Fast-ion transport studies using FIDA spectroscopy at the ASDEX Upgrade tokamak

Dissertation der Fakultät für Physik
der Ludwig-Maximilians-Universität München

vorgelegt von
Benedikt Geiger
Rosenheim
2012

Erstgutachter: Prof. Dr. Hartmut Zohm
Zweitgutachter: Prof. Dr. Harald Lesch
Datum der mündlichen Prüfung: 25.01.2013

Zusammenfassung

Für den Erfolg künftiger Fusionskraftwerke ist ein effektiver Einschluss von supra-thermischen, schnellen Ionen im Magnetfeld-Käfig nötig: Schnelle Ionen sind unter anderem für das Aufheizen des Fusionsplasmas verantwortlich und sind außerdem wichtig für die Erzeugung eines elektrischen Stroms im Plasma. Im Fall eines turbulenten oder magneto-hydrodynamisch (MHD) aktiven Plasmas müssen verschiedene Mechanismen berücksichtigt werden, um die die Verteilung von schnellen Ionen zu bestimmen: Die Verlangsamung und Ablenkung durch Coulomb-Stöße an Elektronen und Ionen, die Wirkung von Potentialschwankungen und mögliche Störungen der Magnetfeld-Konfiguration. Jedoch sind diese Effekte noch nicht vollständig verstanden.

An dem Fusion Experiment ASDEX Upgrade werden schnelle Ionen hauptsächlich durch Neutral -Strahl Injektion (NBI) erzeugt. Um den Einschluss dieser Teilchen zu untersuchen, wurde eine "Fast-Ion D-alpha" (FIDA) Diagnostik im Rahmen dieser Doktorarbeit aufgebaut. Durch Ladungsaustausch-Reaktionen mit neutralen Teichen im Plasma erhalten die schnellen Ionen ein gebundenes Elektron und können Balmer-Alpha-Strahlung emittieren. Diese sog. FIDA-Strahlung kann abhängig von der Geschwindigkeit der Ionen mit Doppler-Verschiebungen von mehreren Nanometern beobachtet werden und ist entlang der NBI lokalisiert, denn nur dort existieren neutrale Teilchen mit signifikanter Dichte. Die FIDA-Diagnostik verwendet horizontale und vertikale Sichtlinien, die auf eine 2.5 MW NBI Quelle fokussiert sind. Dadurch können schnelle Ionen mit unterschiedlichen Geschwindigkeitsvektoren oberhalb einer Energie von 25 keV erfasst werden. Um die gemessene FIDA-Strahlung quantitativ zu analysieren, wurde ein Monte-Carlo Code implementiert, weiterentwickelt und validiert, der es ermöglicht, synthetische Spektren aus einer theoretischen Verteilungsfunktion schneller Ionen zu bestimmen.

Mit Hilfe der FIDA Diagnostik wurde der mögliche Einfluss von Turbulenzen (Potentialschwankungen) auf die schnellen Ionen untersucht. Plasma-Entladungen wurden unter verschiedenen experimentellen Bedingungen durchgeführt, die ein geringes Level an MHD-Aktivität aufweisen, sodass ein möglicherweise erhöhter Transport von schnellen Ionen auf die Turbulenzen zurückzuführen wäre. Jedoch zeigt der Vergleich der gemessenen FIDA-Spektren mit der Simulation eine gute Übereinstimmung wenn angenommen wird, dass der Transport der schnellen Ionen nur durch Coulomb-Stöße bestimmt ist. Simulationen die einen zusätzlichen Transport berücksichtigen, können die Messungen nicht beschreiben.

Im Gegensatz dazu wird in Anwesenheit von MHD-Aktivität eine starke Änderung der Verteilungsfunktion der schnellen Ionen beobachtet. Insbesondere in Anwesenheit der sogenannten Sägezahn-Instabilität wird eine Umverteilung von bis zu 50 % der Teilchen gemessen und eine gute Übereinstimmung mit Simulationen gefunden, die diesen Effekt beschreiben. Zudem wurden die Phasen nach dem Auftreten der Sägezahn-Instabilität untersucht. Hier konnte die zeitliche Entwicklung der Dichte der schnellen Ionen wiederum mit klassischen Abbremszeiten in Verbindung gebracht werden.

Abstract

A good confinement of fast-ions, i.e. ions with energies above the thermal energy, is essential for the success of fusion devices as it determines, amongst others, the plasma performance and the heating and current drive efficiencies. In case of a turbulent or magneto-hydrodynamic (MHD) active background plasma, various mechanisms have to be considered in order to estimate the spatial distribution of the fast-ions: the slowing down and radial diffusion by Coulomb collisions on electrons and ions, the effect of potential fluctuations and the effect of perturbations of the magnetic field structure. These can lead to a broadening of the fast-ion distribution function which is not yet completely understood.

At the fusion experiment ASDEX Upgrade, the fast-ions are generated by heating sources such as neutral beam injection (NBI). Their transport properties can be studied by a fast-ion D-alpha (FIDA) spectroscopy diagnostic which has been built in the framework of this thesis. Through charge exchange reactions with neutrals, fast-ions can receive a bound electron and emit Balmer alpha line radiation. This so-called FIDA radiation can be measured with large Doppler shifts and is localized along the NBI path where a high density of neutrals is present. The FIDA diagnostic uses radially distributed lines of sight that intersect, in the horizontal and in the vertical plane, the path of a 2.5 MW NBI heating source. Thereby different parts of the fast-ion phase space above 25 keV can be analyzed.

To interpret the FIDA radiation quantitatively, a forward modelling code has been implemented, tested and further developed. The code calculates, based on theoretical fast-ion distribution functions, synthetic FIDA spectra that can be compared to the measurement.

In MHD-quiescent plasmas, the possible effect of turbulence on the fast-ion transport has been investigated with the FIDA diagnostic. The measurements obtained under different experimental conditions, such as during on- and off-axis NBI heating, are compared to simulations. Thereby a good agreement is obtained when using simulations that describe the broadening of the fast-ion distribution by collisions only. In contrast, simulations that assume an additional diffusion of fast-ions do not fit the experimental data. This reveals that a possible anomalous fast-ion transport, caused by potential fluctuations from turbulence, is small and below the sensitivity of the diagnostic.

However, in the presence of MHD-instabilities, a strong radial fast-ion redistribution is observed with the FIDA diagnostic. In particular, in the presence of magnetic reconnection events induced by sawtooth crashes, a radial redistribution of up to 50% of the central fast-ion population is evidenced that is in agreement with theoretical predictions. The evolution of the redistributed fast-ion population after the sawtooth crash enables to investigate the fast-ion transport properties in the absence of strong MHD activity. Here also, a good agreement is found with the fast-ion diffusion that is caused by collisions only.

Contents

Chapter 1

Introduction

1.1 Thermonuclear fusion

The present day prosperity of the western world is based on the ready availability of fossil fuels. However, within the near future, first the costs of oil and gas and later the costs of coal will increase more and more. On the one hand, the extraction of fossil fuels will become more and more demanding as the easy accessible fields will be depleted. On the other hand, the energy demand is rapidly increasing due to the growth of the developing countries like China or India. In addition, the world's climate is influenced by the exhaust of burning fossil fuels. This results in the need of new energy supplies to sustain the wealth of our civilization.

A possible contribution to the worlds future energy supply can be fusion power plants. The fusion process is a well known source of energy. For example the sun produces most of its energy from the thermonuclear fusion of hydrogen to helium. The sun burns about 564 million tons of hydrogen per second to 560 million tons of helium. The resulting mass difference of 4 million tons is transformed into energy, according to Einstein's formula $E = mc^2$. The main reaction that takes place in the sun's core is the proton-proton chain. It is depicted on the left side of figure 1.1. Hydrogen nuclei (protons) are fused to deuterium nuclei ($^2_1$H), then to $^3_2$He and finally to $^4_2$He.

It has already been found in the early 20th century that the sun produces its energy by fusion reactions. At that time, the idea was born to build a power plant on earth that uses the same, nearly unlimited source of energy. However, if was found that the first reaction of the proton-proton chain cannot be realized in a fusion device on earth as in particular the very high densities of the sun's core cannot be reached. Therefore, a different fusion reaction will be used in the first generation of fusion power plants due to its higher reaction rate:

$$^2_1H + \ ^3_1H \rightarrow \ ^4_2He + \ n \ + \ 17.6 \ MeV \tag{1.1}$$

where a deuterium ion, $^2_1$H, and a tritium ion, $^3_1$H, fuse to a helium ion (also called alpha particle) and a neutron n releasing an energy of 17.6 MeV. The reaction has a significantly higher cross-section than the first reaction of the proton-proton chain as no weak forces are involved, i.e. no protons are transformed into neutrons. It is feasible in a fusion power plant since both isotopes are available on earth or be can easily produced. Deuterium is a stable isotope of hydrogen and can be extracted from the oceans as water consists of 0.0115% of deuterium. Tritium is not naturally available on earth (it has a half life time of 12.3 years) but can be bred from lithium. By exposing a lithium blanket to neutrons which result from the fusion reaction, tritium can be obtained. As can be seen in figure 1.1, the fusion

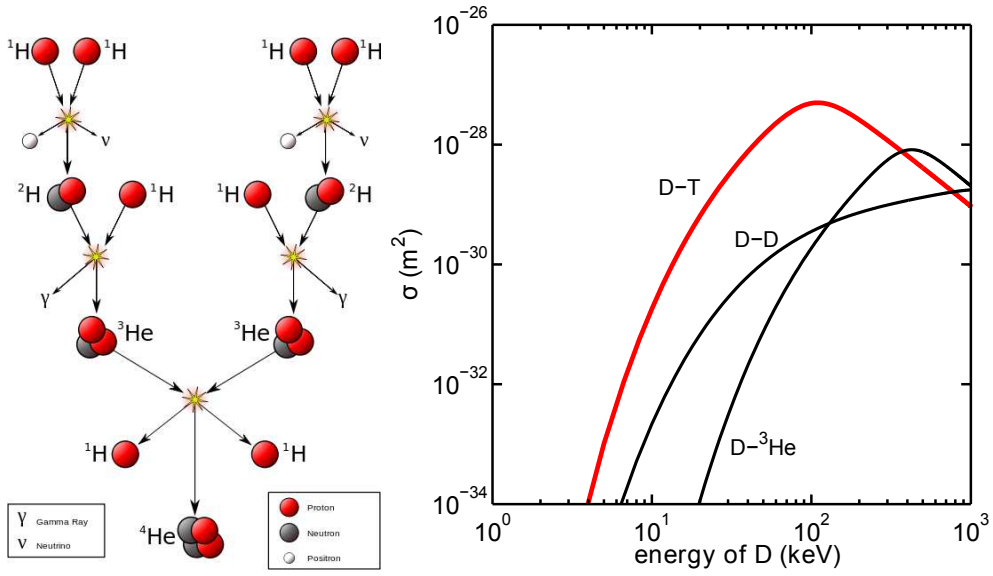

Figure 1.1: Left: Proton-proton chain as the main mechanism the sun uses to fuse hydrogen ions to helium [1]. Right: Cross-sections for the fusion reactions between deuterium, D, and tritium, T, between deuterium and helium and between two deuterium ions as a function of the collision energy.

reaction needs high collision energies between the reactants before it can happen because the Coulomb barrier between two equally charged particles has to be overcome. Therefore, plasma temperatures above 10 keV[1] are needed in a fusion device because this guaranties high particle velocities and hence high collision energies. Furthermore, many collisions between the reactants must be ensured since the cross-section of the fusion process is small compared to that of the coulomb repulsion. Hence, the plasma density in a fusion device and the energy confinement time must be relatively high. A threshold for the onset of self-sustained fusion can consequently be described by the Lawson criterion. It states that the fusion product, i.e. the product of the temperature, the energy confinement time and the plasma density has to be higher than 5×10^{21}keV s/m^3.

Two main concepts exist to approach the Lawson criterion: One is to generate high densities at low energy confinement times by using very intense laser beams that compress and heat up a pellet of deuterium and tritium on very short time scales. The other approach uses low densities but higher confinement times. It is realized in magnetic confined fusion and makes use of the properties of ionized gases, i.e. plasmas. Plasmas, as defined by Langmuir in 1928 [2], can be seen as a fourth state after the gaseous state and consist of charged particles that show a collective behavior such as oscillations. In magnetic fields, the charged particles are subject to the Lorentz force. Whereas the motion parallel to the magnetic field lines is unrestricted, the perpendicular motion is forced onto gyration orbits. This enables to confine plasmas without direct contact to surrounding walls which is essential for a fusion power plant because every material would melt at the necessary temperatures of several keV.

As linear magnetic field configurations, such as mirror machines, show strong losses at the ends, most fusion experiments use a configuration in which the magnetic field lines are bent to a torus. For the stability in toroidal geometries, it is necessary to have helically twisted field lines. The magnetic field in toroidal devices can consequently be described by a toroidal and a poloidal component. The toroidal magnetic field is typically produced by coils that are arranged around the torus as indicated in blue color in figure 1.2. To generate the poloidal magnetic field, two different concepts exist. On the one hand, the magnetic field lines can be twisted by additional magnetic field coils or by curved main field coils as done

[1] 1 eV is equal to 11605 Kelvin.

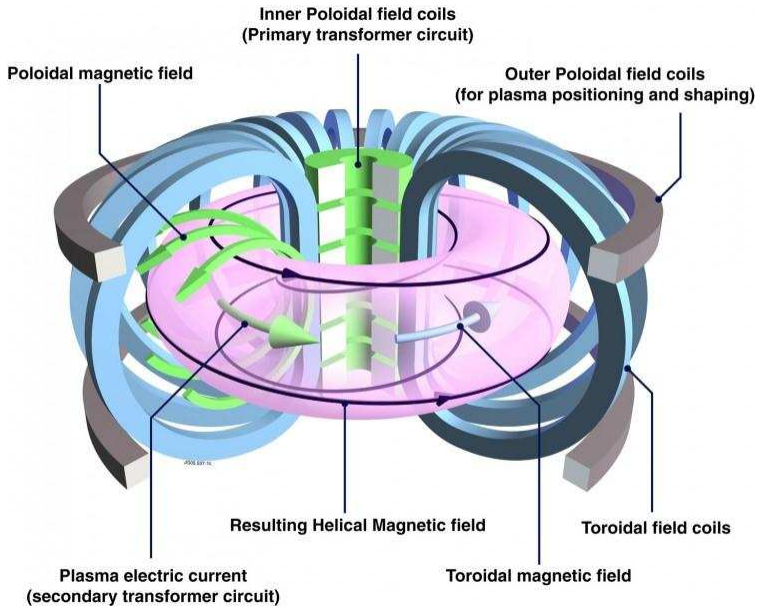

Figure 1.2: Configuration of a tokamak: The toroidal magnetic field is generated by the coils indicated in blue. The poloidal magnetic field is generated by a plasma current that is induced by the inner transformer coil shown in green [6].

in so called stellarators [3]. On the other hand, a poloidal magnetic field can be generated by an internal plasma current following the tokamak concept.

1.2 The tokamak concept

In tokamaks, the toroidal field is generated by external coils while the poloidal field originates from a strong toroidal current that flows in the highly conductive plasma. The current is mainly driven by a loop voltage that is induced by a central coil (inner poloidal field coil) according to the transformer principle using the plasma as secondary coil (see figure 1.2). Tokamaks have been developed in Russia in the late 1950s [4] and are nowadays the fusion experiments with the best performance in terms of the fusion product. Therefore, also the next generation fusion device, ITER [5], which is currently under construction in France and which should closely approach the Lawson criterion, will be a tokamak. The poloidal field B_θ in a tokamak is usually about a factor of 10 smaller than the toroidal magnetic field B_ϕ. It twists the magnetic field lines and thereby produces nested flux surfaces on which the pressure is constant. The helical twisting of the field lines can be described by the safety factor q:

$$q = \frac{d\Theta}{d\Psi} = \frac{m}{n} \tag{1.2}$$

where n are the poloidal and m toroidal turns of a given field line, to close with itself. Ψ is the poloidal flux and Θ is the toroidal flux defined by:

$$\Theta, \Psi = \int \vec{B} d\vec{A} \tag{1.3}$$

Here, $\vec{B}$ is the magnetic field vector and $\vec{A}$ defines an area that is, for the toroidal flux, located in the poloidal plane and for the poloidal flux, e.g. located in the midplane[2]. Typically, q is close to one in the plasma center and increases towards the plasma edge. As an example,

[2]The midplane is located at the vertical position of the magnetic axis.

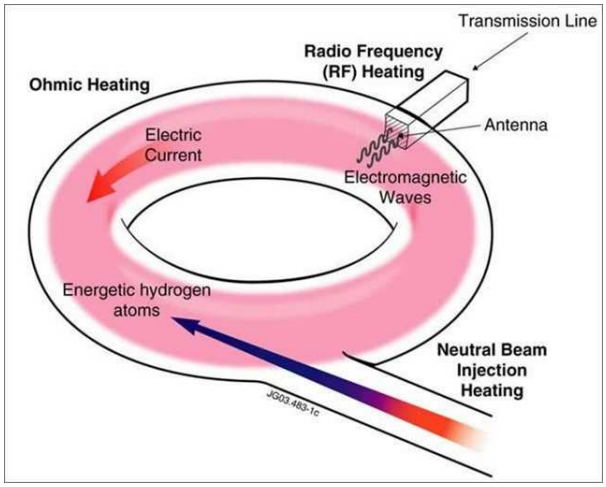

Figure 1.3: External heating mechanisms used in fusion experiments to increase the plasma temperature and to generate a toroidal plasma current. The illustrated heating mechanisms consist of wave heating, ohmic heating and neutral beam injection [8].

figure 1.2 shows a magnetic field line in black that experiences m=4 toroidal turns while performing n=1 poloidal turns. The flux surface which consists of field lines that have this property is consequently a q=4 surface.

The first Russian tokamak T-3A [4] could show (for that time) spectacularly high electron temperatures of up to 1 keV as the current induced to the plasma not only twists the magnetic field lines but also contributes to the plasma heating. However, with increasing temperatures, the ohmic heating becomes more and more ineffective as the electric resistance in plasmas is proportional to $T^{-3/2}$ [7]. To reach significantly higher temperatures above 1 keV, additional heating mechanisms are needed. Most fusion experiments use additional heating by electromagnetic waves and by the injection of energetic neutrals (Neutral Beam Injection, NBI), as illustrated in in figure 1.3. The energetic neutrals injected by NBI penetrate into the plasmas in straight lines until they are ionized by charge exchange and ionization processes. Consequently, they are confined by the magnetic field and release their energy along their paths by Coulomb collisions with plasma ions and electrons.

In future fusion devices the external heating sources are foreseen to be necessary only in the starting phase of plasmas or for plasma control. As soon as the Lawson criterion is reached and a significant amount of fusion processes sets in, the plasmas are expected to maintain or even increase their temperatures by a part of the energy released by the fusion process itself: The produced helium ions have an energy of 3.5 MeV and heat the plasmas similar to the injected beam neutrals by collisions with electrons and plasma ions.

These helium ions, as well as the ionized beam neutrals and the ions accelerated by electromagnetic waves, i.e. by ion cyclotron resonance heating (ICRH), have energies above the thermal energy and are therefore called fast-ions. They must be well confined in future fusion devices because poorly confined fast-ions cannot contribute to plasma heating and can even damage the first wall. Effects that redistribute fast-ions such as intrinsic asymmetries of the magnetic field structure, turbulent fluctuations or magneto-hydrodynamic (MHD) modes such as sawtooth crashes or Alfvén Eigenmodes [9] must consequently be understood and if possible be prevented in future fusion devices. Moreover, the good fast-ion confinement is important since fast-ions with a non-uniform velocity distribution into the toroidal direction can contribute to the plasma current. They can be used to tailor the plasma current profile, needed e.g. for better confinement properties, or to replace the inner transformer coil of a tokamak [10]. The latter is of particular interest because the need of an inner transformer

coil limits the tokamak concept to a pulsed operation. The loop voltage that drives the plasma current corresponds to a monotonic change of a current in this coil. As the current cannot be increased infinitely long, tokamaks need effective means of non-inductive current drive to be operated in steady state.

When studying the fast-ion confinement, the six dimensional fast-ions phase space needs to be observed which consists of three spatial coordinates and three coordinates in the velocity space. By accounting for the toroidal symmetry of a tokamak and for the symmetric gyro motion of charged particles around the magnetic field lines, the phase space can be reduced to 4 dimensions: the radial and the vertical coordinate, the fast-ion energy and the fast-ion pitch, i.e. the cosine of the angle between the fast-ion velocity vector and the magnetic field vector.

Several techniques exist to study the fast-ion phase space such as fast-ion loss detectors (FILD) [11], neutral particle analyzers (NPA) [12], gamma ray tomography [13], collective Thomson scattering (CTS) [14], neutron spectroscopy [15] and fast-ion D-alpha (FIDA) [16] measurements. Each technique observes a given, often complementary, part of the fast-ion phase space. The FIDA technique, which has been applied for this thesis, enables to study confined fast-ions at different radial positions and in different parts of the fast-ion velocity space. It analyzes strongly Doppler shifted radiation of neutralized fast-ions and has become a widely used method due to its good spatial and temporal resolution. It is nowadays used at several fusion devices such as MAST, TEXTOR [17], LHD [18], NSTX [19] and ASDEX Upgrade [20].

1.3 This thesis

The interaction of fast-ions with the thermalized plasma is an active field of investigations in plasma physics. In particular the fast-ion transport and redistribution in the presence of turbulence and MHD activity is not yet completely understood and might limit the performance of future fusion devices. To address this problem at the ASDEX Upgrade tokamak, a new FIDA diagnostic has been installed in the framework of this thesis that now allows the investigation of the fast-ion transport with a high temporal and spatial resolution and with a good signal to noise ratio. The diagnostic has particularly been designed to answer the questions whether turbulent fluctuations significantly reduce the fast-ion confinement and how the effect of sawtooth crashes on the fast-ion distribution function can be characterized.

In chapter 2 of this thesis, an introduction to the generation of fast-ions by neutral beam injection (NBI) is given and the classical fast-ion orbits are presented. The classical slowing down distribution of fast-ions and the mechanism of the fast-ion current drive are described. The anomalous fast-ion transport is explained and an introduction to the FIDA technique and to TRANSP, a code that predicts 4D fast-ion distribution functions, is given. In chapter 3, the experiment ASDEX Upgrade is described with detailed information on the heating systems and its diagnostics used to characterize the plasmas. In the chapter 4, a forward modelling tool called F90FIDASIM is presented that is needed to analyze measured FIDA data. The Monte Carlo code has been implemented at ASDEX Upgrade as a part of this Ph.D. thesis and has been further developed and tested. A general description, as well as a validation and a sensitivity study, is presented. Chapter 5 is devoted to the properties of the FIDA diagnostic. After discussing the geometric setup, the calibration techniques and the different contributions in the spectra, the observed fast-ion velocity space is illustrated. In the two subsequent chapters, the experimental results are described. In chapter 6, the comparisons between the FIDA measurements, performed in MHD-quiescent plasmas, and

results from forward modelling are given. The simulated fast-ion distribution functions are compared to the measurement when using different NBI injection energies and geometries and the possible fast-ion redistribution, caused by turbulence is investigated. Chapter 7 analyzes and discusses measurements of the fast-ion density in the presence the sawtooth instabilities. Continuous observations of different parts of the fast-ion velocity space are presented and comparisons to theoretical predictions are discussed. Finally, a summary and conclusion is given in chapter 8.

Chapter 2

Theoretical background

This chapter presents the theoretical background of this Ph.D. thesis. First, the generation of fast-ions and their classical orbits are described. Then, the neoclassical slowing down distribution, as well as the mechanisms of fast-ion current drive, is discussed. The non-classical redistribution of fast-ions is discussed in section 2.5, followed by an introduction to the FIDA technique. Finally the TRANSP code is presented which is used in this work to predict theoretical fast-ion slowing down distribution functions.

2.1 Generation of fast-ions

Fast-ions are present in fusion plasmas by the fusion process itself as well as due to the application of ion cyclotron resonance heating (ICRH) and Neutral beam injection (NBI). The fast-ions generated by these processes populate different parts of the velocity space. The fast helium ions from the fusion process have an isotropic distribution of velocity vectors at 3.5 MeV. In contrast, the velocity vectors of fast-ions generated by ICRF and NBI only point into certain directions. ICRH generates fast-ions with large velocities perpendicular to the magnetic field by accelerating confined ions up to several hundreds of keV with electromagnetic waves at the Larmor frequency. The velocity vectors of fast-ions injected by NBI systems depend on the NBI injection geometry and acceleration voltage. Their generation will be explained in more detail because the confinement of NBI generated fast-ions has been studied during this Ph.D. work.

2.1.1 Neutral beam injection

Neutral beam injection is one of the main heating and current drive sources that are foreseen for future fusion experiments such as ITER. As an example, ITER will have about 33 MW of NBI heating power which will be almost half of its total external heating power (74 MW). The general setup of NBI heating systems is depicted in figure 2.1. Ions are generated in the ion source, are accelerated within a high voltage grid and are then neutralized in a cloud of gas. Finally the resulting neutrals are injected into the plasma. Two different approaches are used in NBI heating systems, namely sources with negative ions, e.g. D^-, and sources with positive ions such as D^+. While the positive ion sources are limited to injection energies below about 100 keV[1], the negative sources can be operated with higher

[1] Above this value, the neutralization efficiency of the accelerated positive ions strongly decreases.

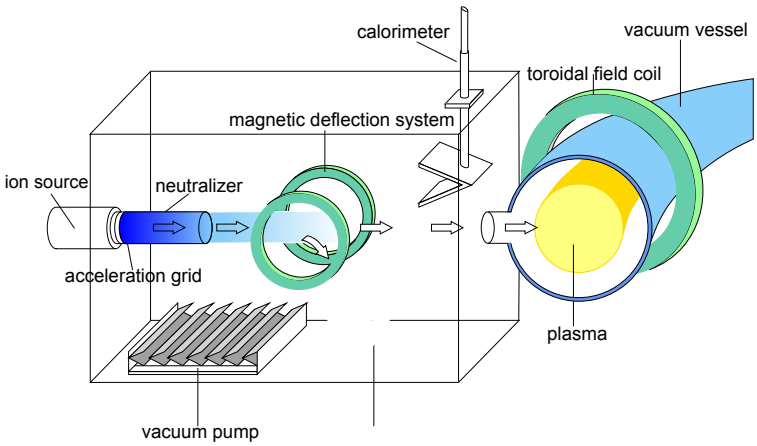

Figure 2.1: Scheme of neutral beam injection. The ions created in the so called ion source are first accelerated in the acceleration grid and then neutralized. Then, they injected into the plasma.

injection energies. This will be necessary in large size machines like ITER because the high injection energies permit the neutral beams to penetrate deep into the plasmas. However, most nowadays fusion experiments, such as ASDEX Upgrade, use positive ion sources as negative ion sources are more difficult to build and to maintain. The neutrals injected by the positive ion-sources have three different energy components since D_2^+ and D_3^+ molecules are generated in addition to the D^+ ions. These molecules are also accelerated, neutralized and injected into the plasma. The energy of the single atoms is then half and one third of the full injection energy. The fraction of full, half and third energetic neutrals is called species-mix. It can be defined as a function of particles (current) or as a function of the energy. The geometry of the beam of NBI can be described by the ion source's dimension, its horizontal and vertical focus and by its divergence. The focus of NBI is achieved by using multiple beam-lets that have slightly different injection geometries. The divergence, which is about one degree at AUG, results from the interaction of the ions among each other in the acceleration grid. The divergence scales inversely with the the ion-velocity because ions with large velocities have less time to interact with the space charges present in the acceleration grid.

The injected neutral particles can penetrate through the magnetic field of a tokamak in straight lines until they are ionized by collisions with plasma ions and electrons. Then, the ionized neutrals are caught by the magnetic field and circulate in the plasma on different orbits which depend on the deposition position, the fast-ion energy, the geometry of NBI and the magnetic field structure.

2.2 Fast-ion orbits

Charged particles such as fast-ions are subject to the Lorentz force when moving in magnetic fields. Depending on their velocity vector perpendicular to the magnetic field lines, $v_\perp$, they gyrate with a certain Larmor radius ρ_L:

$$\rho_L = \frac{v_\perp}{\omega_c} \tag{2.1}$$

where, ω_c is the cyclotron frequency, defined by:

$$\omega_c = \frac{qB}{m} \tag{2.2}$$

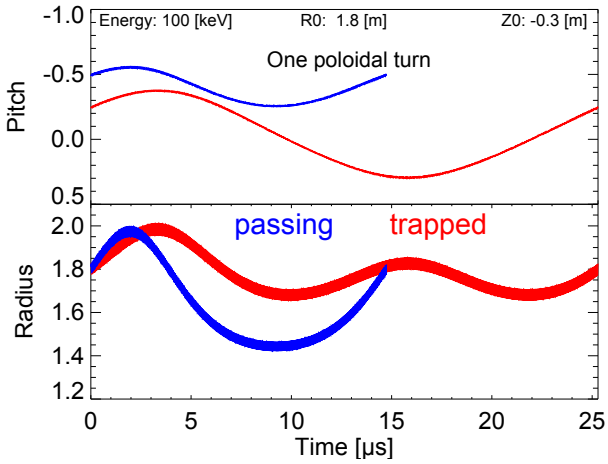

Figure 2.2: Evolution of the pitch angle of a passing (blue) and a trapped particle (red) that perform one poloidal turn.

with m the particles mass, q its charge and B the magnetic field strength. In contrast to electrons and thermal ions, the fast-ions typically have large gyro radii in the range of centimeters. As an example, a deuterium ion with a perpendicular velocity of 3.1×10^6 m/s (100 keV) has a cyclotron frequency of $f_c = \omega_c/2\pi \approx 20$ MHz and a Larmor radius of $\rho_L \approx 2.5$ cm in a magnetic field with 2.5 T. The magnetic moment that corresponds to the gyro-motion of charged particles is defined by:

$$\mu = \frac{m\ v_\perp^2}{2B} \tag{2.3}$$

It is a conserved quantity for a given particle and is therefore also called the first adiabatic invariant. As consequence of the conservation of the magnetic moment, the perpendicular velocity, $v_\perp$, of a particle changes if the particle circulates in a varying magnetic field. The change of $v_\perp$ is balanced by the parallel velocity, $v_{||}$ because the particles energy must be conserved. Instead of the parallel and perpendicular velocity, the velocity space of fast-ions is often described by the particles energy and the so called pitch. The latter, also called pitch angle, is defined by:

$$pitch = \frac{v_{||}}{v_{tot}} = \cos(\alpha) \tag{2.4}$$

where v_{tot} is the total velocity and α is the angle of the fast-ion velocity vector to the B-field. For particles that move parallel or anti parallel to the field lines, the pitch is 1 or -1. Particle that only gyrate around the field lines have a pitch of zero.

In tokamaks, the toroidal magnetic field strength decreases radially with $1/R$ because of the toroidal arrangement of the magnetic field coils. Particles that propagate along the helically twisted magnetic field lines consequently change their pitch as they continuously change their radial position. As an example, figure 2.2 shows the temporal evolution of the pitch and the radius of two simulated fast deuterium ions with 100 keV that make one turn in the poloidal plane. The simulation has been performed with the full orbit code GOURDON [21]. As can be seen, the pitches, as well as the radial positions of the two particles, constantly change in time.

Fast particles with small pitches are particularly affected by the conservation of the magnetic moment because they can be reflected in an increasing magnetic field. Figure 2.3 shows the orbits of the two 100 keV particles simulated by GOURDON. The ions start at the same position, indicated with black diamonds, have the same energy but different pitches (-0.5 and -0.25). While the trajectory shown in blue color follows a closed, poloidal orbit in

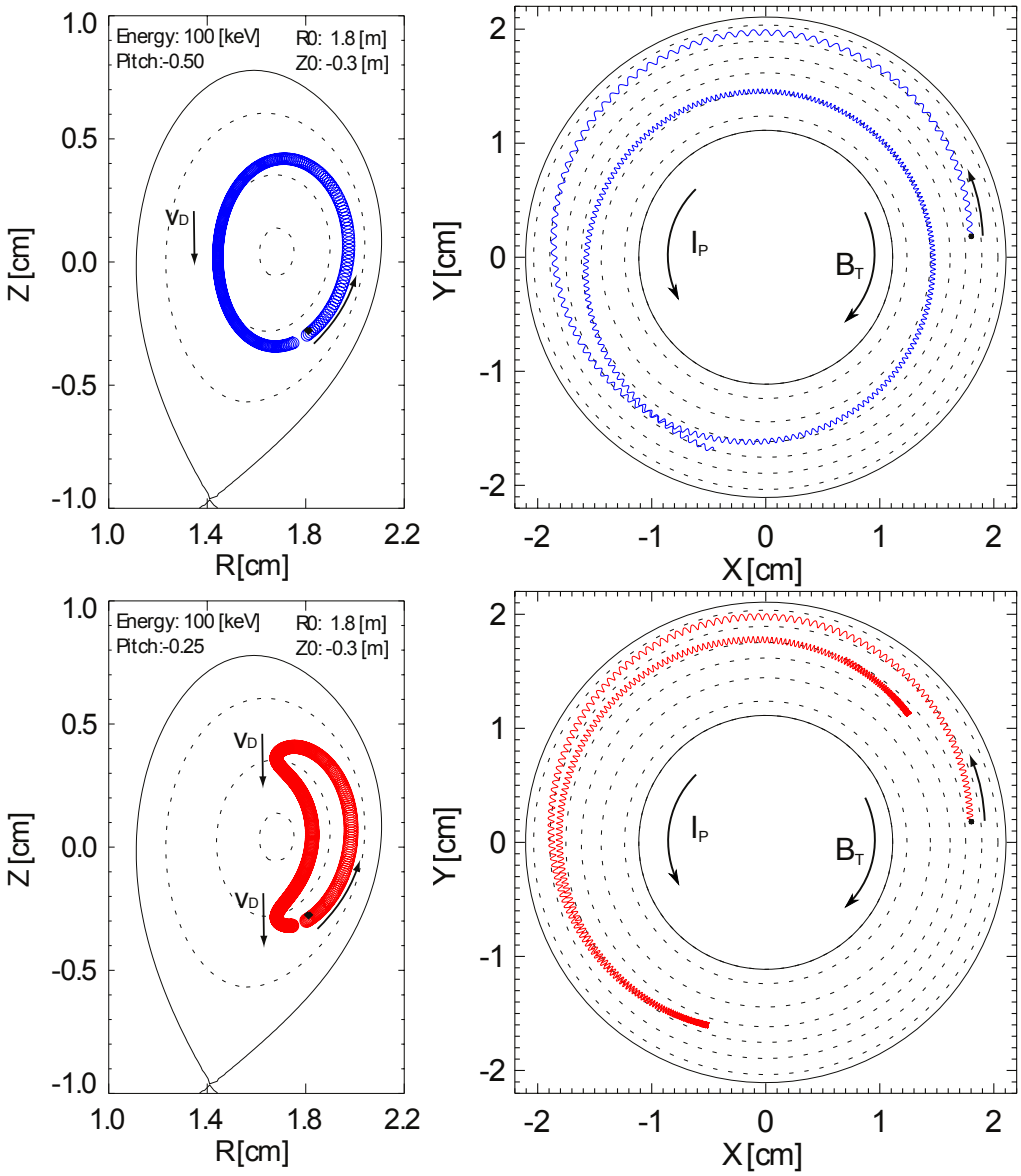

Figure 2.3: Top down view and poloidal view on two fast-ion orbits. Both fast-ions are started at R=1.8 m, Z=-0.30 m with an energy of 100 keV. The difference between the two ions is the pitch which is -0.5 for the upper figures and -0.25 for the lower ones. The orbit of the fast-ion with pitch -0.5 is passing, the one with pitch -0.25 is trapped.

the radial plot, the one shown in red performs a so called banana orbit. This ion is reflected as soon as all its parallel energy is converted into the perpendicular motion. It is trapped at large radii, i.e. at the so called low-field side[2]. It should be noted that trapped particles change the sign of their pitch when being reflected. As can be seen in the top down view of figure 2.3, the trapped particle is started with a velocity vector in counter-clockwise direction and then moves, after the first reflection, into the clockwise direction.

For the particle orbits shown in figure 2.3, the toroidal magnetic field, B_T, is directed clockwise and the current, I_P, is defined counter-clockwise. Following a field line in the toroidal direction counter-clockwise, it consequently performs a counter-clockwise rotation in the poloidal plane. For this reason, the two particles shown in figure 2.3 first move upwards from their starting positions because their gyro centers move mostly parallel to the magnetic field lines.

[2]The low-field side is defined by the radii that are larger than the radius of the magnetic axis of the plasma.

The expression 'mostly' is needed because the orbits of the fast-ions deviate from the flux surfaces (indicated by dashed lines in figure 2.3). The particles are on so called drift-surfaces that differ from the flux surfaces due to the centrifugal force and the $\nabla\vec{B}$ force. The latter is the force on a moving charged particle in an inhomogeneous magnetic field.

In general, forces, $\vec{F}$, that are directed perpendicular to the magnetic field, $\vec{B}$, cause a drift velocity, $\vec{v_D}$, perpendicular to $\vec{F}$ and $\vec{B}$:

$$\vec{v_D} = \frac{\vec{F} \times \vec{B}}{qB^2} \tag{2.5}$$

The direction of the drift velocity can be explained as gyrating particles are accelerated and de-accelerated into the forces direction. They are thereby not displaced on average. However, by the acceleration and de-acceleration, the gyro orbits are deformed. This results in a net displacement perpendicular to the magnetic field lines and perpendicular to $\vec{F}$.

The centrifugal force and the $\nabla\vec{B}$ force point into the same direction. Hence, the associated drift velocities, namely the curvature and $\nabla\vec{B}$-drift, can be expressed by one equation:

$$\vec{v_D} = \frac{m}{q\ B^3}(v_{||}^2 + 0.5\ v_{\perp}^2)\vec{B} \times \nabla\vec{B} \tag{2.6}$$

As can be seen, the drift velocity of a fast-ion depends on both, $v_{||}$ and $v_{\perp}$. For the trajectories shown in figure 2.3, the drift velocity is directed downwards because the centrifugal force and the $\nabla\vec{B}$ force point outwards and as B_T has been defined clockwise.

The amount of the displacement, dz, at a given position depends on the time during which a particle is present at this location ($dz = v_D dt$). Thus, the displacement of the fast-ion orbits is largest at low radii. There, the particle's parallel velocities, i.e. the pitches are smallest and dt is consequently largest. In particular, at the bounce positions of trapped particles, a large displacement can be observed as the parallel velocity of the particles becomes zero. At the upper bounce position of the trapped orbit shown in figure 2.3, the particle is displaced downwards to a flux surface closer to the plasma center. At the lower bounce position, the drift velocity moves the particle also downwards, but in this case away from the plasma center. Thereby, the particle is back on its initial flux surfaces after one poloidal turn. This explains that particles are confined in axisymmetric toroidal devices when twisting the magnetic field lines because the drift effects are balanced.

The orbits of the particles strongly depend on their initial position. To illustrate this dependence, fast-ions with an energy of 100keV and with an initial pitch of -0.25 have been simulated at various starting positions. The types of the resulting orbits are shown in the left plot of figure 2.4. Orbits that are not confined by the magnetic field structure are indicated with gray crosses. The trapped orbits are indicated with red diamonds, the passing orbits are shown with blue stars and so called stagnation orbits are displayed by yellow triangles. The right plot of figure 2.4 shows the orbits of a trapped (red), a passing (blue), an un-confined (gray) and of a stagnating particle (yellow). The stagnation orbit is similar to a passing orbit but does not reach the high field side.

In the left plot of figure 2.4, the region of the confined orbits is shifted relatively to the flux surfaces shown with dashed lines. That is to say, there are on the one hand confined orbits that are started on the low-field side, outside the last closed flux surface (separatrix). On the other hand, there are unconfined orbits at the high field side that are started inside the separatrix. This can be explained by the drift surfaces, i.e. the drift velocity in combination with the particles movement along the magnetic field lines. Particles started with negative pitches at the low-field side first propagate upwards along the magnetic field lines. As v_D

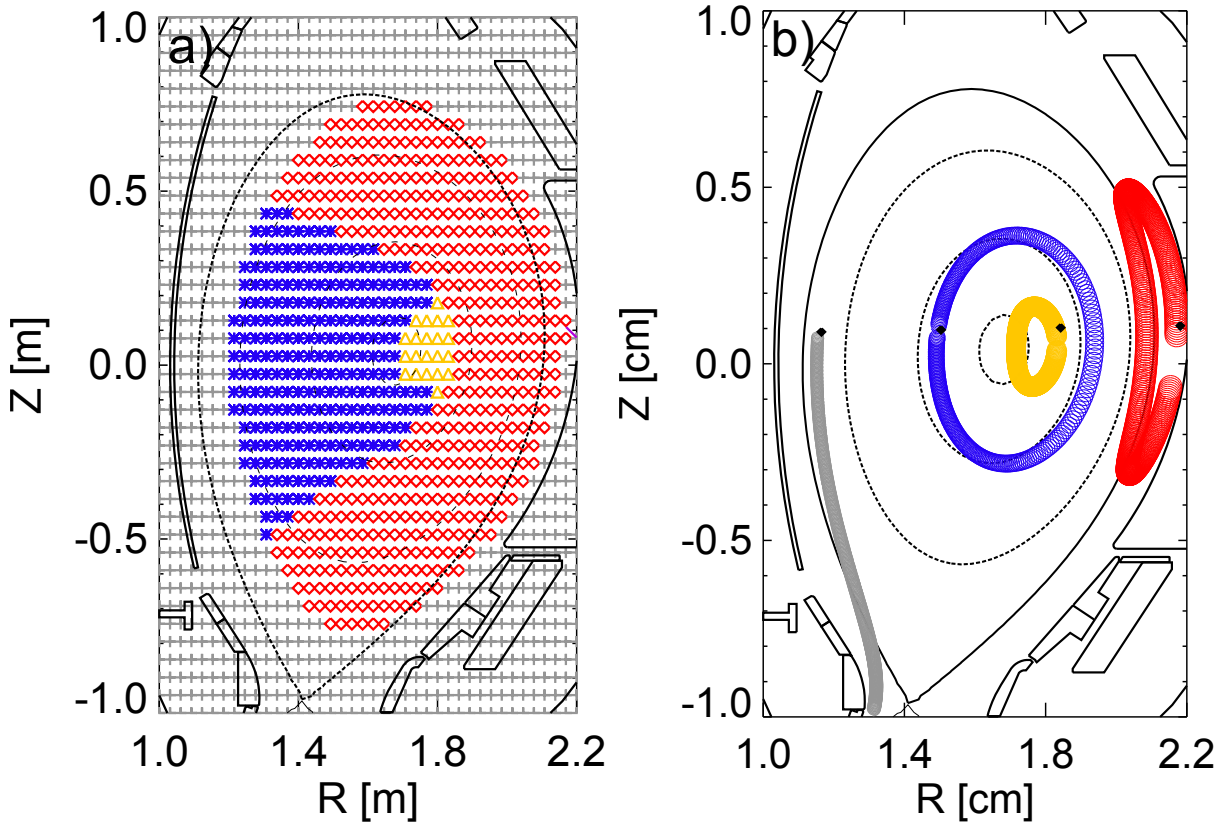

Figure 2.4: a) Types of orbits of 100 keV fast-ions with an initial pitch of -0.25 that are started at different radial and vertical positions. In blue, start positions of fast-ions that result in passing orbits are shown. In red, the start positions of trapped orbits and in gray the ones of unconfined orbits are indicated. The positions shown in yellow correspond to stagnation orbits. b) Radial plot of an unconfined (gray), a stagnation (yellow), a trapped (red) and a passing orbit (blue) that correspond to 100 keV fast-ions with a pitch of -0.25.

points downwards, particles started outside the last closed flux surface can drift back into the confined region (see red orbit in figure 2.4). In contrast, the particles started at the high-field side first propagate downwards. As the drift velocity is in addition directed downwards, particles started inside the confined region can be displaced to a non-closed field line (see gray orbit in figure 2.4).

In this context, it should be noted that, depending on the configuration of the plasma current and the toroidal field, only certain NBI injection geometries are useful. When e.g. injecting neutrals with negative pitches into the configuration described above, most of the fast-ions which are typically deposited at the low-field side, are on confined orbits. In contrast, when injecting fast-ions with positive pitches, a significant amount of injected particles is on unconfined orbits. They first propagate downwards and are displaced by v_D to a non-closed field line. Thereby, NBI would be less efficient because prompt losses cannot contribute to heating and current drive.

2.3 The neoclassical fast-ion slowing down distribution

The neoclassical fast-ion slowing down distribution represents the distribution of fast-ions that are created at a certain energy and pitch, that are propagating through the plasma and that are decelerated and redistributed by collisions with electrons and ions. High energetic fast-ions mainly interact with electrons because the momentum, dp, transferred within a

coulomb collision, depends on the time two particles can interact with each other:

$$dp = \vec{F}dt \tag{2.7}$$

where $\vec{F}$ is the coulomb force. The time dt is small for collisions between thermal plasma ions and high energetic fast-ions as it depends on the relative collision velocity. The electrons have on average significantly higher velocities than fast-ions. As an example, the mean velocity of electrons at a temperature of 2 keV is significantly larger than the velocity of 100 keV fast-ions. However, within the thermal velocity distribution of electrons, there are also slow electrons with velocities comparable to the fast-ions that can be efficiently dragged. The drag force imposed by the electrons decelerates the fast-ions while it does not change the fast-ion pitch. The reduced mass for the interaction between electrons and ions is small. With decreasing fast-ion energies, the relative collision velocities between fast and thermal ions become smaller while those with the electrons become larger. Consequently, the fast-ions interact more and more with the plasma ions. The fast-ion energy, at which one half of the energy is transferred to the electrons and the other half to the ions, is called the critical energy, E_c. It can be approximated for pure Deuterium plasmas by [22]:

$$E_c = 18.6 \cdot T_e \tag{2.8}$$

The critical energy is proportional to electron temperature, T_e, as it depends on the relative collision velocity between fast-ions and electrons. At higher temperatures, the electrons are faster, have higher relative collision velocities with the fast ions and consequently drag the fast-ions less efficiently. Hence, the critical energy increases with T_e as collision with thermal ions become more likely. Below the critical energy, the velocity distribution of fast-ions changes due to pitch angle scattering as the reduced mass for collisions between fast-ions and plasma ions is relatively large.

The fast-ion density present in a plasma depends, besides on the strength of the fast-ion source, on the slowing down time, τ, of fast-ions which is a function of the collisionality [23]. The collisionality of a given plasma scales linearly with the density, while it is inversely proportional to the square of the plasma temperature. High collisionalities consequently result in a large attenuation of fast-ions, short slowing down times and a fast-ion density that is smaller compared to that in a low-collisionality plasma.

As an example, figure 2.5 shows a theoretical slowing down distribution that is representative for ASDEX Upgrade. The distribution function corresponds to fast ions that are injected into a plasma by a synthetic off-axis, tangential NBI source that injects neutrals with 100keV. The left plot shows a poloidal view that contains the density of fast-ions. In addition, the NBI deposition profile of the tangential source is shown in transparent red. As the deposition profile is off-axis, the corresponding fast-ion slowing down distribution is localized off-axis as well. The radial fast-ion distribution is maximal at low radii where the fast-ions propagate slower along the magnetic field lines (see figure 2.2) because the fast-ion density corresponds to the time-integral of the fast-ion flux.

The right plot of figure 2.5 shows, for the position indicated on the left plot by an arrow, the predicted fast-ion velocity space in terms of the fast-ion energy and the pitch. The highest energies are present at a pitch of ~ -0.8 which corresponds to the tangential neutral beam injection with 100 keV. Between the injection energy and about 40 keV, the distribution does not significantly change in the pitch because, as already mentioned, the high energetic fast-ions mainly interact with electrons. The electron temperature in the simulation is 2 keV at the specified position which defines a critical energy of $E_c = 37.2$ keV. As can be seen, below 40 keV, the pitch angle scattering becomes visible as the velocity space distribution

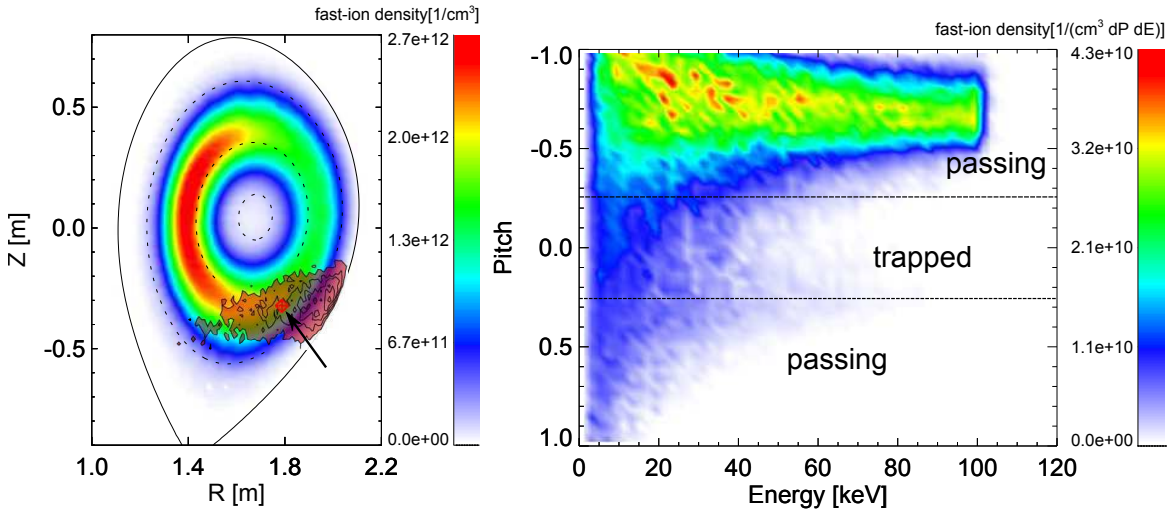

Figure 2.5: Artificial fast-ion distribution function from TRANSP. Left: Poloidal view showing the sum of all possible pitches and energies. Right: Velocity space distribution at the position indicated by a black arrow on the left.

function is broadened. At even lower energies, namely below ~ 10 keV, the fast-ion densities decrease as the fast-ions get thermalized and are then not considered as fast-ions any more. The two dashed lines in the right plot of figure 2.5 indicate the pitches in between which a fast-ion would be trapped. Fast-ions that are between the two dashed lines are consequently bouncing back and forth in the toroidal direction. The bouncing of the trapped ions explains the existence of particles that have positive pitches of $\sim +0.3$ and relatively high energies (60 keV). By collisions, some of the injected ions get on trapped orbits and then propagate into the direction opposite to NBI injection geometry.

2.4 NBI current drive

Fast-ions injected tangentially to the magnetic field lines can contribute to the plasma current. The positive toroidal current of fast-ions, J_{NBI}, injected by a given NBI source can be expressed by:

$$J_{NBI} = I_0 Z_{NBI} F \tag{2.9}$$

where I_0 is the ion current of the NBI source, Z_{NBI} the charge number of the beam ions and F is a function that accounts for the net velocity of fast-ions into the toroidal direction by considering the fast-ion slowing down distribution. The net current generated by NBI is significantly smaller than J_{NBI} because dragged electrons shield the positive ion current. Two main effects prevent the electrons from shielding the positive ion current completely: On the one hand, electrons can be deflected by impurity ions which have higher collision cross-sections ($\propto Z_i^2$) relative to their charge, Z_i, and therefore cannot follow the fast-ions. On the other hand, trapped electrons cannot follow passing ions and therefore cannot completely cancel out the current driven by NBI. By taking these two considerations into account, the current drive by NBI can be approximated according to [24]:

$$J = J_{NBI} \cdot (1 - \frac{Z_{NBI}}{Z_{\text{eff}}}[1 - 1.46\sqrt{\epsilon}A]) \tag{2.10}$$

where Z_{eff} is the effective charge of a plasma defined by:

$$Z_{eff} = \frac{\sum_i n_i \, Z_i^2}{n_e} \tag{2.11}$$

where i denotes the different ion species present in a plasma with the density n_i and charge Z_i. n_e is the electron density. The function A in equation 2.10 is a function that typically ranges from 1.18 to 1.67 [7] and that mainly depends on Z_{eff}. ϵ is the inverse aspect ratio, defined by:

$$\epsilon = a/R_0 \tag{2.12}$$

where a is the minor radius, i.e. the radius of a given plasma in the poloidal plane and R_0 the radius of the plasma center. The radial variation of the magnetic field strength in a toroidal device depends on ϵ. Thus, the larger ϵ, the larger is the radial variation of B_T, the more electrons are trapped and the more current is driven by NBI. Furthermore, it can be deduced from equation 2.10 that plasmas with a higher impurity density are expected to show a higher fast-ion current drive efficiency. Finally, it should be noted that the plasma density is not contained in this approximation. High densities can influence the current drive efficiency since by frequent collisions, the electrons might not remain on trapped orbits [25].

2.5 Anomalous transport of fast-ions

Anomalous transport of fast-ions denotes all effects that cause a phase space redistribution of fast-ions in addition to the neoclassical transport[3]. Typically, the net anomalous flux of fast-ions, F, is described by a diffusion coefficient, D_x, that acts on the gradient of the fast-ion distribution function $\nabla \vec{n_{fi}}$:

$$\vec{\Gamma} = -D_x \cdot \nabla \vec{n_{fi}} \tag{2.13}$$

The diffusivity is defined in [m^2/s] and can depend on the fast-ion energy, the fast-ion pitch and the position in the plasma.

The anomalous transport is typically caused by temporal or spatial asymmetries in the electric and magnetic fields of a fusion device. The variation in the electric field causes a radial $\vec{E}\times\vec{B}$ drift velocity according to equation 2.5. The variation in the magnetic field yields an enhanced radial transport of particles that propagate along perturbed magnetic field lines. Furthermore, the fast-particles can experience an anomalous transport through resonances. The particles have, due to their high velocities, small collision frequencies and consequently perform several toroidal and poloidal turns before being displaced or significantly decelerated. Thus, they can encounter a given perturbation several times. As an example, trapped particles can be redistributed by a non-axis symmetric magnetic field as the radii of the upper and lower bounce position would vary at different toroidal positions.

The phenomena that cause a spatial or temporal perturbation of the electric and magnetic fields can be classified into magneto hydrodynamic (MHD) effects, small scale turbulence and intrinsic error fields. Intrinsic error fields are asymmetries in the magnetic field configuration. They are present in fusion devices also without the plasma. As an example, the limited amount of magnetic field coils in a toroidal device imposes the so called toroidal field (TF) ripple at the low-field side which can redistribute fast-ions at the plasma edge.

2.5.1 Small scale turbulence

Small scale turbulence typically dominates the transport of thermal particles and energy in fusion plasmas. It is orders of magnitudes larger than the neoclassical transport and limits

[3]The neoclassical transport summarizes the heat and particle transport due to Coulomb collisions and accounts for the particles orbits in a toroidal device.

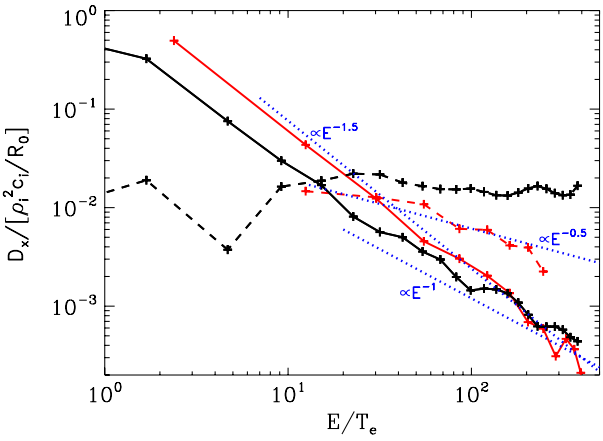

Figure 2.6: Predicted fast-ion diffusion coefficients as a function of the fast-ion energy over the electron temperature. The dashed lines correspond to magnetic fluctuations. The solid lines correspond to electrostatic fluctuations. The figure has been taken from [28].

the achievable temperature gradients in a fusion device. It is responsible for so called stiff temperature profiles [26] and is the reason for the need of large machine sizes to approach the Lawson criterion. Several turbulence regimes exist such as trapped electron modes (TEM), ion temperature gradient modes (ITG), and electron temperature gradient modes (ETG) that reach a non-linear growth phase above a certain critical gradient [27]. The anomalous diffusivities of thermal particles can be up to several m^2/s and the turbulent fluctuations can have large extents along the magnetic field lines. However, electromagnetic fluctuations are localized in the radial directions: The radial size of the turbulent structures, i.e. the turbulent eddies, is in the order of several mm (the order of the gyro radii of thermal ions). Due to this relatively small scale, the anomalous fast-ion transport caused by turbulence can be neglected in a first approximation. The fast-ion orbits average over the turbulent eddies due to their large gyro radii and due to the deviation of drift surfaces from the magnetic field lines.

However, new theoretical results predict that in particular the magnetic fluctuations might affect the confinement of high energetic fast-ions. Figure 2.6 has been taken from [28]. It shows the anomalous fast-ion diffusion coefficient, determined by GENE[4] simulations, as a function of the fast-ion energy relative to the electron temperature, T_e. The solid lines indicate the fast-ion diffusivity for electrostatic fluctuations caused by turbulence. The dashed lines account for magnetic fluctuations and the dotted, blue lines stand for theoretical scalings. As can be seen, the electrostatic diffusivity depends strongly (note the logarithmic scale) on the fast-ion energy ($\propto E^{-1.5}$). The higher the fast-ion energy, the larger are the gyro radii and the deviations from the flux surfaces and the smaller is the diffusion coefficient. In contrast, the diffusion due to magnetic fluctuations does not depend on the fast-ion energy. Therefore, the small scale turbulence might even influence the high energetic fast-ions. Furthermore, figure 2.6 shows that the diffusivity of fast-ions depends on the pitch. The black lines correspond to fast-ions with small absolute pitches. The red lines correspond to fast-ions with large pitches (small gyro radii). As can be seen, the electrostatic diffusivity is smaller for fast-ions with larger gyro radii. In contrast, the magnetic particle diffusivity decreases with increasing pitch.

Experiments at DIIID using FIDA spectroscopy already indicated that a fast-ion redis-

[4]The GENE code can be categorized as gyro-kinetic, Eulerian code. It is typically used to study plasma turbulence and therefore calculates the non-linear, temporal evolution of the distribution function of charged particles in 5 dimensions (the gyro motion is neglected). GENE is based on the Vlasov equation and uses in addition the Poisson equation to determine the corresponding evolution of the electromagnetic fields.

tribution is observed in the presence of micro-turbulence [29]. Furthermore, measurements of the fast-ion driven off-axis current at AUG showed deviations from the expected values which are possibly caused by an anomalous fast-ion redistribution [30]. The newly developed FIDA diagnostic at AUG now enables to verify these findings. Therefore, the effect of small scale turbulence on the fast-ion distribution function is studied in this thesis.

2.5.2 MHD effects

MHD effects summarize a variety of different modes and plasma instabilities. In general MHD modes are driven by pressure gradients, current gradients or by particles under resonant conditions. They can redistribute fast-ions and can be driven by a part of the fast-ion distribution function through so called inverse Landau damping [31]. The MHD effects, which are radially localized and which typically act on a certain part of the fast-ion velocity space, can be sub-classified into resistive and non-resistive effects. Resistive modes, such as magnetic islands [32] or edge-localized modes [33], change the magnetic field topology through magnetic reconnection. Non resistive modes modify the field lines but keep the nested structure of the flux surfaces. While the time scales of the evolution of resistive modes are relatively large (the current diffusion time is typically in the order of ms), the non-resistive modes can evolve much faster. Typical examples of non-resistive modes are kink modes and Alfvén waves. The Alfv́en waves are fluctuations of the magnetic field lines, comparable to the fluctuation of a guitar string that typically do not become unstable and are therefore not categorized as instabilities. However, they can interact with fast-ions, gaining or releasing energy. Thereby they can change the fast-ion distribution function as reported by [34], [35].

Prominent kink modes are internal (m=1,n=1) modes that are located at the q=1 surface [36]. Modes with a poloidal number of m=1 can be present in plasmas as a constant displacement of the flux surfaces does not change the magnetic structure's free energy. The free energy, δW, needed for a constant, internal displacement, ξ, can be approximated for large aspect ratio tokamaks by [7]:

$$\delta W \propto \int_0^a \left[(r\xi') + (m^2-1)\xi^2\right] \left(\frac{n}{m} - \frac{1}{q(r)}\right)^2 r dr \tag{2.14}$$

where a is the minor radius and n and m are the toroidal and poloidal mode numbers. As can be seen, the first term of the integral becomes zero for a constant displacement of a m=1 mode. However, the displacement at the plasma edge needs to be zero as otherwise surface currents would increase the free energy. Hence, there must be a finite gradient of the displacement, ξ' at a certain radius. At the q=1 surface where m and n are one, the contribution of a gradient ξ' to δW is zero because there, the second term in equation 2.14 is zero. Consequently, (1/1) modes with displacements as shown in figure 2.7 can exist.

According to equation 2.14 the magnetic field structure below a safety factor of q=1 would be always unstable. However, the approximation does not account for the kinetic plasma pressure and the fast-ion distribution function which can act as a stabilizing mechanism. Therefore, the (1/1) internal kink mode is often present when the q-profile is below one, but not necessarily.

Two names are assigned to the internal (1,1) kink mode as it appears with two different characteristics: It is on the one hand called fishbone instability when a strong correlation with fast-ions is observed [37]. The fishbones are excited by inverse Landau damping of trapped fast-ions with a resonant toroidal rotation of their bounce positions. The bottom

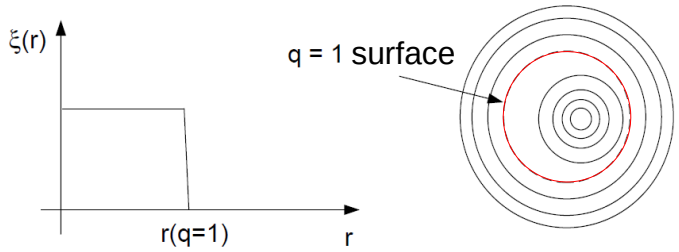

Figure 2.7: q=1 kink mode.

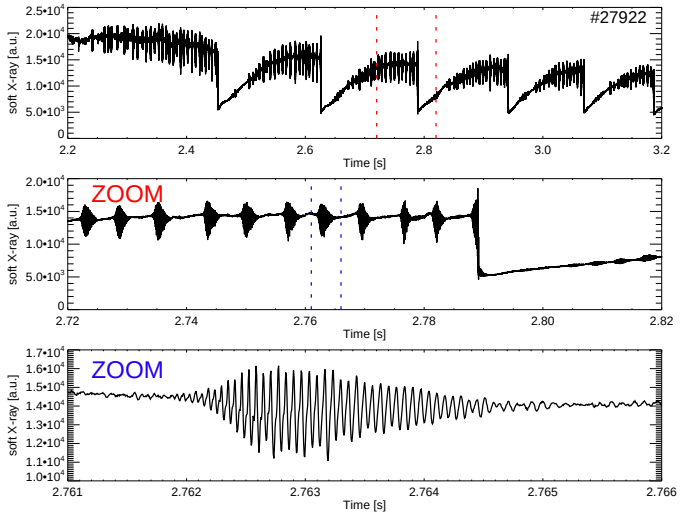

Figure 2.8: Soft X-ray measurement of fishbone modes and sawtooth crashes in ASDEX Upgrade. In the top row, the sawtooth crashes become visible. In the bottom row, which shows a zoom on one single fishbone instability, the fluctuation imposed by this kink mode can be seen.

row of figure 2.8 shows oscillations observed by a soft X-ray diagnostic that are caused by a fishbone. The amplitude of the signal's fluctuation is correlated with the variation of the plasma temperature and density close to the plasma center. The amplitude first increases as the fishbone mode gains energy from the fast-ions. Then, as soon as the mode has redistributed the fast-ions responsible for its growth, its amplitude decreases again.

On the other hand, the (1/1) kink mode is called sawtooth instability when its appearance is followed by temperature crash of the plasma core. As can be seen in the upper row of figure 2.8, sawtooth crashes appear periodically as a relaxation oscillation of the plasma center. The sawtooth redistributes energy, particles and current that are present inside the q=1 surface. After the crash, the plasma parameters recover until the next crash occurs. The fact that not every (1/1) mode causes a sawtooth crash is most likely due to the relatively slow evolution of the current density gradient in the plasma core. Only above a certain current density gradient, the kink mode becomes unstable and crashes. One theory of the sawtooth crash is the Kadomtsev model [38] which is derived from the Sweet-Parker model for magnetic reconnection [39]. It states that the helical component of the magnetic field, $\vec{B}_*$, reconnects during a sawtooth crash. The helical component is defined relative to the helically twisted field lines situated on the q=1 surface. The helical magnetic field has opposite signs inside and outside the q=1 surface. Inside the q=1 surface, the field lines are more twisted than the ones at q=1 while outside, the field lines are less twisted.

The reconnection of this anti-parallel magnetic field component now appears in a narrow layer where the flux surfaces are strongly compressed by the displacement imposed by the

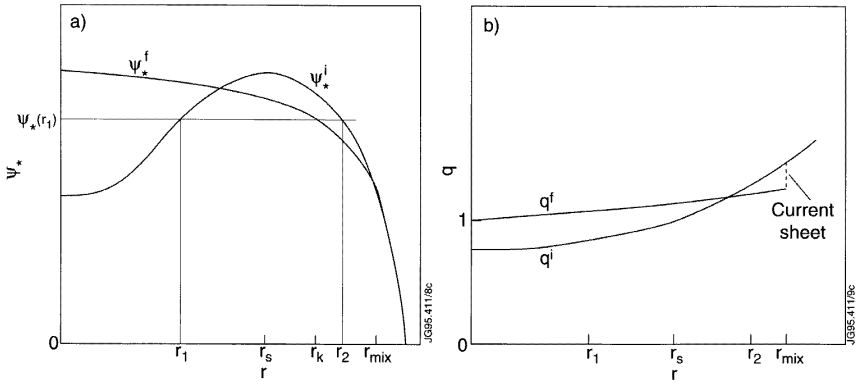

Figure 2.9: a) Radial profile of the helical flux before (ψ_*^i) and after (ψ_*^f) a sawtooth crash as assumed by the Kadomtsev model. Field lines at two radii with the same helical flux (e.g. r_1 and r_2) are supposed to reconnect. At radii larger than the mixing radius, r_{mix}, the field lines do not reconnect. b) Radial q-profiles before and after a sawtooth crash determined by the Kadomtsev model. After the sawtooth crash, the q-profile is above one which corresponds to a helical flux that is maximal in the center. The figure is taken from [40].

(1/1) mode. The reconnection forms a magnetic island that squeezes the nested flux surfaces out of the plasma center. The sawtooth crashes happens very fast because the high pressure in the plasma center enables the electrons and ions to flow with a high velocity into the reconnection layer. The Kadomtsev model predicts the time scales of the crash, which are consistent with the ones observed in small fusion devices. However, in larger experiments, such as ASDEX Upgrade, the observed time scales of the reconnection do not agree with the Kadomtsev model. They are too long. The research on this discrepancy is still ongoing and might in part be explained as the Kadomtsev model does not account for the difference of the gyro radii of electrons and ions that can cause an additional electric field in the reconnection layer.

In addition to the calculation of the time scales, the Kadomtsev model also describes the reconnection of the magnetic field lines and the corresponding redistribution of heat and particles, such as fast-ions. A typical radial helical flux profile present before a sawtooth crash,$\psi_*^i(r)$ is depicted in figure 2.9a that corresponds to the q-profile shown in 2.9b. The helical flux increases from the plasma center to larger radii and has its maximum at the q=1 surface. There, the sign of the helical field reverses. Then it decreases towards the plasma edge. The Kadomtsev model now assumes that a given field line inside the q=1 surface reconnects with a field line outside the q=1 surface, located at the same value of the helical flux. In the example plotted in figure 2.9a, a field line at r_1 would reconnect with a field line at r_2 as there, the helical flux is equal. The radius r_k, which corresponds to the radial position where the reconnected field lines are located after the sawtooth crash, is determined by the conservation of the toroidal flux. The redistribution of heat and particles is finally calculated by assuming that the latter are bound to the reconnecting field lines and that the pressure and the quantity of the particles are conserved. It should be noted that particles and heat are redistributed only up to the mixing radius r_{mix} where the helical flux, before the crash, is equal to that in the center. At larger radii, no change is assumed.

In addition to this basic approach of modeling the redistribution of fast-ions caused by sawtooth crashes, a more sophisticated theory is described in [41]. There, the redistribution of fast-ions is assumed to be mainly caused by the large electric fields associated with the fast change of the helical magnetic field during the reconnection. A dependence of the fast-ion pitch is theoretically predicted that has already been studied at the TEXTOR tokamak by

CTS measurements [42]. There, the measurements indicate that passing fast-ions are more affected by the sawtooth crash than trapped ones.

2.6 The FIDA technique

In this section, an introduction to the FIDA technique is given which is used in this Ph.D work to study the confinement of fast-ions. It is similar to spectroscopic measurements of fast alpha particles [43] performed at the JET tokamak and was first implemented at DIII-D [44]. The technique is a charge exchange recombination spectroscopy method (CXRS) [45] which is applied to fast D-ions. Through charge exchange reactions with neutrals in the plasma, mainly present along the path of NBI, the fast ions can capture an electron into an excited quantum state, become neutral themselves, and subsequently emit line radiation. The radiation is well localized because it is typically emitted before the neutralized fast ions (fast neutrals) move by more than a few centimeters. The de-excitation back to the equilibrium happens very quickly.

Several spectral lines from the fast neutrals exist in fusion plasmas. However, FIDA measurements tend to use the Balmer Alpha emission line (λ_0 = 656.1 nm, n=3 to n=2) because it permits the use of standard lenses and spectrometers as it is in the visible range.

The FIDA emission is localized mainly along the path of the NBI as there is no significant overlap of fast ions and neutrals elsewhere. Hence, multiple lines of sight (LOS) that intersect neutral beams at different radii can be used to obtain profile information. Information on the velocity distribution of fast ions is contained in the spectral shape of FIDA radiation. The shape is dominated by the Doppler effect which depends on the velocity vector of the fast neutrals, $\vec{v_n}$, and on the unit vector along a line of sight $\vec{e_p}$:

$$\Delta\lambda_{Doppler} = \lambda_0 \frac{\vec{v_n} \cdot \vec{e_p}}{c} \tag{2.15}$$

here, c is the speed of light and λ_0 is the un-shifted wavelength. The Doppler Effect shifts the D-alpha emission considerably in wavelength. The spectral shape of the FIDA emission has consequently broad spectral wings. It deviates significantly from a Gaussian curve because fast ions do not follow a Maxwell distribution. It should be noted that the properties of the Doppler Effect make an energy and pitch resolved measurement difficult. That is to say, one cannot relate a specific shift in wavelength to an unique energy as fast ions with higher energies and different pitches can result in similar shifts. Information on fast-ion density profiles is contained in the measured spectral radiances. The FIDA radiance is proportional to the density of neutralized fast-ions in the n=3 state present along a LOS. This density depends not only on the fast-ion density, but also on the probability for charge exchange and on the mechanisms that populate the n=3 state. The probability, $prob_m$, for a fast ion to undergo a charge-exchange reaction in which the electron ends up in the atomic state, m, is:

$$prob_m = \sum_n \sum_k d_{NBI(n,k)} \cdot \sigma_{cx(n\rightarrow m)}(v_{rel}) \cdot v_{rel} \tag{2.16}$$

where $d_{NBI(n,k)}$ is the density of injected beam and halo neutrals present along the NBI with different atomic states, n, and energies, k, $v_{rel}(k)$ is the relative velocity between fast ions and neutrals and $\sigma_{cx(n\rightarrow m)}(v_{rel})$ is the energy dependent charge-exchange cross-section. All of the various neutral beam energy components and atomic states as well as the halo population have to be accounted for separately because the charge-exchange cross-sections depend on atomic states and energies.

The halo neutrals originate from charge exchange reactions between the injected beam neutrals and the thermal D-ions (the bulk plasma ions). Due to these reactions as well as subsequent charge exchange reactions of the halo neutrals with thermal D-ions, a cloud of neutrals surrounding the NBI is built whose density is typically comparable or even larger than the beam neutral density. The NBI halo density is important for FIDA measurements because the high collision energy between the fast ions and the halo neutrals provides a significant probability for charge exchange reactions.

A considerable fraction of fast neutrals are in the n=3 state directly after charge exchange. Additionally, the n=3 state can be populated by the radiative decay from higher states that have been populated by charge exchange or other mechanisms. Furthermore, fast neutrals in lower states can be excited into the n=3 state by collisions along their path through the plasma. This effect yields non-localized FIDA radiation but, fortunately, does not strongly limit the spatial resolution of the technique. The FIDA radiation emitted in the equilibrium state (through collisions) is comparably small. The radiation which is emitted directly after charge exchange is more intense as the charge exchange reaction strongly overpopulates the excited states.

The interpretation of FIDA spectra is difficult. In particular, the moderate resolution in the velocity space (one cannot resolve information on the energy and pitch of fast ions independently) and the energy dependent charge exchange cross sections make a direct deconvolution of a single FIDA measurement to a fast-ion distribution function virtually impossible. Two different methods can be applied when analyzing FIDA measurements to circumvent this difficulty: First, by assuming that the fast-ion velocity space is unchanged and by calculating the density profiles of the beam and halo neutrals, changes in the FIDA radiation can be interpreted as variations of the fast-ion density. Hence, the evolution of the fast-ion distribution can be studied e.g. in the presence of MHD activity.

Second, a forward model can be used to quantitatively interpret FIDA measurements. By simulating the neutralization and photon emission of fast ions that correspond to a given distribution function, it is possible to calculate synthetic FIDA spectra. These can then be compared to the measurement. The theoretical distribution functions of fast-ions can be determined by a solution of the Fokker Planck equation [46] or by using a Monte Carlo code, such as TRANSP, that simulates fast-ion orbits and the collisions with electrons and ions.

2.7 Simulation of fast-ion slowing-down distribution functions by TRANSP

The theoretical fast-ion distribution functions shown in this and the following chapters have been determined by TRANSP [47]. TRANSP is, as its name indicates, a transport code that is typically used to calculate quantities such as neutron rates, energy confinement times, the local diffusion coefficients of ions and electrons or the magnetic field line angles on a time dependent basis. The code is maintained and run at the Princeton plasma physics Laboratory (PPPL) and can be accessed from outside via a user interface. TRANSP can be operated in a predictive or an interpretative mode concerning the kinetic plasma profiles[5]. When using TRANSP to predict the fast-ion distribution function it is mainly executed in the interpretative mode. The evolution of the plasma current, information on the geometry, power and timing of the heating and current drive sources, the evolution of the kinetic

[5]Radial profiles of the electron temperature, ion temperature, electron density, plasma rotation and the effective charge.

plasma profiles and the positions of the last closed flux surface are the required inputs. The deposition profiles of the heating sources, the power radiated by the plasma and the evolution of the magnetic field are computed by TRANSP.

To model the heating and current drive from NBI, TRANSP uses a module called NUBEAM. NUBEAM is a Monte Carlo code that determines the deposition position of multiple NBI markers (e.g. 10^5) in five dimensions (three spatial and two velocity space coordinates). It then simulates the corresponding fast-ion orbits and their slowing down evolution as a function of time and in two spatial dimensions, i.e. in the poloidal plane. The orbits are simulated in the gyro center approximation whereby losses of unconfined orbits[6] and neutralization losses are taken into account. The fast-ion collisions with electrons and ions are taken into account by a collision operator. The latter models the drag force imposed by the electrons and uses a Monte Carlo approach to determine the direction into which a given fast-ion is scattered by collisions. New fast-ion deposition profiles are typically determined every 10ms and are then added to the simulation of the fast-ion orbits. Thereby, the evolution of the fast-ion density can be studied e.g. after turning on NBI. The quantity of simulated ions does not infinitely increase by adding new fast-ions to the simulation because the code stops simulating slowed down fast-ions as soon as their energy is below 3/2 of the local ion temperature.

Non-classical fast-ion slowing down distributions can be simulated by defining an anomalous diffusion coefficient which can depend on the time, the radial position and on the fast-ion energy. By applying this anomalous diffusion, additional radial random kicks to the fast-ions are simulated which results in an anomalous fast-ion transport.

To output fast-ion distribution functions, the user needs to define time-ranges for which an average distribution of the simulated fast-ions is calculated. It should be noted that the resulting fast-ion distribution functions are given in terms of the radial and vertical coordinate, the energy and the solid angle Ω divided by 4π. To convert this phase space to a function of the fast-ion pitch, the fast-ion distribution functions from TRANSP need to be multiplied by 0.5.

[6]TRANSP is supplied with a simplified geometry of the vacuum vessel of ASDEX Upgrade. As soon as a simulated fast-ion hits the inner surface of this vacuum vessel, it is defined as a orbit loss and is not simulated any longer.

Chapter 3

The experiment ASDEX Upgrade

This chapter gives an introduction to the fusion experiment ASDEX Upgrade (AUG). The main parameters and the history of the experiment are described in the first part. Then, the additional heating systems and the main diagnostics used during this Ph.D. thesis are presented.

3.1 Overview

ASDEX Upgrade is situated in Garching at the Max Planck-Institut für Plasmaphysik (IPP) and went into operation in 1992. It is Germany's largest operating fusion device with a major radius, R_0, of 1.65 m and a minor radius, a, of 0.5 m. The toroidal magnetic field, B_T, is typically -2.5 T in the plasma center and is directed clockwise. It is created by 16 toroidal field (TF) coils, each defining one sector of the machine. The poloidal magnetic field is generated by a counter clockwise directed plasma current I_p [0.6-1.4 MA] that is mainly driven by a central transformer coil. The vertical position of the plasma is controlled using a passive stabilizing loop (PSL) and active vertical field coils.

Furthermore, external coils are used to balance the varying magnetic field from the transformer coil and to generate an elongated, triangular shaped magnetic field structure as circular plasmas are less stable versus MHD modes. The first, i.e. inner, wall of the experiment is made of tungsten coated graphite tiles which tolerate large heat loads and which have a high sputtering threshold. The generated plasmas mainly consist of deuterium, as tritium would activate the machine and as hydrogen is less fusion reactor relevant. Plasma densities between 10^{19} and 10^{20} electrons per m^3 can be achieved and temperatures can reach up to 25 keV. The duration of plasma discharges[1] is up to 10 seconds which is a multiple of the global confinement time $\tau \sim 100$ ms. The mostly used operational regime is the high confinement mode (H-mode) [48] which typically develops above a certain heating power and which results in a steepening of the edge temperature gradient. Thereby the energy confinement of the plasmas is significantly increased. The H-mode has first been observed at ASDEX, the predecessor of ASDEX Upgrade. ASDEX was a slightly smaller machine operated from 1982 to 1990. Its name is derived from the german 'Axial Symmetrisches Divertor EXperiment' which refers to a special magnetic field topology which was successfully tested at that machine and that is also foreseen for ITER. In the divertor configuration, the outermost flux surfaces are not closed but end in the divertor region (see right plot of figure 3.3). Particles expelled from the plasma do, consequently, not impact on neighboring walls

[1] Plasma experiments in fusion devices are also called discharges.

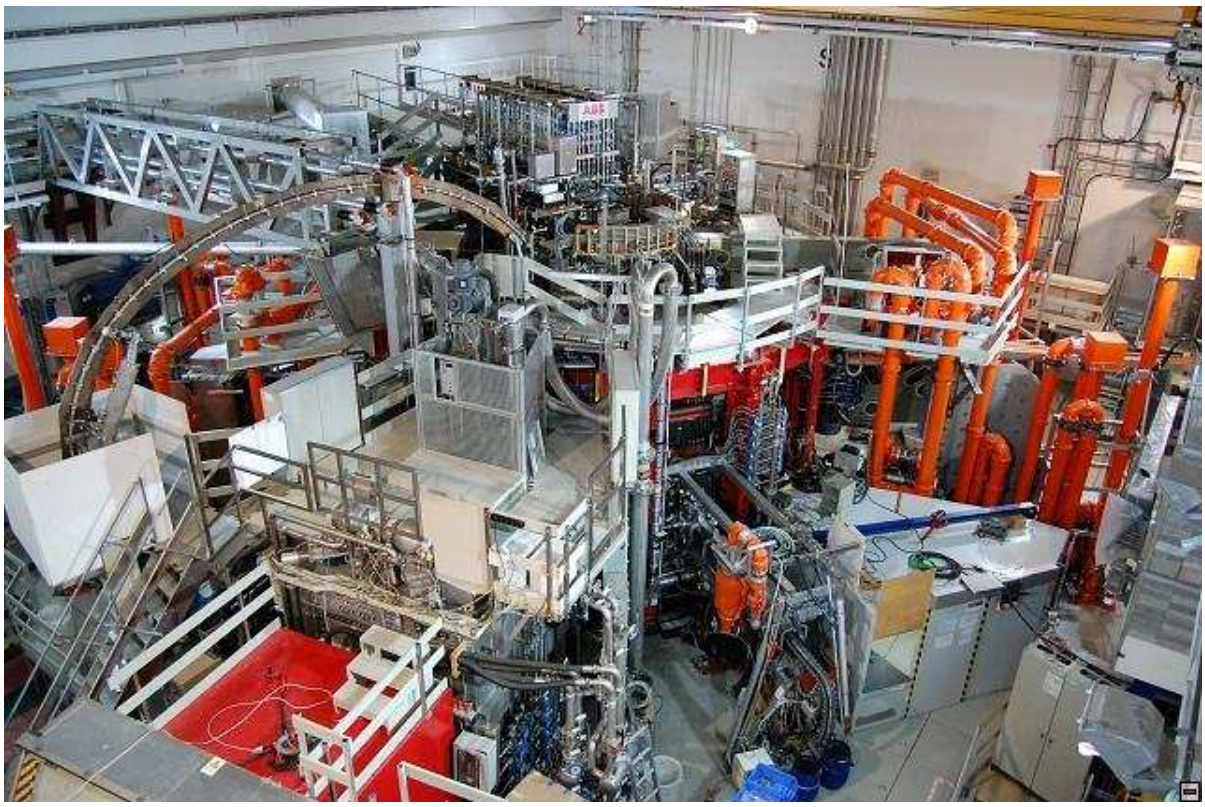

Figure 3.1: Torus hall of ASDEX Upgrade.

but are guided into the divertor region where they are slowed down by a high density. With the divertor concept, the influx of sputtered wall material is significantly reduced and plasmas with smaller impurity contents are obtained. The plasmas are consequently less cooled by impurity line radiation yielding higher energy confinement times and temperatures.

3.2 Additional heating systems

ASDEX Upgrade has a very powerful and flexible heating system. Besides ohmic heating from the plasma current, AUG plasmas can be heated by electromagnetic waves (ICRH and ECRH) and by neutral beam injection (NBI) with a power of up to 33 MW.

3.2.1 Neutral beam heating

The neutral beam injection system at AUG consists of four NBI sources located in sector 15 (box 1) and of four NBI sources located in sector 7 (box 2). Each source typically injects Deuterium neutrals with a power of 2.5 MW. As shown in figure 3.4, the four sources located in sector 15 are named NBI 1-4 and have a full injection energy of 60 keV. The sources in sector 7 are named NBI 5-8 and have a full injection energy of 93 keV. The species-mix in terms of particles of box 1 is in the range of 0.47 : 0.36 : 0.17 for the full, half and one third energetic neutrals. The species-mix of box 2 is 0.43 : 0.39 : 0.18. The full width at half maximum of the beams is in the order of 22 cm. The ion sources of the beams are located at radii between 9.3 m and 9.8 m and have a half width of 11cm and a half hight of 22 cm. The horizontal and vertical focuses are located at a distance of 6.5 m and 8.5 m from the sources respectively. The divergences of the injectors are in the range of 0.7 degree. For NBI

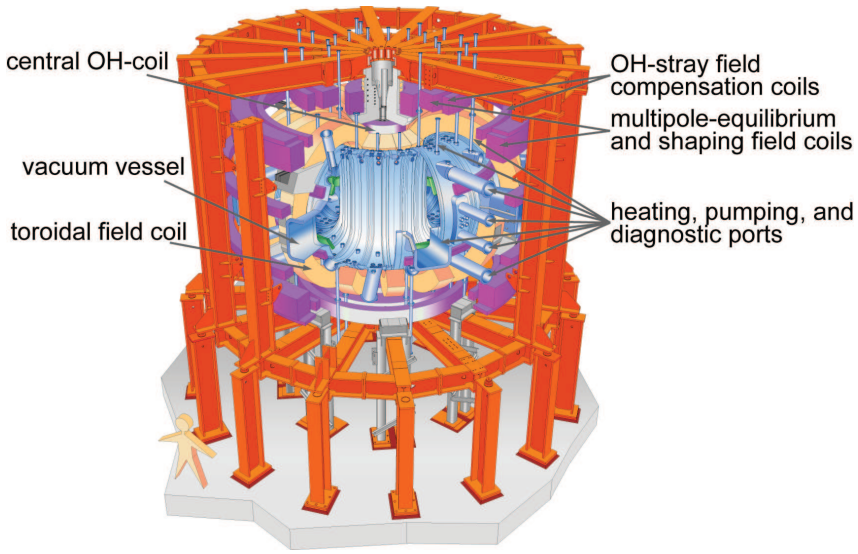

Figure 3.2: Overview of the ASDEX Upgrade fusion experiment. The 16 toroidal field coils are indicated in orange. The coils used to determine the plasma shape and to generate the plasma current are shown in purple.

3, the divergence has been determined by the means of spectroscopy and is 0.59, 0.62 and 0.71 degree for the full, half and third energetic neutrals. Of particular interest are sources NBI 6 and NBI 7 which have an off-axis, tangential geometry and can therefore be used for NBI current drive studies. Furthermore, NBI 3 is essential for this Ph.D. work as the FIDA diagnostic is focused on this neutral beam injector.

3.2.2 Ion cyclotron resonance heating

The ion cyclotron resonance heating (ICRH), i.e. radio frequency (RF) heating, accelerates ions by electromagnetic waves with frequencies in the range of several tens of MHz (see equation 2.2). The high frequencies, produced by four generators with 2 MW each, are transmitted to antennas that are situated close to the plasma. In the right photo shown in figure 3.3, one antenna of AUG can be seen. It is located behind shielding stripes that are tilted along the direction of the magnetic field lines. AUG has in total four ICRH antennas, shown in figure 3.4, that can heat plasmas with a coupled power of up to 7.2 MW. At AUG, the ICRF system is typically adjusted to accelerate the hydrogen minority present in the deuterium plasmas (3-6%) at $\sim$ 36 MHz because it is not possible to couple the RF heating into the plasma at the frequency of deuterium ions.

3.2.3 Electron cyclotron resonance heating

Electron cyclotron resonance heating (ECRH) accelerates electrons and is operated at higher frequencies than the ICRH system because the cyclotron frequency depends on the mass of the gyrating particles. At AUG the ECRH system is operated at a frequency of 140 GHz or 105 GHz which corresponds to the second harmonic of the cyclotron frequency of electrons at -2.5 T or -2.0 T respectively. The microwaves are generated by gyrotrons and are guided to the experiment by wave-guides where the radiation can be deposited at different vertical positions by using turnable mirrors (see figure 3.3). The ECRH deposition position is radially localized because the waves are only resonant at a given magnetic field strength which is mainly determined by the radially decreasing toroidal field. During this Ph.D. thesis, 6

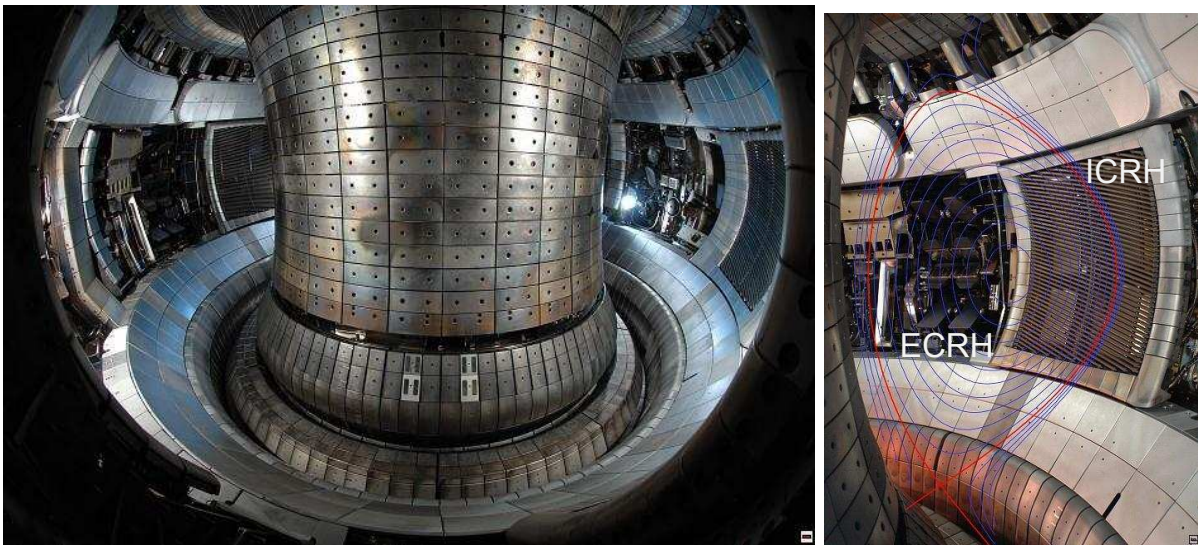

Figure 3.3: Photos from the inside of the machine. The right photo is combined with flux surfaces. As can be seen, the outermost flux surfaces, shown in blue, end in the upper and lower divertor. An ICRH antenna and the movable mirrors of the ECRH system can be seen in the right figure.

different gyrotrons were available with a total heating power of up to 4 MW. It should be noted that the ECRH system is very important for the operation of AUG because it helps to prevent from the accumulation of heavy impurities such as tungsten in the plasma core. By applying localized ECRH, the local level of turbulence is increased and impurity ions are expelled.

3.3 Diagnostics

ASDEX Upgrade has about 70 different diagnostics that are routinely operated to investigate and monitor the behavior of the machine and the plasma. As a detailed description of every diagnostic would be out of the scope of this work, the following section focuses on the diagnostics which have been used to characterize the discharges analyzed in this thesis.

3.3.1 Magnetic equilibrium

The magnetic equilibrium defines a field line structure where the net force perpendicular to the magnetic surfaces is zero. The equation on which the equilibrium is based can be approximated under simplified conditions by:

$$\vec{j} \times \vec{B} = \vec{\nabla} p \tag{3.1}$$

where $\vec{j}$ is the current density, $\vec{B}$ is the magnetic field and $\vec{\nabla} p$ is the pressure gradient. Following equation 3.1, the plasma pressure in the equilibrium is constant on flux surfaces. This is very useful when analyzing plasma discharges because in the magnetic equilibrium, the localized measurements of the kinetic plasma profiles can be compared by using a one-dimensional normalized flux coordinate:

$$\rho = \sqrt{\frac{\Psi - \Psi_{axis}}{\Psi_{separatrix} - \Psi_{axis}}} \tag{3.2}$$

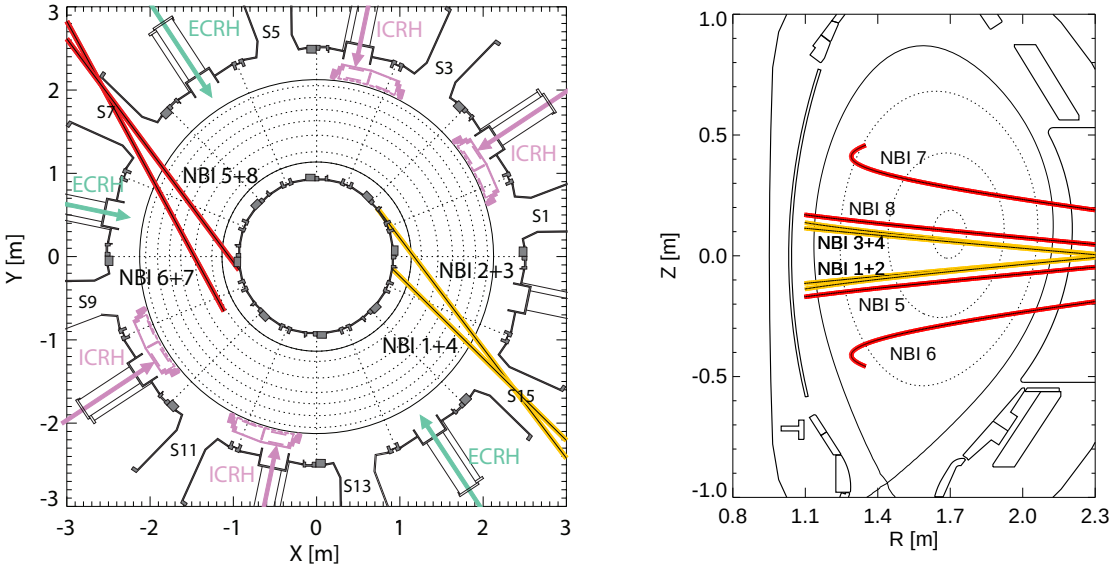

Figure 3.4: Top-down and poloidal view on the ASDEX Upgrade tokamak indicating the different heating sources.

where Ψ is either the poloidal or the toroidal magnetic flux. The coordinate is per definition zero in the plasma center (axis) and one at the last closed flux surface (separatrix). At AUG, the equilibrium is calculated by the CLISTE [49] code which solves the Grad-Shafranov equation [50] that is derived from equation 3.1 for a toroidal geometry. For the solution of the Grad-Shafranov equation, CLISTE performs an iterative approach and uses information from several magnetic measurements. It uses the information from 63 magnetic pick up coils that measure the local poloidal magnetic field at their position (see figure 3.5). Furthermore, the information of 18 flux difference measurements as well as information on the currents in the TF-coils, the ohmic transformer, the poloidal shaping coils and the PSL are used. Unfortunately, the uncertainties of the routinely determined equilibria are large concerning the current profile in the plasma center. However, it is possible to calculate more sophisticated equilibria by supplying CLISTE with the kinetic plasma pressure (also consisting of the fast-ion pressure), with currents that flow in the divertor and with field line angles from MSE measurements.

3.3.2 MSE

The motional stark effect (MSE) diagnostic is used to determine the angles of the field lines. It is based on the observation of the Balmer alpha emission of the injected beam neutrals. The emission is split into π and σ Stark lines caused by the $\vec{v}\times\vec{B}$ electric field (see chapter 4). By analyzing the direction of the polarization of the π and σ lines, it is possible to infer the local B-field angle. The MSE diagnostic at AUG is focused on NBI 3 and uses interference filters and photo multipliers to study one component of the beam emission spectrum. Within the optics, a polarization filter and two photo elastic modulators (PEM) are situated. The latter rotate the polarization of the incoming light depending on the time (the phase of the modulator) and on the initial direction of the polarization. By analyzing the temporal evolution of thereby modulated signal, the field line angles are determined.

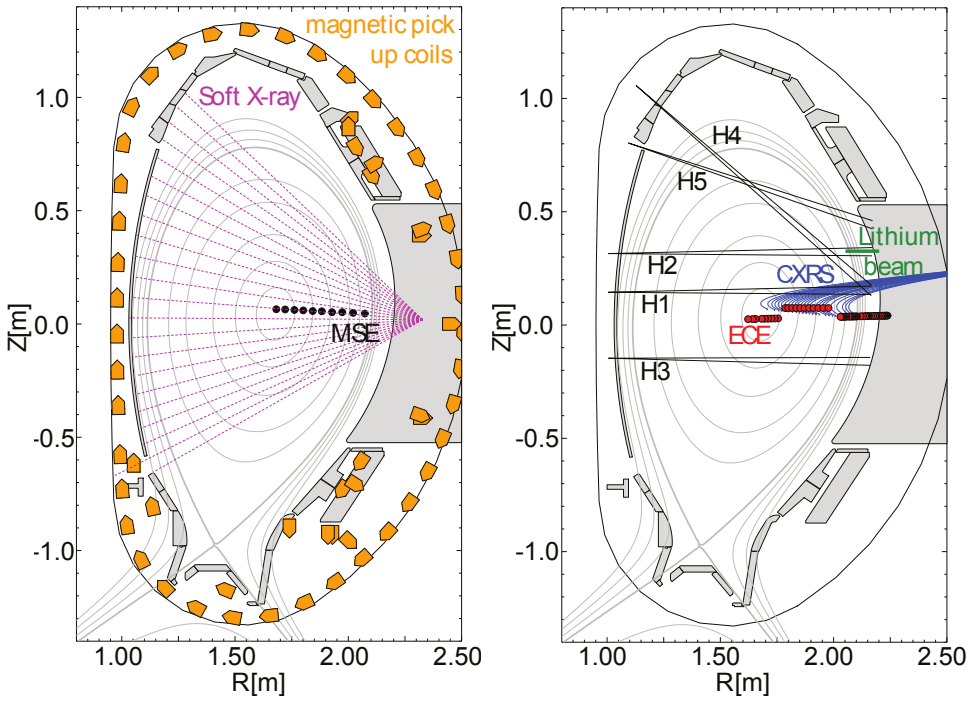

Figure 3.5: Poloidal view on AUG with the different diagnostics used in this thesis.

3.3.3 Electron temperature

The electron temperature is measured by the electron cyclotron emission (ECE) diagnostic with a high temporal resolution (up to 1 MHz). The diagnostic observes the cyclotron radiation of gyrating electrons along its viewing direction. The radial position of the observed cyclotron radiation depends on the frequency as the latter is a function of the magnetic field strength. As the magnetic field strength is dominated by the known toroidal field, the measurement positions, as indicated in figure 3.5, are well defined.

At the position of the so called resonance of a given frequency, the plasma is optically thick which means that Planck's law can be applied to infer the electron temperature from the intensity of the measured radiation. The optically thick layer furthermore provides a good spatial resolution of the measurement (few mm). Radiation that is emitted at the same frequency further apart from the diagnostic, e.g. due to a Doppler shift, is absorbed in the optically thick layer.

3.3.4 Electron density

The electron density profiles used in this work are taken from an integrated data modeling approach, IDA [51] that combines the measurements of two diagnostics. On the one hand, the line integrated measurements from interferometry are used to obtain information on the electron density in the plasma core. As can be seen in figure 3.5 five (H1 to H5) laser beams are used to determine the line integrated electron density. The laser beams pass through the plasma and experience a phase shift relative to a second beam that does not propagate through the plasma. By analyzing the interference pattern between the two lasers, the line integrated electron density can be determined. On the other hand, a Lithium beam diagnostic measures the electron density at the plasma edge. Lithium neutrals are injected into the plasma with injection voltages of up to 50 keV at about 30 cm above the mid plane (indicated in green in 3.5). The lithium neutrals are excited and ionized when penetrating

into the plasma. The ionization, the excitation and subsequent photon emission depend mainly on the electron temperature and electron density. Knowing the electron temperature from the ECE measurement, the radial profile of the light intensity of the injected lithium neutrals is used to calculate the electron density. The time resolution of the lithium beam diagnostic limits the time resolution of the electron density profiles computed by IDA. It is in the order of 1ms.

3.3.5 Ion temperature and plasma rotation

The ion temperature and the plasma rotation are inferred from impurity charge exchange recombination spectroscopy measurements (CXRS) [45]. The diagnostic technique is similar to the FIDA technique whereas the charge exchange radiation of impurity ions, A, such as carbon and boron is analyzed:

$$A^{Z-} + D^0 \rightarrow A^{(Z-1)-\,*} + D^- \tag{3.3}$$

As can be seen, a fully stripped impurity ion with charge number, Z, undergoes a charge exchange reaction with a neutral, D^0. The impurity ion thereby catches an electron with a high probability into an excited state and the D-neutral is ionized. During the subsequent de-excitation of the impurity ion, line radiation is emitted. By using lines of sight that intersect a given neutral beam at different radial positions, this so called charge exchange radiation can be observed spatially resolved. From the spectral width of the radiation of a given impurity line emission, information on the ion temperature is obtained. The plasma rotation can be determined from the measured spectral shift of a given line emission and by accounting for the diagnostic's viewing geometry.

The CXRS method uses the charge exchange radiation from impurity ions instead of radiation from the main plasma ions because it is easier to analyze: The spectra of impurity ions do not contain the beam emission and no FIDA emission. Furthermore, the passive contributions from the plasma edge are less dominant for impurities than for main ions.

At ASDEX Upgrade a CXRS diagnostic with a time resolution of up to 3.5 ms, called CER, is used that has 25 radially distributed LOS. The LOS are, as indicated in figure 3.5, focused on NBI 3 and cover radii from the plasma edge to the plasma center. Typically, the charge exchange radiation from boron ions (BV: 494.47 nm) and from carbon ions (CVI: 529.06 nm) is analyzed.

3.3.6 Effective charge

The effective charge profiles are determined at ASDEX Upgrade by analyzing the level of Bremsstrahlung radiation that is contained in the spectra measured by the CER diagnostic (see previous subsection). An integrated data modeling approach is used to infer Z_{eff} because the Bremsstrahlung is a line integrated value that in addition depends on the electron temperature and density [52]. The uncertainties of the Z_{eff} profiles are relatively high as the calculation combines the uncertainties of the electron temperature and the electron density measurements as well as the noise contained in the spectra of the CER diagnostic.

3.3.7 Soft X-ray

The soft X-ray diagnostic measures energetic radiation emitted by the plasma in the energy range above 1 keV by multiple viewing lines. The radiation originates from line emission of

heavy impurity ions as well as from Bremsstrahlung. Its intensity depends on the impurity content, the electron density and the electron temperature. The radiation is observed by 7 pin hole cameras where each camera defines multiple viewing lines. The pin hole cameras consist of several diodes and a 75 μm thick beryllium filter foil to block radiation with energies below 1 keV. The diodes observe an energy integrated total radiation power with an energy dependent detection probability. The time resolution of the soft-X ray measurement is up to 2 MHz. The spatial resolution of every line of sight is of the order of 1cm. It is defined by the size of the pinhole and its distance to the diode. In figure 3.5, the viewing geometry of one of the soft X-ray cameras is depicted.

Chapter 4

Forward modeling by F90FIDASIM

A Monte Carlo code called FIDASIM [53] is used to model the density and spectra of beam, halo and FIDA-neutrals (neutralized fast-ions). It has been implemented at ASDEX Upgrade since 2009 and was modified and rewritten in Fortran90 and is now called F90FIDASIM. The code has been parallelized to be able to work simultaneously on several CPU's and a new approach to determine the density and spectral emission of halo neutrals was developed which models the charge exchange processes among halo particles in greater detail. Furthermore, the possibility to routinely determine the level of Bremsstrahlung has been added to validate the predicted spectra. The time dependent collisional radiative model of F90FIDASIM that describes the attenuation, excitation and photon emission of Deuterium neutrals has been extended and updated. Corrected and up-to-date cross-sections up to the atomic state n=12 have been added and a new, analytical solution has been implemented. Moreover, a new approach to simulate FIDA spectra has been made that uses 'weight functions' instead of a Monte Carlo approach. Thereby, the determination of FIDA spectra is much faster and a tomographic inversion of the 1D measurement data becomes possible. The new code, now called F90FIDASIM has been validated by comparisons to a beam imaging diagnostic, a beam emission spectroscopy diagnostic and to predictions from TRANSP and ADAS. Furthermore, a sensitivity study has been carried out to illustrate the uncertainties of predicted beam, halo, Bremsstrahlung and FIDA spectra that are caused by uncertainties of the kinetic plasma profiles that are input to the code.

In this section, first a detailed description of the code is presented. Then, the validation of F90FIDASIM and the already mentioned sensitivity study are discussed. The last section of this chapter finally gives a short summary.

4.1 Description

The noise and achievable resolution of FIDA measurements makes a direct conversion of the measurement to a 2D fast-ion velocity distribution very difficult. Therefore, forward modeling is needed when analyzing the measurements quantitatively. At ASDEX Upgrade, F90FIDASIM is used for this purpose that translates theoretical fast-ion distribution functions into spectra. The code has originally been written in the IDL programming language by William Heidbrink [53] and has been further developed and rewritten in Fortran90 in the framework of this Ph.D. thesis. It works on a three dimensional simulation grid and models the attenuation, excitation and radiation of neutrals for single time points. F90FIDASIM contains atomic rates and cross-sections, the NBI parameters and the FIDA diagnostic's

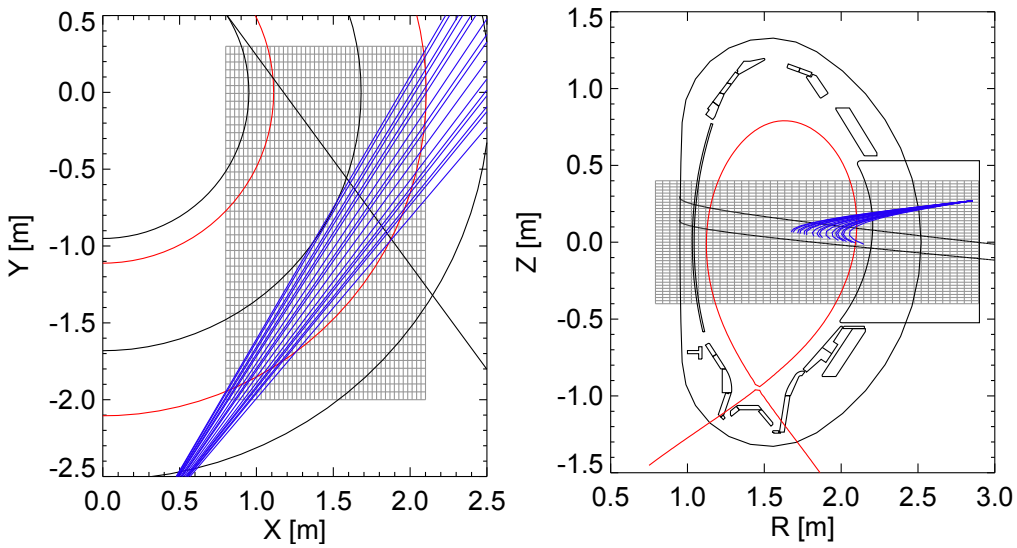

Figure 4.1: Top-down and poloidal view on the AUG tokamak. The separatrix and the flux surfaces are indicated in red color. The simulation grid, which is illustrated in gray, is arranged along the LOS of the FIDA diagnostic with cell-sizes of 3 cm. In the top-down view, the separatrix is shown at z=10cm.

geometry. It needs to be provided with information on the fast-ion distribution function, the magnetic equilibrium, and kinetic plasma profiles. The code's main routines first model the beam and halo neutrals because their densities are needed to calculate the charge exchange probabilities of fast-ions. Then, the radiation from Bremsstrahlung and the FIDA radiation are calculated. It should be noted that F90FIDASIM only simulates, with the exception of Bremsstrahlung, the active components that are only present when NBI is on. The passive components present without NBI, such as the radiation from cold neutrals at the plasma edge or passive FIDA radiation, are not modeled.

Detailed information on the inputs and on the three dimensional simulation grid is presented in the first part of this section. Then, the basic Monte Carlo approach of F90FIDASIM to determine the densities and spectra of Deuterium neutrals is discussed. The simulation of beam and halo neutrals is described in the subsequent sections, followed by the discussion of two approaches that model the FIDA radiation: On the one hand, the standard Monte Carlo approach to model FIDA spectra is introduced. On the other hand, a new method that uses weight functions is described. Finally, the collisional radiative model of F90FIDASIM and the determination of the charge exchange neutralization rates of fast and thermal D-ions are discussed.

4.1.1 Inputs and the simulation grid

F90FIDASIM works on a 3D grid that is located along the LOS of the FIDA diagnostic and that is defined in machine coordinates (xyz). Figure 4.1 shows, as an example, a radial and a top-down view on the AUG tokamak indicating the simulation grid in gray, the NBI path in black, the FIDA diagnostic's toroidal LOS in blue and the separatrix in red. The dimension of the simulation grid is selected such that all LOS within the separatrix are covered[1] and the cell sizes are typically set to 3 cm in the x, y and z directions. The geometry and parameters of NBI are read from the AUG shot-file system because the energy, power, species mix and the injection geometry depend on the experimental program. The geometry of the FIDA diagnostic is defined by vectors that point along the LOS and by the position

[1]This is needed in particular when calculating the radiation from Bremsstrahlung.

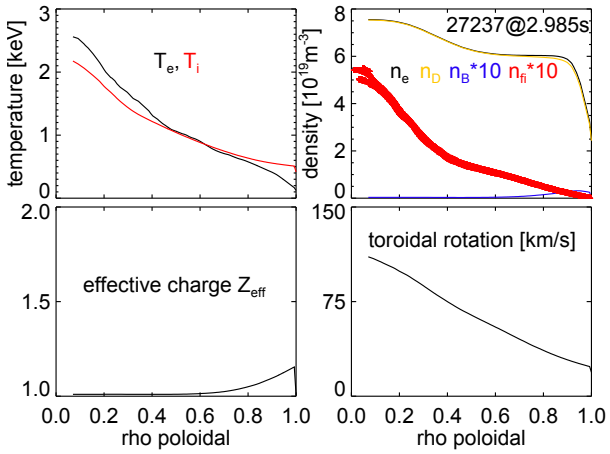

Figure 4.2: Kinetic plasma profiles of discharge #27237 at 2.98s that are input to F90FIDASIM. The Electron temperature, the electron density and the effective charge profiles are taken from integrated data analysis [55]. The ion temperature and the plasma rotation are taken from charge exchange measurements that use boron as impurity. Fast-ion density, shown in the top right box in red is taken from a TRANSP simulation.

of the diagnostic's optical head. The intersection lengths between the cells and the LOS are calculated in the load/input routines as they are needed when calculating line-integrated spectra in the main routines. The magnetic field vectors and the normalized poloidal flux are taken from CLISTE equilibrium reconstructions [54]. Profiles of the kinetic plasma parameters, i.e. the electron density, the electron temperature, the ion temperature, the plasma rotation and the effective charge (Z_{eff}) are read from files that are also input to TRANSP simulations and that are routinely generated. These so-called u-files contain fits on the experimental data as a function of flux coordinates and combine the measurements of several diagnostics (described in chapter 3). The impurity and D-ion densities are determined from the Z_{eff} and electron density profiles. By assuming only one main impurity species (boron in the case of AUG plasmas), the following equation is applied in the load-routines of F90FIDASIM:

$$d_{\mathrm{imp}} = \frac{Z_{\mathrm{eff}} - 1}{q_{\mathrm{i}}\ (Z_{\mathrm{i}} - 1)}\ d_{\mathrm{el}} \tag{4.1}$$

where, d_{imp} is the impurity density, Z_{i} is the atomic charge number of the impurity species and d_{el} is the electron density. It is possible to use only one main impurity as long as one deals only with low-Z impurities such as carbon, boron, nitrogen and oxygen because the cross-sections for these particles do not differ significantly. With the knowledge of the impurity density, the ion density, d_{ion}, can be expressed by:

$$d_{\mathrm{ion}} = d_{\mathrm{el}} - Z_{\mathrm{i}}\ d_{\mathrm{imp}} \tag{4.2}$$

After having collected the kinetic plasma profiles, as shown in figure 4.2, the data is mapped on the simulation grid. Then, the code collects the theoretical fast-ion distribution function. The fast-ion distribution functions are determined by the TRANSP code which simulates for predefined time points fast-ion phase-space densities as a function of the pitch, the energy, the radial and the vertical coordinates. By knowing the radial and vertical coordinates of every grid cell, the 2D velocity space distribution of fast-ions is mapped on the simulation grid. It should be noted that the load-routines of F90FIDASIM are written in the IDL programming language. To pass the inputs to the main Fortran routines, the data is stored in binary files.

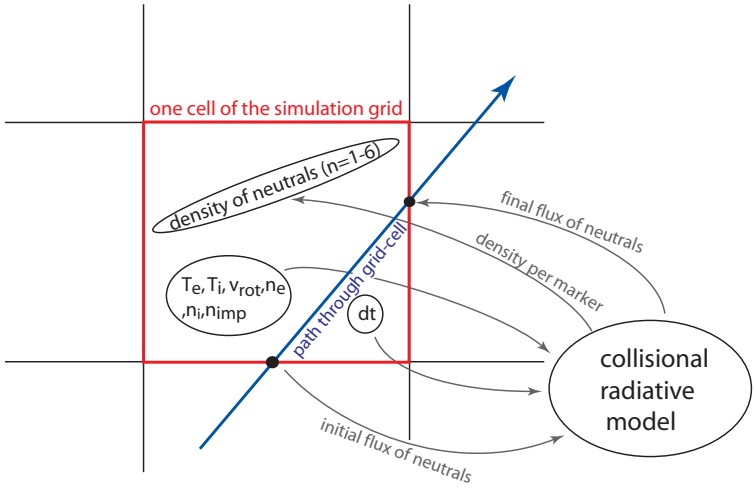

Figure 4.3: Schematic illustration of the application of the collisional radiative model in F90FIDASIM. The solution of the collisional radiative model yields the flux of neutrals in states n=1-6 that enter into the next cell and a density of neutrals per cell.

4.1.2 Basic approach for modeling the beam, halo and FIDA neutrals

Before describing the simulation of the beam, halo and FIDA[2] neutrals, first the basic Monte Carlo approach of F90FIDASIM is presented. It is used to determine the spectra and densities of D-neutrals and can be applied for the beam, halo and FIDA neutrals because these neutrals only differ in their velocity distribution. The basic approach is based on the simulation of the trajectories of Monte Carlo markers through the simulation grid. As the markers represent neutrals which are not influenced by magnetic fields, their trajectories are described by straight lines. The markers represent a certain flux of neutrals in the different atomic states (n=1 to n=6). In every grid cell along their path, the change of the flux of neutrals is calculated by the time-dependent collisional radiative model of F90FIDAISM. The latter is described in detail in section 4.1.8 and models the ionization, charge exchange, excitation and de-excitation of neutrals. As shown in figure 4.3, the collisional radiative model needs to be provided with information on the initial flux of neutrals, the kinetic plasma profiles, the markers velocity vector and with the time interval, dt, a marker remains in a given cell. The solution of the collisional radiative model yields the flux of neutrals that enters into the next cell. Furthermore, it yields, combined with the cell's volume, a density of neutrals per marker, d_{n}. This density is binned into a cell and state (n=1-6) dependent array and after simulating all Monte Carlo markers, 3D density profiles of neutrals are obtained.

The spectral contribution per marker is calculated if a cell along a marker's path is intersected by a LOS of the diagnostic. The Doppler shift under which the D-alpha radiation of a given marker is observed is determined by accounting for the markers velocity vector, $\vec{v_{\mathrm{n}}}$ in [cm/s], and for the unit vector pointing along the LOS's viewing direction, $\vec{v_{\mathrm{p}}}$:

$$\lambda_{\mathrm{D}} = \lambda_0 \cdot (1 + \vec{v_n} \cdot \vec{v_p})/c \tag{4.3}$$

Here, c is the speed of light in [cm/s] and λ_0 is the unshifted D-alpha wavelength (656.1 nm). The Stark splitting $\triangle\lambda_{\mathrm{S}}$ in [nm] that is observed in addition to the Doppler Effect, is determined by the following equation:

$$\triangle\lambda_{\mathrm{S}}(i) = |\vec{v_{\mathrm{n}}} \times \vec{B}| \cdot S_\lambda(i) \cdot 10^{-17} \cdot \lambda_0^2 \tag{4.4}$$

[2]The neutralized fast-ions, i.e. fast-neutrals, are also called FIDA neutrals.

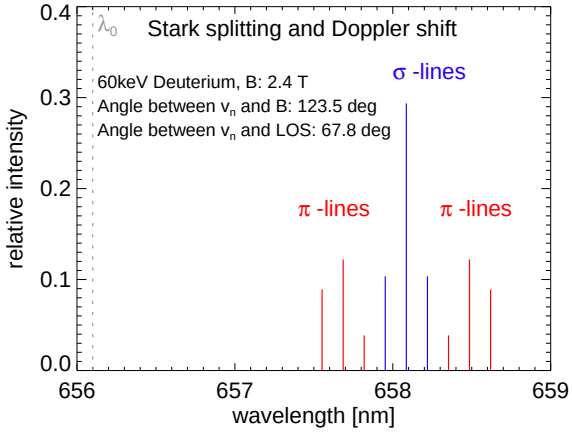

Figure 4.4: Theoretical Stark splitting into the π and σ lines of a 60 keV neutral that moves in a 2.44 T magnetic field.

where $\vec{B}$ is the cell dependent magnetic field vector in [T] and $S_\lambda(i)$ is an array that accounts for the 9 relevant transitions between the atomic state n=3 and n=2 [56]:

$$S_\lambda(1-9) = [-257.56, -193.17, -128.78, -64.39, 0, 64.39, 128.78, 193.17, 257.56] \tag{4.5}$$

As an example, figure 4.4 shows the spectrum that would be observed from a 60 keV Deuterium neutral that propagates with an angle of 67.8 deg to the direction of the observation line and with an angle of 123.5 deg to a 2.4T magnetic field. As can be seen, the emission is shifted by the Doppler effect and is split into π and σ components by the Stark effect.

Having determined the wavelengths at which the radiation of a given maker is observed, the code proceeds with the calculation of the spectral intensity per marker for each Stark component. The code takes the density in the n=3 state, $d_{\text{marker}}(3)$ in [cm^{-3}/marker], the Einstein coefficient, $E_{3\to2}$ in [Ph/s], the intersection length between the cell and the line of sight, dl in [cm], and the relative intensity of the different Stark components, $I_{\text{rel}}(i_s)$, into account:

$$I(i_s) = \frac{d_{\text{marker}}(3) \cdot E_{3\to2} \cdot dl \cdot I_{\text{rel}}(i_s)}{d\lambda} \frac{10^4}{4\pi} \tag{4.6}$$

here, i_s denotes the individual Stark lines and $d\lambda$ in [nm] is the resolution in wavelength of the output spectra[3]. The spectral intensity, $I(i_s)$ is obtained in [ph/(s nm m^2 sr marker)] as the factor $10^4/4\pi$ converts [ph/cm^2] to [ph/(m^{2}sr)]. The relative intensity of the Stark components $I_{\text{rel}}(i_s)$ is determined as follows:

$$\pi: \; I_{\text{rel}}(1:3) = S_{\text{I}}(1:3) * (1 - \cos(\vec{v_{\text{p}}}, \vec{v_{\text{n}}} \times \vec{B})^2) \tag{4.7}$$

$$\sigma: \; I_{\text{rel}}(4:6) = S_{\text{I}}(4:6) * (1 + \cos(\vec{v_{\text{p}}}, \vec{v_{\text{n}}} \times \vec{B})^2) \cdot F \tag{4.8}$$

$$\pi: \; I_{\text{rel}}(7:9) = S_{\text{I}}(7:9) * (1 - \cos(\vec{v_{\text{p}}}, \vec{v_{\text{n}}} \times \vec{B})^2) \tag{4.9}$$

$$I_{\text{rel}}(i) = \frac{I_{\text{rel}}(i)}{\sum_i I_{\text{rel}}(i)} \tag{4.10}$$

where, F is a diagnostic dependent ratio of the π and σ lines. If e.g. mirrors are used in the optics, the π and σ components are reflected with different efficiencies compared to each other. For the toroidal LOS of the FIDA diagnostic at AUG, F has been measured to be 0.5

[3]Typically wavelength arrays with a resolution of 0.01nm are used in F90FIDASIM.

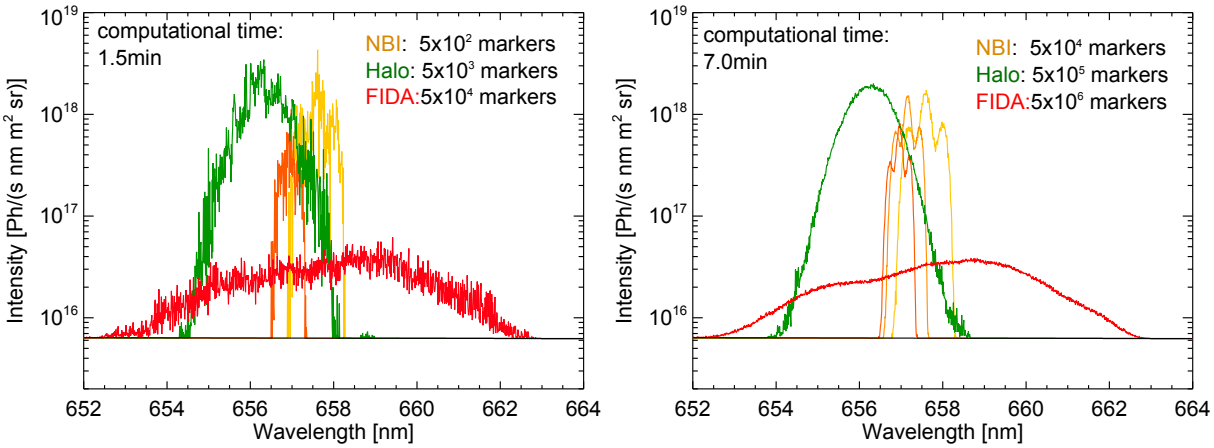

Figure 4.5: Simulated spectra on a semi-logarithmic plot consisting of the radiation of beam, halo, FIDA neutrals and of Bremsstrahlung. The left spectrum has been calculated by using a reduced number of Monte Carlo markers. The right spectrum corresponds to the typical setting used in F90FIDASIM. The radiation from beam neutrals is indicated with three different colors ranging from yellow to orange that correspond to the full, half and one third injection energy.

as a beryllium mirror was used in the optical setup. $S_{\mathrm{I}}(i)$ are the relative Stark intensities that have first been calculated in [56]:

$$S_{\mathrm{I}}(i) = [1681, 2304, 729, 1936, 5490, 1936, 729, 2304, 1681] \tag{4.11}$$

F90FIDASIM calculates the spectral contribution of every Monte Carlo marker and then bins it into a LOS and wavelength dependent array. Hence, after simulating all markers, absolute spectra are obtained. The noise in the theoretical data depends on the quantity of Monte Carlo markers that are simulated. Typically, 5×10^4 markers are simulated to describe the beam neutrals, 5×10^5 are used for the halo contribution and 5×10^6 markers are modeled to determine the FIDA spectra. This is a good compromise between the noise in the synthetic data and the computational time ($\sim$ 7 min in total on 15 CPUs). Different numbers of Monte Carlo markers are needed to simulate the beam, halo and FIDA neutrals as the regions of the populated phase space have different sizes. The phase space of beam neutrals is for example small compared to the phase space of halo neutrals. Beam neutrals are, in contrast to halo neutrals, localized along NBI and are injected into a given direction. As an example to illustrate the dependence of the noise in the spectra on the quantity of Monte Carlo markers, figure 4.5 shows two synthetic spectra of beam, halo and FIDA neutrals for which different numbers of Monte Carlo Markers were used. The shape of the two spectra is similar. However, the noise levels differ significantly.

4.1.3 Simulation of beam neutrals

F90FIDASIM models the beam neutrals present along the path of the NBI source that is used as a diagnostic beam for FIDA measurements because parts of the halo and FIDA neutrals originate from charge exchange reactions with these neutrals. It should be noted that F90FIDASIM does not determine the density of fast-ions that results from the ionization of beam neutrals. The fast-ion distribution functions, used to predict FIDA spectra, are taken from TRANSP simulations.

In F90FIDASIM, the beam neutrals are modeled by starting Monte Carlo markers at random positions on the NBI ion-source that is situated outside the simulation grid. The

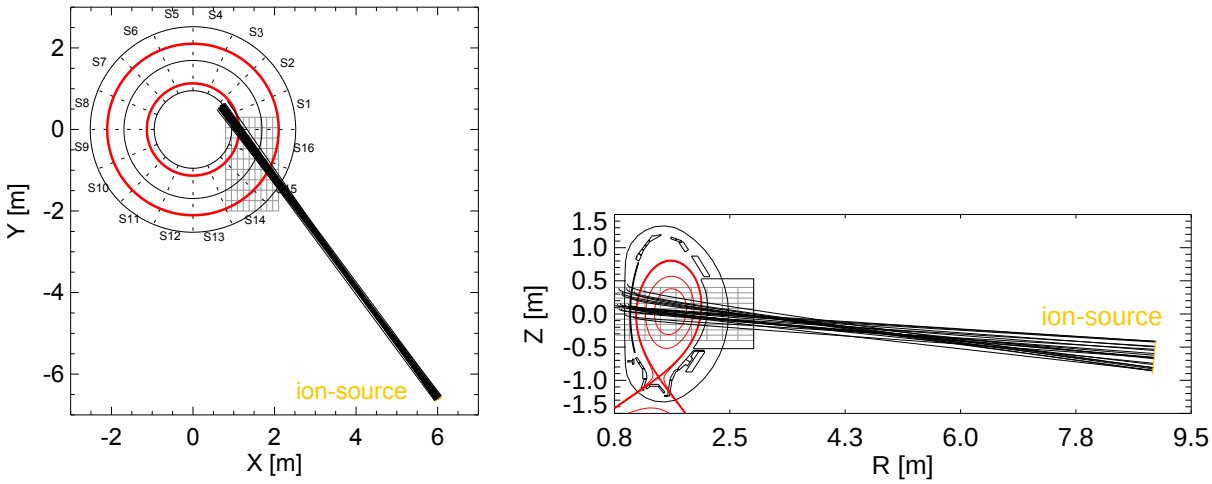

Figure 4.6: Radial and top-down view on the AUG tokamak showing the NBI-ion source used that is used as a diagnostic beam for FIDA measurements at ASDEX Upgrade. In black, the paths of markers are shown, that are launched at the NBI ion-source which is situated outside the simulation grid. Only inside the simulation grid, the attenuation excitation and photon emission of the markers is calculated.

ion-source, as indicated in figure 4.6, is defined by its position, width and height. The velocity vectors of the markers are computed from the ion-sources orientation, focus, and injection energy consisting of full, half and one third energetic neutrals. Furthermore, the injection-energy dependent divergence of NBI is taken into account by adding an additional, normally distributed angle to the velocity vectors. In figure 4.6, the markers trajectories are indicated with black lines. The initial flux of neutrals per marker, f_n in [1/(s marker)], is defined by the NBI injection energy, E_{inj} in [J], the NBI power, P_{inj} in [W], and the NBI species mix, sp_i, in terms of particles. Furthermore, it depends on the user defined total number of markers, N_{markers}, that should be simulated (e.g. 10^4):

$$f_{n=1} = \frac{P_{\mathrm{inj}}}{E_{\mathrm{inj}} \cdot (sp_1 + \frac{1}{2}sp_2 + \frac{1}{3}sp_3)} / N_{\mathrm{markers}} \tag{4.12}$$

Before entering the simulation grid, the markers are set to be in the ground state (n=1) only. Then, inside the simulation grid, the basic approach is applied which is described in detail in section 4.1.2 and which models the attenuation, excitation and photon emission of the beam neutrals. The resulting densities and spectra per marker are binned into arrays whereby finally absolute spectra and density profiles are obtained. As an example, figure 4.5 shows simulated spectra of beam neutrals for a toroidal LOS of the AUG FIDA diagnostic. The contributions from the three energy components are indicated with different colors ranging from yellow to orange. The spectral shape of the individual energy components is caused by the Stark splitting into the π and σ lines. Figure 4.7 shows a radial and a top-down view on the simulation grid. The projection of the simulated density of the beam neutrals is given on a logarithmic scale. As can be seen, the beam neutrals are attenuated when entering the plasma because of charge exchange reactions and electron/ion impact ionization.

4.1.4 Simulation of HALO neutrals

Halo neutrals are neutralized main plasma ions (bulk D-ions) that result from charge exchange reactions with beam neutrals and with other halo neutrals. They build a cloud of thermal particles along the NBI lines and are therefore called halo particles.

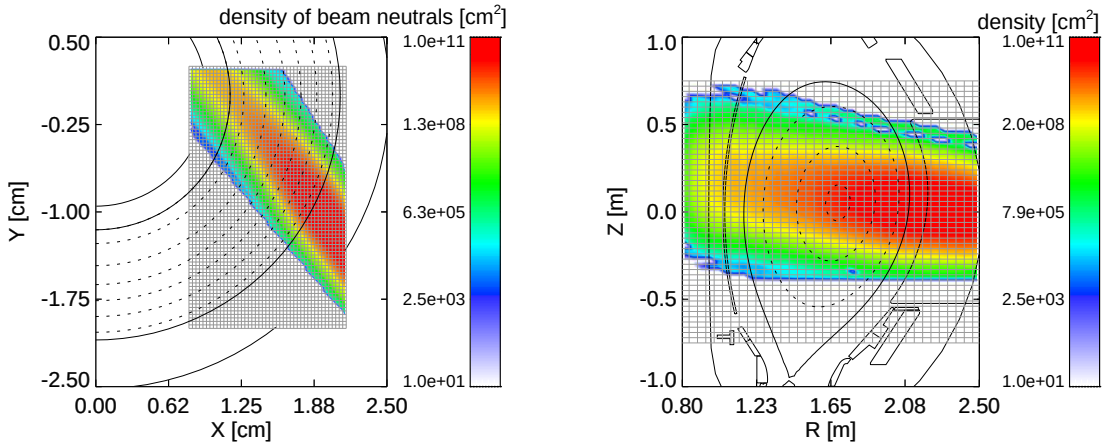

Figure 4.7: Top-down and poloidal view on the F90FIDASIM simulation grid. The projection of the density of beam neutrals is shown on a logarithmic scale. As can be seen, the beam neutrals are attenuated when entering the plasma due to charge exchange reactions and impact ionization with ions and electrons.

The simulation of the halo contribution is very important for the FIDA measurements because halo neutrals contribute significantly to the charge exchange probability of fast-ions. It needs to be simulated in several steps because, as already mentioned, halo neutrals can, not only be generated by charge exchange reactions between main ions and beam neutrals, but also by charge exchange reactions between main ions and other halo neutrals. By charge exchange reactions with other halo neutrals, the absolute density of the halo population is unchanged because a new halo neutral is born at the expense of an existing one. However the velocity vectors and the distribution of the excited states of halo neutrals can change. A new model has been implemented in F90FIDASIM that no longer treats the charge-exchange reactions solely as a random walk. The halo neutrals are simulated iteratively in different generations which enables the application of the basic approach discussed in section 4.1.2.

The first generation of halo neutrals is also called direct charge exchange (DCX) component and originates from charge exchange reactions between the beam neutrals and the main ions. It is modeled by simulating Monte Carlo markers that are started at random positions in every cell of the simulation grid. The quantity of markers, $N_{\mathrm{markers}}(i)$, that are simulated in a given cell, i, is defined by the normalized product of the density of beam neutrals and main D-ions present in this cell:

$$N_{\mathrm{markers}}(i) = N_{\mathrm{markers}} \frac{d_{\mathrm{beam}}(i) \cdot d_{\mathrm{main}}(i)}{\sum_j (d_{\mathrm{beam}}(j) \cdot d_{\mathrm{main}}(j))} \tag{4.13}$$

Here, the sum over j corresponds to all grid-cells. N_{markers} is the total number of markers to be simulated and $d_{\mathrm{beam}}(i)$ is the density of beam neutrals per cell. $d_{\mathrm{main}}(i)$ is the density of main ions which is defined as the cell-related D-ion density minus the fast-ion density. For every marker, a velocity vector, $\vec{v_n}$, can be defined by using normally distributed random numbers that represent the cell-related plasma rotation and ion temperature:

$$v_x = randn \cdot \sqrt{T_i \; e_0/m} + rot_x \tag{4.14}$$

$$v_y = randn \cdot \sqrt{T_i \; e_0/m} + rot_y \tag{4.15}$$

$$v_z = randn \cdot \sqrt{T_i \; e_0/m} \tag{4.16}$$

Here, $randn$ denotes normally distributed random numbers with a standard deviation of one. T_i is the cell-related ion temperature in [eV], m the halo particles mass in [kg], e_0 is the unit charge in [C] and $rot_{x,y}$ the cell-related toroidal plasma rotation in [m/s]. In total,

the random velocity vectors thereby represent a Maxwell distribution that is shifted by the plasma rotation.

Then, the initial flux of halo neutrals, f_n in [1/(s marker)], in the various atomic states n is defined by:

$$f_n = \frac{n_{\text{rate}}(n) \cdot d_{\text{main}} \cdot V_{\text{cell}}}{N_{\text{markers}}} \tag{4.17}$$

where V_{cell} is the cell's volume in [cm^3] and $n_{\text{rate}}(n)$ are the neutralization rates in [1/s], i.e. the probabilities for charge reactions with beam neutrals. The neutralization rates are discussed more in detail in section 4.1.9. They depend on the charge exchange cross-sections, on the relative velocity between the markers and the beam neutrals and on the density of beam neutrals. With the initial flux of neutrals per marker, the basic approach (see section 4.1.2) can be applied. The latter models the attenuation of the first generation of halo markers by impact ionization and charge exchange reactions and yields spectra and 3D density profiles.

The second generation of halo neutrals originates from charge exchange reactions between main ions and the first generation of halo neutrals. Comparable to the simulation of the first-generation, Monte Carlo markers are started with various start positions in the cells and with a velocity distribution that depends on the ion-temperature and the plasma rotation. The quantity of Monte Carlo markers simulated per cell is determined similarly to equation 4.13 using the normalized product of the density of main-ions and the density of the first generation of halo neutrals. Again, the initial flux of neutrals per marker is calculated by accounting for the density of main ions, for the neutralization rate, for the cell's volume and for the number of markers. However, the neutralization rate now depends on the density of the first generation of halo neutrals and not on the density of beam neutrals. After applying the basic approach that simulates the markers excitation and attenuation along the paths through the grid, the densities and the spectra of the second generation are obtained.

The third and the following generations are calculated similarly to the second generation whereas the neutralization rates depend on the density of the previous generation. From generation to generation, the flux of halo neutrals decreases compared to the previous generation because more and more neutrals are lost through electron-, ion- and impurity-impact ionization which is accounted for by the basic approach, i.e. by the collisional radiative model. As the change of the density of halo neutrals of a given (the i-th) generation depends on the density of the previous generation $(i-1)$, the evolution of the halo population can be described by an exponential function:

$$n_H(i) = n_H(1) \cdot \exp\left(-\frac{i}{\tau}\right) \tag{4.18}$$

where τ is the number of iterations after which the halo density is decreased to 1/e. After typically 10 iterations, the simulation can be stopped because the fluxes of halo neutrals get negligible and as an exponential decay converges.

Absolute halo spectra and densities are finally obtained by summing up the contributions of the different generations. An example of simulated halo spectra are shown in figure 4.5. The noise in the spectra corresponds to the limited numbers of Monte-Carlo markers that were used (5×10^5 and 5×10^3 markers). Figure 4.8 shows the projection of the simulated halo density on a radial view and on a top-down view. As can be seen on the semi-logarithmic scale, the population of halo neutrals is broader compared to the population of beam neutrals because halo neutrals can propagate perpendicular to the NBI lines. However, the difference in width between the distribution of beam neutrals and halo neutrals is typically not larger

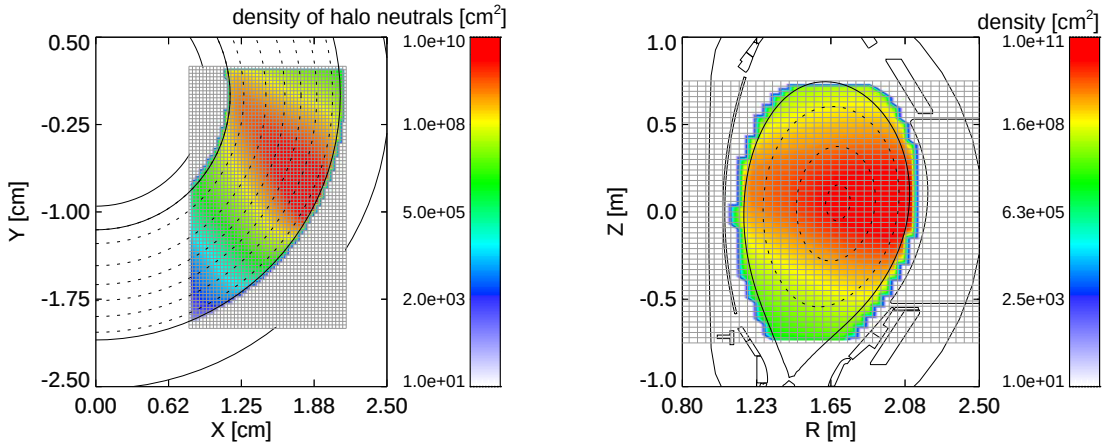

Figure 4.8: Top-down and poloidal view on the AUG tokamak and the F90FIDASIM simulation grid. The projected density of the halo neutrals is shown on a logarithmic scale.

than 20% as the mean free path of halo neutrals is only a few cm. It should be noted that the halo density is generally larger than the density of beam neutrals: In contrast to the beam neutrals, the density of halo neutrals is not reduced by charge-exchange reactions with main ions. Furthermore, the cross-sections for ion-impact ionization of the n=1 state (see chapter 8.4) are smaller for low collision energies and are consequently smaller for the thermal halo particles than for the neutralized fast-ions.

4.1.5 Simulation of FIDA spectra with the Monte Carlo approach

With the knowledge of the density of beam and halo neutrals, the simulation of the FIDA component can be performed. In every cell of the simulation grid, Monte Carlo markers are started at random positions. The number of markers that is started in a given cell is defined similarly to equation 4.13. It depends on the user-defined total number of FIDA-markers and on the normalized product of the cell-related density of fast-ions and beam neutrals plus halo neutrals. The energy and the pitch of the markers are determined from the input theoretical fast-ion distribution function by using rejection sampling [57]. The latter enables to define random energies and pitches that are weighted by the fast-ion velocity distribution. The third dimension of the velocity space, the gyro angle of fast-ions, is defined by uniformly distributed random phases in 360°. The velocity vectors in terms of pitch, energy and gyro angle are then converted into Cartesian vectors, v_n, and the initial positions of the markers, $\vec{x}_{\mathrm{start}}$, are corrected by the gyro-motion of the fast-ions because TRANSP uses a guiding center approach to calculate the fast-ion distribution functions:

$$\vec{x}_{\mathrm{start}} = \vec{x}_{\mathrm{start}} - (\vec{v}_{\mathrm{n}} \times \vec{B}) \, \frac{m}{|\vec{B}|^2 \cdot e} \cdot 10^{-2} \tag{4.19}$$

Here, $\vec{B}$ is the magnetic field vector, m is the fast-ion mass and e is the elementary charge. For every Monte Carlo marker, the neutralization rates, $n_{\mathrm{rate}}(n)$ in [1/s], are calculated according to section 4.1.9 which enable to determine the initial flux of FIDA neutrals, f_n in [1/(s marker)]:

$$f_n = \frac{n_{\mathrm{rate}}(n) \cdot d_{\mathrm{fast-ion}} \cdot V_{\mathrm{cell}}}{N_{\mathrm{markers}}} \tag{4.20}$$

where $d_{\mathrm{fast-ion}}$ is the fast-ion density that corresponds to all pitches and energies of fast-ions and V_{cell} is the cell's volume. With the initial flux, the basic approach described in sections

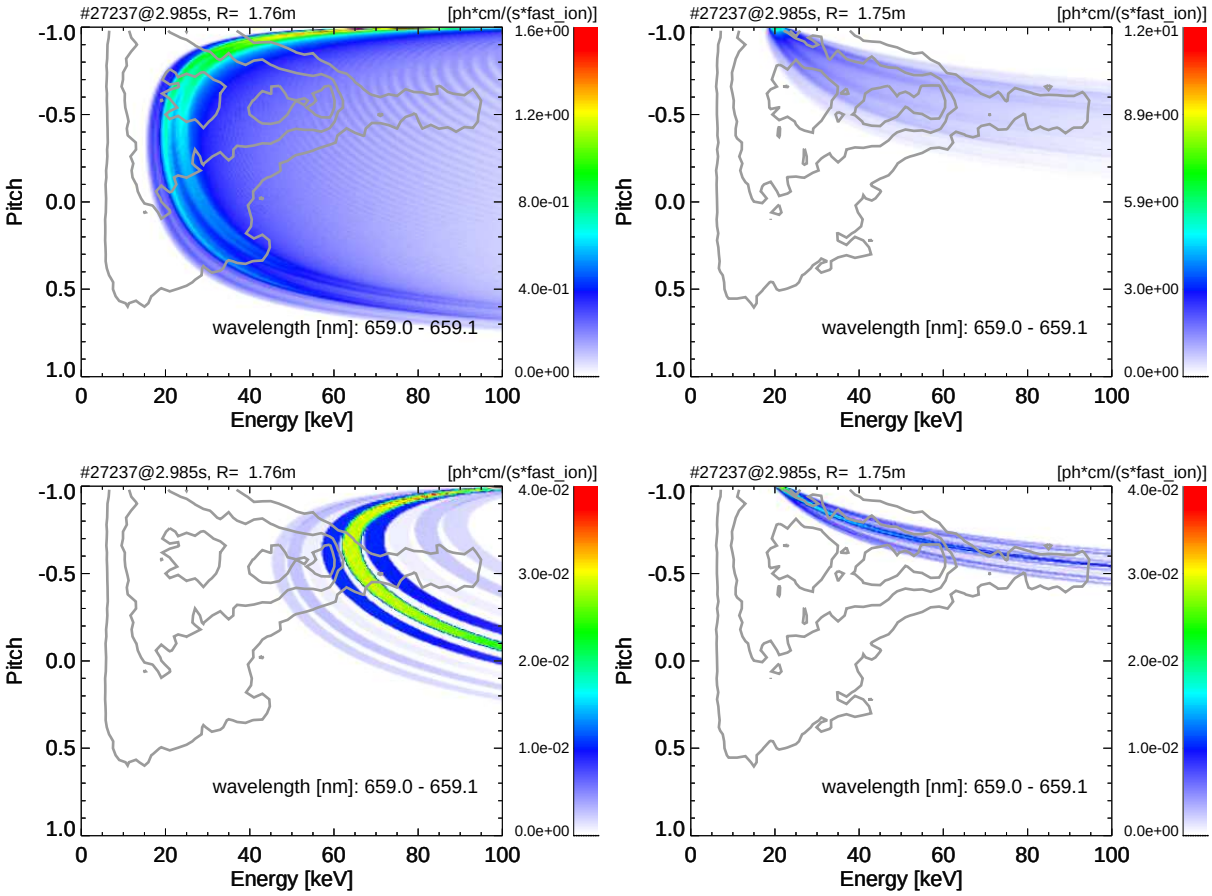

Figure 4.9: Weight functions of a poloidal LOS (left) and a toroidal LOS (right) for wavelengths between 659.0 nm and 659.1 nm. In the top row, the full weight functions are displayed. In the bottom row, the weight functions have been calculated for only one gyro angle. Superimposed to the weight functions, a theoretical fast-ion velocity space distribution is shown that has been predicted by TRANSP (gray contour lines). By folding the fast-ion distribution functions with the weight functions, the FIDA radiance is obtained for the defined wavelength range.

4.1.2 is applied which yields the spectra of neutralized fast-ions. As an example, figure 4.5 shows predicted FIDA spectra that were calculated by using 5×10^4 and 5×10^6 Monte Carlo markers.

4.1.6 Simulation of FIDA spectra using weight functions

A second method has been developed to simulate FIDA spectra that is incorporated into F90FIDASIM and that makes use of the same algorithms and cross-sections as the standard Monte-Carlo approach. However, instead of performing a Monte Carlo simulation of fast-ions according to the basic approach discussed in 4.1.2, weight functions are calculated and then folded with a given theoretical fast-ion distribution function.

4.1.6.1 Description of weight functions

The weight functions display the part of the velocity space that can be accessed by a given LOS in a defined wavelength range. That is to say, the weight functions show the probability for a fast-ion of a certain energy and pitch range to be neutralized and to subsequently emit D-alpha radiation into a given wavelength range. The shape of the weight functions in

the velocity space mainly depends on the geometry of the LOS and on the magnetic field configuration. As an example, figure 4.9 shows weight functions of a toroidal LOS (right) and a poloidal LOS (left) of the AUG FIDA diagnostic which is described in detail in chapter 5. As can be seen, the weight functions are not single points in the 2D velocity space but cover a wide range. This can be explained as fast-ions with different energies, pitches and gyro angles can emit radiation at the same wavelength. The weight functions in the upper row of figure 4.9 are calculated for all gyro angles of fast-ions (400 simulated gyro angles) while the lower row shows, for illustrative purposes, the weight functions for only one gyro angle. As can be seen, the different gyro angles cover different parts of the fast-ion velocity space. The difference between the weight function for all gyro angle to the weight function for only one gyro angle is most obvious for the poloidal geometry. A poloidal view is arranged perpendicularly to the magnetic field lines and observes large Doppler shifts from the gyro motion of fast-ions depending on the gyro angle. In contrast, the toroidal views are arranged along the magnetic field lines, observe large Doppler shifts from passing fast-ions and consequently do not strongly depend on the gyro motion and gyro angle.

In addition to the dependence of the weight functions on the gyro angle, the Stark effect considerably broadens the weight functions in the velocity space: Every single Stark line that is observed at a given wavelength refers to a different region in the velocity space. The 9 regions visible in the poloidal weight function for only one gyro angle consequently refer to the 9 Stark lines shown in figure 4.4. Moreover, the weight functions depend on the width of the wavelength range for which they are defined. As an example, the width of the individual Stark regions in the lower left plot of figure 4.9 corresponds to a wavelength range of 0.1 nm. By increasing this wavelength range, this region in the velocity space would increase. Finally it should be noted that the weight functions for all gyro angles are maximal close to their edges. This can be explained as the Doppler effect depends on the cosine function between a given velocity vector and the viewing direction which mostly weights its turning points.

4.1.6.2 Calculation of weight functions

The weight functions depend not only on the geometry of the LOS but also on the kinetic plasma profiles, on the magnetic field vectors and on the density of neutrals present along the path of NBI. They thus need to be calculated separately for each discharge and time point. In general, the weight functions are calculated by performing a loop over the whole fast-ion velocity space. For every velocity vector, the probability for charge exchange is calculated and the amount of photons that would be emitted into a defined wavelength is determined.

The calculation of weight functions is based on the assumption that the FIDA radiation is well localized. That is to say, the FIDA radiation is assumed to originate from the position where the beam and halo density is present which allows the application of line averaged plasma parameters (weighted means), k_{mean}, present along a given LOS:

$$k_{mean} = \frac{\int k \cdot (d_{beam} + d_{halo})\ dl}{\int (d_{beam} + d_{halo})\ dl} \tag{4.21}$$

Here dl is the path along the LOS. k denotes local plasma parameters such as the electron and ion temperatures, the density, the magnetic field vectors, the plasma rotation or the impurity density. d_{beam} and d_{halo} are the density of beam and halo neutrals. In addition to the line averaged data, the line-integrated densities of beam and halo neutrals are determined before starting the main calculation of the weight functions.

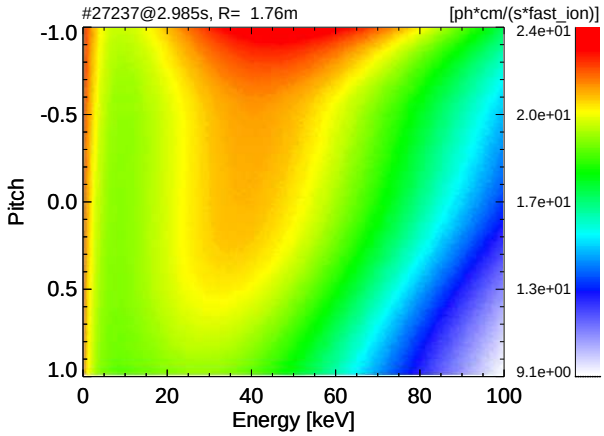

Figure 4.10: Probability of fast-ions to emit D-alpha radiation calculated for discharge # 27237 at 2.985sec. The probability depends on the distribution function of beam and halo neutrals and on the kinetic plasma profiles.

With the knowledge of the line averaged and line-integrated quantities, the code models a given LOS fast-ions with typically 200 different energies, 200 pitches and 200 gyro angles to cover the entire fast-ion velocity space. For every fast-ion, first, the neutralization rate is calculated (see section 4.1.9). That is to say, the probability rate is determined that a fast-ion, which propagates through the density of beam and halo neutrals, undergoes a charge exchange reaction. To calculate the neutralization rate, the LOS integrated density of beam and halo neutrals is used instead of a cell-related density as done in the basic approach (see section 4.1.2). Then, the time, dt, a fast-ion needs to pass through the density of beam and halo neutrals is calculated. For this purpose, F90FIDASIM accounts for the velocity of a given fast-ion and for its intersection length with the density of beam and halo neutrals at half maximum.

For a single fast-ion, the neutralization rate is equal to the initial flux of neutrals per fast-ion after the charge exchange event. This initial flux of neutrals is applied in the collisional radiative model in order to obtain the quantity of fast-neutrals present along the LOS during the time interval dt. Here, the line averaged kinetic plasma parameters are applied in the collisional radiative.

With the quantity of fast-neutrals in the n=3 state, $d_{fn(3)}$, the line-integrated flux of photons emitted by a single fast-ion in [ph cm/s] can be calculated:

$$I = d_{fn(3)} \cdot E_{3\to 2} \tag{4.22}$$

where $E_{3\to 2}$ is the Einstein coefficient for the transition from n=3 to n=2. As an example, figure 4.10 shows the calculated photon flux of fast-ions as a function of pitch and energy. The photon flux depends on the pitch of the fast-ions because of the distinct velocity vectors of the beam neutrals that yield, due to different relative collision velocities, different probabilities for charge exchange.

The code proceeds with the calculation of the Doppler shift and the Stark splitting according to equations 4.3 and 4.4 whereby the averaged magnetic field vectors are applied. It then checks if the calculated wavelengths are inside the predefined wavelength range for which the weight function is calculated. If a given Stark line exists within this wavelength range, the relative intensity of the stark line is calculated according to equation 4.7, multiplied by the flux of photons per fast-ion and binned on an energy and pitch dependent array. After simulating all fast-ions, every pitch and energy bin is divided by the number of gyro angles

that have been calculated. Thereby, 2D weight functions in terms of [ph cm/(s fast-ion)] are finally obtained.

4.1.6.3 Determination of FIDA spectra and discussion

Superimposed to the weight functions, figure 4.9 shows a LOS-averaged velocity space distribution of fast-ions predicted by TRANSP in gray contour lines. The velocity space distribution has been LOS averaged by taking the beam and halo density as weight. The FIDA radiance, I_{FIDA} in [ph/(s nm m^2 sr)], can be calculated by folding the averaged fast-ion distribution function, $FBM(E,P)$ in [fast-ions/(cm^3 dP dE)], with a given weight function, $WF(E,P)$ in [ph cm/(s fast-ions)]:

$$I_{\mathrm{FIDA}} = \frac{10^4}{4\pi\ d\lambda} \int_{P=-1}^{1} \int_{E=0}^{E_{\max}} FBM(E,P) \cdot WF(E,P) \cdot dP \cdot dE \tag{4.23}$$

Here, $d\lambda$ is the wavelength range defined by the weight function, dE is the energy interval and dP is the pitch interval. The factor $\frac{10^4}{4\pi}$ arises from the conversion from [ph/cm^2] to [ph/(m^{2}sr)]. By folding the fast-ion distribution function with multiple weight functions that are defined for different wavelength ranges, artificial spectra are obtained. As an example, figure 4.11 compares theoretical FIDA spectra obtained from 140 weight functions (140 wavelengths between 649nm and 663nm) to spectra from the standard Monte Carlo approach for a toroidal and a poloidal LOS. Clearly, similar results are obtained with the two methods. The time needed to calculate the weight functions is comparable to the time, the standard method needs to calculate FIDA spectra. However, the subsequent convolution of the weight functions with a fast-ion distribution function is very fast (about 10 seconds per LOS). Therefore, the weight function technique is very useful when, for example, analyzing synthetic FIDA spectra for various fast-ion distribution functions. Furthermore, the weight function method has the advantage compared to the standard Monte Carlo method that it provides synthetic spectra without Monte Carlo noise. However, the weight function method cannot completely replace the Monte Carlo simulation because it uses line averaged (along the LOS) fast-ion distribution functions, magnetic fields and kinetic plasma parameters, as well as line-integrated densities of beam and halo neutrals. Thereby, changes of these parameters perpendicular to the LOS are not taken into account. As a result, the spectra determined by the weight function method typically deviate from the Monte Carlo approach at low wavelength shifts which correspond to fast-ions that propagate perpendicular to the LOS. However, the differences are small because of the good localization of the FIDA radiation due to the overpopulation of the n=3 state after the charge exchange process (see section 4.1.9).

Finally it should be noted that conversion factors from the measured FIDA radiances to fast-ion densities can be calculated by folding a given weight function with a normalized fast-ion velocity space distribution. Thereby, the assumption must be made that the shape of the normalized distribution is present in the investigated conditions and that is does not change. As will be discussed in chapter 7, the conversion factors calculated with the weight function method have been used to study the temporal evolution of the fast-ion density in the presence of sawtooth crashes. Moreover, the weight functions can even be applied to de-convolute the FIDA measurement if, as described in [58], measurements from multiple LOS with different angles to the magnetic field lines were available.

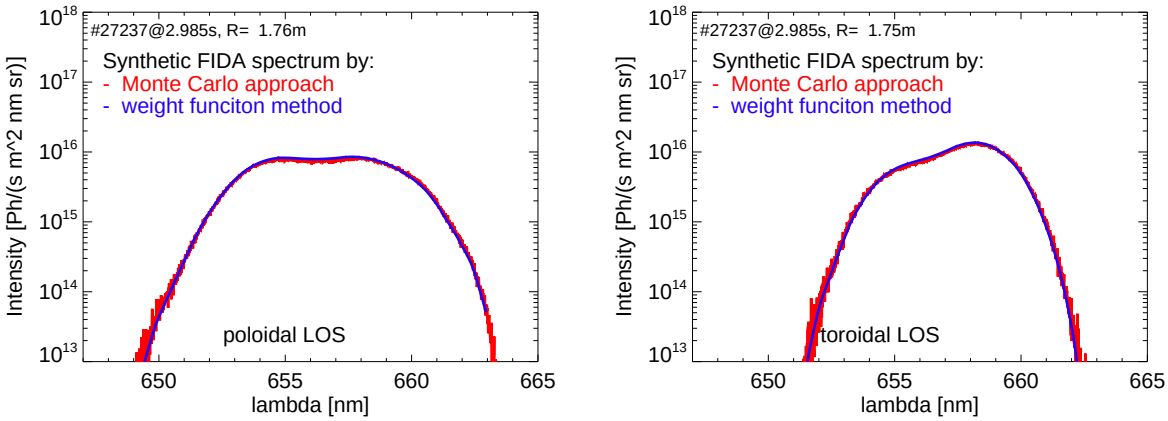

Figure 4.11: Simulated spectra using the Monte Carlo approach (red) and using the weight function method (blue) for a toroidal LOS (right) and a poloidal LOS (left).

4.1.7 Determination of the radiation from Bremsstrahlung

In order to be able to validate the simulated spectra against the measured spectra, the code has been extended to also simulate the radiation from Bremsstrahlung. The simulation of Bremsstrahlung is possible by using the $3D$ simulation grid and the kinetic profiles that are input to F90FIDASIM. In every cell along a given LOS, the local radiation from Bremsstrahlung is determined by:

$$Il_{\text{brems}}(\lambda) = 7.57x10^{-8} \frac{g d_{\text{el}}^2 Z_{\text{eff}}}{\lambda \sqrt{T_{\text{e}} 10^3}} \exp \frac{-hc}{\lambda T_{\text{e}}} \tag{4.24}$$

Here, Il_{brems} denotes the local emissivity of Bremsstrahlung in [ph/(s nm m^3 sr)], d_{el} is the local electron density in [cm^3], Z_{eff} is effective charge, h is the Planck constant in [eV/s], T_{e} is the electron temperature in [eV], c is the speed of light in [m/s] and λ is the wavelength for which the Bremsstrahlung is calculated. Finally, g is the gaunt factor which is, according to [59], approximated by:

$$g = 5.542 - (3.108 - \ln T_{\text{e}})(0.6905 - 0.1323/Z_{\text{eff}}) \tag{4.25}$$

By summing up the local emissivities of the cells along the LOS, multiplied by the intersection length between the LOS and the cells, dl in [cm], the spectra of Bremsstrahlung $I_{\text{brems}}(\lambda)$ are obtained:

$$I_{\text{brems}}(\lambda) = \sum_k Il_{\text{brems}}\ dl_k \tag{4.26}$$

Here, k denotes the various cells along a given LOS. As an example, the radiation from Bremsstrahlung has been included in black in figure 4.5 which has been shown earlier. As can be seen, it has a flat shape in the observed wavelength range and can therefore be described by a horizontal line.

4.1.8 Collisional radiative model

The collisional radiative model is one of the most important parts of F90FIDASIM because it describes the time-dependent attenuation, population and depopulation of the atomic states, n, of beam, halo and FIDA neutrals. The model is applied in the basic Monte Carlo

approach of F90FIDASIM as well as when calculating the weight functions. It is based on the solution of the following differential equation:

$$\begin{pmatrix} df_1/dt \\ df_2/dt \\ \vdots \\ df_6/dt \end{pmatrix} = \begin{pmatrix} a_{11} & a_{12} & \dots & a_{16} \\ a_{21} & a_{22} & \dots & a_{26} \\ \vdots & \vdots & \ddots & \vdots \\ a_{61} & a_{62} & \dots & a_{66} \end{pmatrix} \begin{pmatrix} f_1 \\ f_2 \\ \vdots \\ f_6 \end{pmatrix} \tag{4.27}$$

Here, f_n in $[1/(s\ marker)]$, is the flux of neutrals per marker in the state, n, and df_n/dt is its time derivative. The matrix A consists of rates, a_{nm} in $[1/s]$, that correspond to the different mechanisms that attenuate, excite and de-excite neutrals. When applying the collisional radiative model in F90FIDASIM, first, the different matrix elements are determined. The off-diagonal elements a_{nm} are defined positive and account for the populating transitions from an initial state n to a final state m. They can be expressed by the sum of k individual rates, $c_{nm}(k)$ in $[1/s]$, for electron-, ion-, impurity-impact excitation and de-excitation and for spontaneous de-excitation (the Einstein coefficients [60]):

$$a_{nm} = \sum_k c_{nm}(k) \tag{4.28}$$

The diagonal elements are defined negative and correspond to the depopulating transitions. They depend on the sum of the k individual excitation and de-excitation processes into all final states m. Furthermore, they consist of the j different loss-mechanisms l_n:

$$a_{nn} = -\sum_k \sum_{m=1}^{12} c_{nm}(k) - \sum_j l_n(j) \tag{4.29}$$

The loss-mechanisms, l_n, are electron-, ion- and impurity-impact-ionization and charge exchange with ions and impurities. It should be noted that in F90FIDASIM, the atomic states are modeled up-to n=6. Nevertheless, the sum in equation 4.29 goes to m=12 as the impact excitation by ions, impurities and electrons into excited states above m=6 acts as a loss mechanism that needs to be taken into account [61]. The neutrals that are excited into high states are immediately lost because of high cross-sections for impact ionization and charge exchange of these states. The rates c_{nm} and l_n can be calculated by:

$$c_{nm} = \langle \sigma v \rangle_{nm} (E_\mathrm{P}, T_\mathrm{T}) \cdot d_\mathrm{T} \tag{4.30}$$

where c_{nm}, from now on, also stands for the loss mechanisms l_n (for the l_n, m would be infinite). $\langle \sigma v \rangle_{nm} (E_\mathrm{P}, T_\mathrm{T})$ is the energy and temperature-dependent effective rate-coefficient in $[cm^3/s]$. E_P is the energy of the projectiles (beam, halo and FIDA neutrals) in $[keV]$. T_T and d_T are the temperature and density of the target particles in $[keV]$ and $[cm^{-3}]$ which can be electrons, impurity ions and D-ions. The effective rate coefficients are determined by calculating the mean atomic rates for collisions between the projectiles and a Maxwell distribution, $M_i(T_\mathrm{t})$, of ni target particles:

$$\langle \sigma v \rangle_{nm} (E_\mathrm{P}, T_\mathrm{T}) = \frac{1}{ni} \sum_{i=1}^{ni} \sigma_{nm}(E_\mathrm{rel}(i)) \cdot v_\mathrm{rel}(i) \tag{4.31}$$

$$v_\mathrm{rel}(i) = |\vec{v}_\mathrm{P}(E_\mathrm{P}) - \vec{v}_\mathrm{T}(M_i(T_\mathrm{T}))| \tag{4.32}$$

$$E_\mathrm{rel}(i) = 0.5 \cdot m_\mathrm{u} \cdot v_\mathrm{rel}(i)^2 \tag{4.33}$$

here, m_{u} is the atomic unit mass in $[kg]$, $\sigma_{nm}(E_{rel})$ are the energy and state dependent cross-sections in $[cm^2]$, E_{rel} is the relative collision energy in $[keV/amu]$ between a target particle and a projectile and v_{rel} is the corresponding relative collision velocity in $[cm/s]$. The calculation of the effective rate coefficients is very time consuming because a large number ni of velocity vectors, $\vec{v}_{\mathrm{T}}$, needs to be applied to describe a Maxwell distribution well. Therefore, the rate-coefficients used in F90FIDASIM have been tabulated for the initial and final states between n/m=1 and n/m=12 and for a wide range of temperatures, T_{T}, and energies E_{P}. It should be noted that the fast-ion velocity distribution is not taken into account in the effective rate coefficients which is valid as long as the fast-ion density is small compared to the main-ion density (below 20%). For example, the change of the effective rate coefficient for charge exchange of 60 keV beam neutrals in the n=1 state at a temperature of 3 keV is 6% when accounting for 20% fast-ions[4]. The cross-sections, σ_{nm}, that are used to calculate the effective rate-coefficients are displayed in the appendix (chapter 8.4). They are mainly taken from reports by Janev and Smith [62], [63]. Only for ion-impact ionization by deuterium ions, up-dated cross-sections from [64] are used. Furthermore, the cross-sections for impact de-excitation by electrons, D-ions and impurity ions are calculated using the reversibility formula [65] for high projectile energies:

$$\sigma_{mn} = \sigma_{nm}\frac{m^2}{n^2} \tag{4.34}$$

With the knowledge of the elements a_{nm} of matrix A, the differential equation 4.27 can be solved. Previously, a forth order Runge Kutta method was used to solve the equation numerically. However, to eliminate numerical instabilities, F90FIDASIM now uses an analytical approach [66]:

$$F(t) = S^{-1} \cdot F(t=0) \cdot S \cdot \exp\left(\Lambda\ dt\right) \tag{4.35}$$

Here, F is the vector of the fluxes of neutrals f_n for n=1-6, S is the matrix of Eigenvectors of A and S^{-1} denotes its inverse. Λ is a diagonal matrix that contains the Eigenvalues of A. The detailed derivation of equation 4.35 is given in the appendix (chapter 8.4). As can be seen, the analytic solution yields the flux of neutrals f_n after the time dt. The density of neutrals per Monte Carlo marker d_n that is binned into the 3D density arrays, is determined by the integration of equation 4.35 and by the division with the cell's volume V_{cell}:

$$d_{\mathrm{n}} = S^{-1} \cdot N(t=0) \cdot S \cdot (\exp\left(\Lambda\ dt\right) - 1)/\Lambda \cdot \frac{1}{V_{\mathrm{cell}}} \tag{4.36}$$

The term -1 next to the exponential function is due to the integration constant that can be determined by the fact that for $dt = 0$, the integral should be zero. As an example of the solution of the collisional radiative model, figure 4.12 shows the evolution of the flux of 60 keV neutrals that are initially set to be in the $n = 1$ state only. Within the first cm's along the path, the excited states are populated and an equilibrium population is reached after about 2 cm. It can also be seen that the population of the excited states is orders of magnitudes lower than the population of the ground state (n=1).

4.1.9 Neutralization rates of fast and main ions

The neutralization rates through charge exchange reactions are needed when simulating the halo and the FIDA neutrals. By defining the initial state by n and the final state by m, the charge exchange process can be described as follows:

$$D_P^+ + D_T(n) \overset{cx}{\rightarrow} D_P(m) + D_T^+ \tag{4.37}$$

[4]When assuming a fast-ion velocity space distribution that is typically present at ASDEX Upgrade.

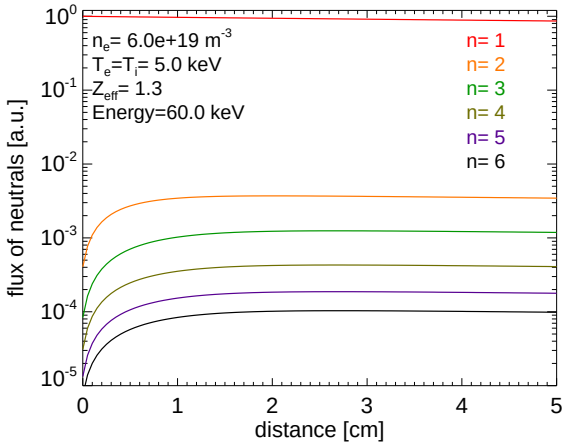

Figure 4.12: Flux of 60 keV neutrals on a semi-logarithmic scale that are initially set to be in the n=1 state only. Along the neutrals path through a plasma, the excited states are populated.

where D_P and D_T denote the Deuterium ions and neutrals. T denotes the target particles such as beam and halo neutrals and P denotes the projectiles which can be fast-ions and main-ions. The neutralization rate $n_{\mathrm{rate}}(m)$ of the projectiles can consequently be expressed by:

$$n_{\mathrm{rate}}(m) = \sum_n d_{\mathrm{T}}(n) \cdot \sigma_{nm}(E_{\mathrm{rel}}) \cdot v_{\mathrm{rel}} \tag{4.38}$$

Here, $d_{\mathrm{T}}(n)$ is the density of the target neutrals in $[1/cm^3]$ in the different atomic states, $\sigma_{nm}(E_{\mathrm{rel}})$ is the energy-dependent collision cross-section for charge exchange in $[cm^2]$ and v_{rel} is the relative collision velocity in $[cm/s]$. The neutralization rates need to be calculated separately for collisions with the full, half, third energetic beam neutrals and for the halo neutrals because the velocity vectors are different. The relative collision velocities and energies with the beam neutrals are calculated by defining the beam velocity vectors from the position of the ion-source and the start position of a given projectile marker. The neutralization rates with halo neutrals are determined by calculating the mean neutralization rate for collisions with a thermal velocity distribution of halo particles that corresponds to the cell-related ion temperature and plasma rotation at which a given projectile marker is started.

When calculating the neutralization rates according to equation 4.38, charge exchange cross-sections are used that depend on the initial state n and on the final state m. For the initial states n=1, n=2 and n=3 the cross-sections are taken from the ADAS database [67] which needed to be corrected for the states n=2 and n=3 (see chapter 8.4 for more information). For higher states, the cross-sections have been approximated. On the one hand, certain cross-sections can be estimated by the reversibility formula (see equation 4.34). It is e.g. possible to define the charge exchange cross-sections from n=4 to m=1 by taking the known cross-sections from n=1 to m=4. On the other hand, so-called bundled cross-sections, provided by [62], have been used. The bundled cross-sections, which are also used in the collisional radiative model, treat the charge exchange process only as a loss mechanism and are therefore not m-resolved. However, by assuming that the probability for a charge exchange reaction from a state n to m decreases exponentially with the energy difference between the states, m-resolved cross-sections can be approximated. Of course, the uncertainties of this approach are relatively high. However, by using the approximated cross-sections, it became clear that the charge exchange reactions with neutrals in excited states above n=3 do not significantly contribute to the FIDA and halo radiation (less than

1%). The fraction of neutrals in the excited states is low compared to the one in the ground state (see figure 4.12). Therefore, the neutralization rate from e.g. n=5 to m=3, which depend on the density of the n=5 state, are negligible. The most important cross-section for the FIDA and halo radiation is the well-known one from n=1 to n=3. It contributes to the radiation with about 50% because it overpopulates the n=3 state after charge exchange reactions. As shown in figure 4.12, the n=3 level is typically 200 times less populated than the n=1 state. However, at typical beam energies of about 30 keV/amu, the cross-section from n=1 to m=3 is only 20 times smaller than that from n=1 to m=1 (see figure B.3). Hence, after charge exchange reactions, ten times more neutrals are in the n=3 state than in the equilibrium which yields strong D-alpha radiation. This radiation is localized at the charge exchange position as the back-transition to the equilibrium is very fast and hence provides a good spatial resolution of the FIDA technique.

4.2 Validation of F90FIDASIM

F90FIDASIM needs to be validated because significant changes have been made to the code compared to the IDL version [53]. The simulation of the FIDA spectra has already been validated, as two different methods, namely the standard Monte Carlo approach and the approach using weight functions, give very similar results (see section 4.1.6). However, both approaches use the same collisional radiative model and the same predicted density of beam and halo neutrals which are not yet validated. Hence, this section presents an analysis of the collisional radiative model of F90FIDASIM and gives a comparison to the collisional radiative model provided by ADAS [67]. The beam density profiles from F90FIDASIM are compared to the ones predicted by TRANSP and the footprint of NBI, measured by a beam-imaging diagnostic, is compared to the simulated beam and halo radiation. Finally simulated beam and halo spectra are compared to measurement of a beam-emission spectroscopy (BES) diagnostic.

4.2.1 Validation of the collisional radiative model

The collisional radiative model used in F90FIDASIM models atomic states between n=1 and n=6 and accounts for the states between n=7 and n=12 by adding an additional loss mechanism, l_n, to the diagonal elements of the matrix A (see section 4.1.8). The states above n=6 do not need to be simulated as their relative population is small due to high cross-sections for charge-exchange and ionization (see chapter 8.4). However, the excited states above n=6 contribute to the de-population of e.g. the n=3 state through electron, ion and impurity-impact excitation.

As can be seen in figure 4.13, the relative population of the n=3 state of neutrals depends on the number of n-states that are simulated. The relative population strongly differs if only the states between n=1 and n=4 (nmax=4) are simulated compared to the simulation of the excited states up to n=12. However, the change of the relative population decreases when taking more excited states into account since the probability for electron, ion and impurity impact excitation decreases with the increase of the energy difference between the initial and final states (see chapter 8.4). Therefore, it is not necessary to take more than 12 excited states into account. To further validate the collisional radiative model of F90FIDASIM, it has been compared to the one provided by ADAS [67]. The relative population of the n=3 state that results when applying the ADAS routines is shown in figure 4.13 with black diamonds.

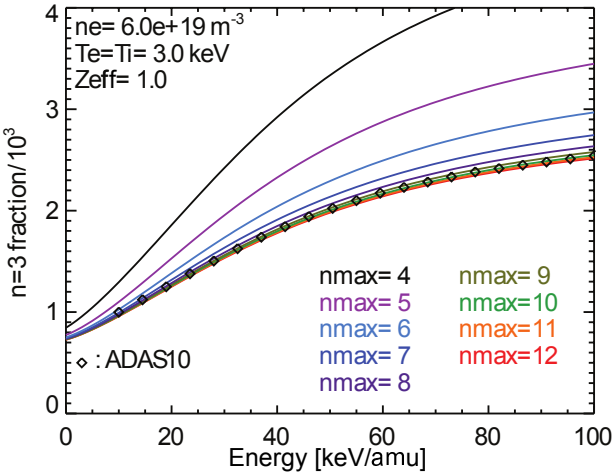

Figure 4.13: Population of the n=3 state relative to the n=1 state for neutrals with energies between 0 and 100 keV/amu. Different numbers of excited states (nmax) have been taken into account when calculating the relative population of the n=3 state by the collisional radiative model of F90FIDASIM. The black diamonds show the relative population of the n=3 state determined by the collisional radiative model of ADAS.

A very good agreement is obtained between the two collisional radiative models which show that F90FIDASIM consistently models the excitation and de-excitation of neutrals.

4.2.2 Comparison to the beam density profiles from TRANSP

The TRANSP code not only yields fast-ion distribution functions but also 3D deposition profiles of the fast-ions injected by NBI. These can be converted into beam density profiles by summing for every radial position over the deposited particles that are situated at lower radii. In figure 4.14, the predicted radial density profiles of beam neutrals in the n=1 state from TRANSP is compared to results from F90FIDASIM for the three energy components. As can be seen, a good agreement is obtained between F90FIDASIM and TRANSP. The differences between the two codes are the highest, with about 10 percent, at low radii where the beams have already penetrated deep into the plasma (the magnetic axis is located at about 1.65m). The differences might be due to different approaches that are used to model the beam neutrals. In contrast to F90FIDASIM, TRANSP calculates the attenuation of neutrals only in the ground state and then applies attenuation factors that account for the excited states. Furthermore, different atomic rates and cross-sections are used. While F90FIDASIM only uses the fundamental cross-sections from mainly Janev and Smith [63], TRANSP typically uses processed attenuation factors provided by ADAS.

4.2.3 Validation using a beam imaging diagnostic

A beam imaging diagnostic has been used to verify the description of the NBI geometry used in F90FIDASIM and to verify the simulation of beam and halo neutrals. The beam imaging diagnostic has a viewing geometry similar to the toroidal view of the FIDA diagnostic and observes radiation in the visible range with a CMOS camera. The camera operates with a time resolution of 200 μs and uses 256×256 pixels. In particular in low density plasmas, a clear contribution from the beam and halo radiation is visible in the camera frames. Figure 4.15 shows on the left a camera frame that has been measured in discharge #26381. On the right, the same camera frame is shown in which the background radiation, observed when NBI was off, has been subtracted. The so-called active radiation observed by the camera

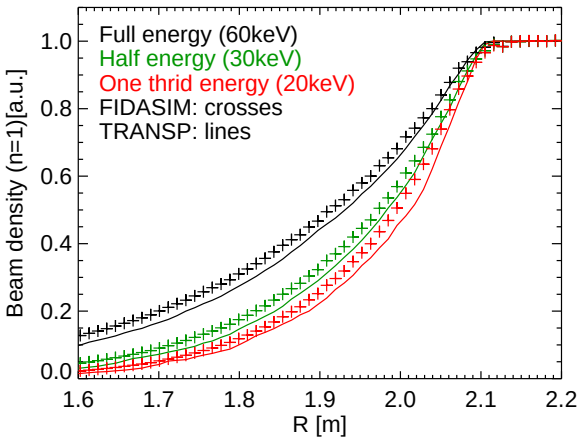

Figure 4.14: Density of beam neutrals with full, half and one third of the injection energy (60 keV) in the n=1 state. The crosses are the results from F90FIDASIM. The lines show the results from TRANSP.

mainly consists of D-alpha radiation from beam and halo neutrals as the active radiation from other contributions such as impurity charge exchange lines are much weaker in the visible range. Therefore, the measured footprint can be compared with the beam and halo radiation predicted by F90FIDASIM.

The beam and halo radiation has been calculated by F90FIDASIM for 4096 LOS that correspond to the viewing directions along every 16th camera pixel. The sum of the resulting halo and beam spectra have been integrated in wavelength for every LOS and are shown in figure 4.15 by red contour lines. To be able to better compare the simulation to the measurement, figure 4.16 shows the data of a vertical and a horizontal cut which are indicated in figure 4.15 with dotted lines. As can be seen, a very good agreement is obtained between the measurement and the simulation. This indicates that the geometry of NBI in terms of the vertical angle, the focus and the divergence is well described by the inputs to F90FIDASIM. Moreover, the good match between the predicted attenuation of NBI and the measurement shows that the collisional radiative model used in F90FIDASIM is valid. Last, it is worth mentioning that the halo radiation strongly contributes to the measurement of the beam imaging diagnostic. The good match between the measured and simulated footprint of NBI consequently shows that the model of the halo contribution used by F90FIDASIM is appropriate.

4.2.4 Validation using a beam emission spectroscopy diagnostic

In addition to the measurements with the beam imaging diagnostic, measurements with a beam emission spectroscopy (BES) diagnostic have been analyzed that are resolved in wavelength. The measurements can consequently be compared to the beam and halo spectra simulated by F90FIDASIM. The BES diagnostic uses toroidal LOS situated next to the FIDA diagnostic [68] and observes the beam emission at wavelengths above 656.1 nm. It has a high spectral resolution and is adjusted such that the red and the blue shifted part of the D-alpha radiation can be observed. Thereby, it enables to also study the halo radiation. In figure 4.17, active spectra (the passive radiation without NBI has been subtracted) are shown that correspond to two different radial locations. In addition to the active spectra, the sum of the simulated beam and halo radiation is illustrated in red. The simulated spectra of the full, half and third energetic beam neutrals are shown in three different colors from yellow to orange. As can be seen, the shape, as well as the intensity, of the measured beam

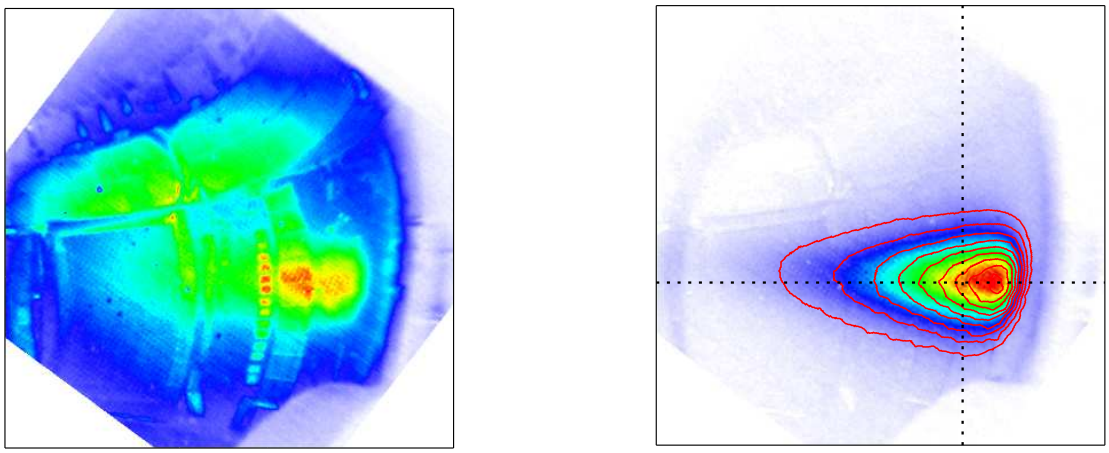

Figure 4.15: Left: measurement of a beam-imaging diagnostic during operation of NBI. Right: active frame in which the passive radiation has been subtracted. In addition the simulation from F90FIDASIM is shown with red contour lines.

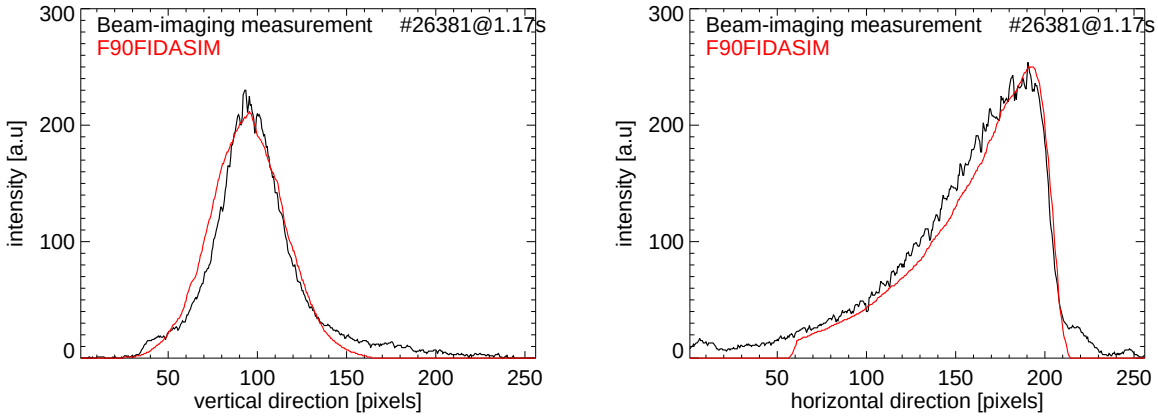

Figure 4.16: Horizontal and vertical cut through figure 4.15 that are indicated by the dotted lines.

emission agrees with the simulation. This shows that the NBI parameters such as the species mix, the geometry, the divergence, the power and the injection energy are well described by F90FIDASIM. Furthermore, the good agreement shows that the input kinetic plasma profiles, as well as the applied collisional radiative model, are appropriate. The simulated spectra of the halo neutrals are shown in green color. They also fit the measurement well. This indicates that the new approach, describing the halo neutrals by several generations, is valid. Finally, it is worth mentioning that this result, together with the previous sections, also validates the simulation of the FIDA radiation because F90FIDASIM employs the same geometry, algorithms and cross-sections when calculating the radiation emitted by beam, halo and FIDA-neutrals.

4.3 Sensitivity study

The dependence of the beam, halo, FIDA and Bremsstrahlung radiation on changes of the kinetic plasma parameters has been investigated in a sensitivity study. Several F90FIDASIM simulations were performed for discharge #27237 and for the toroidal LOS of the FIDA diagnostic at AUG in which the electron density and temperature, the ion temperature, and the Z_{eff} profiles have been scaled artificially. Figure 4.18 shows the relative changes

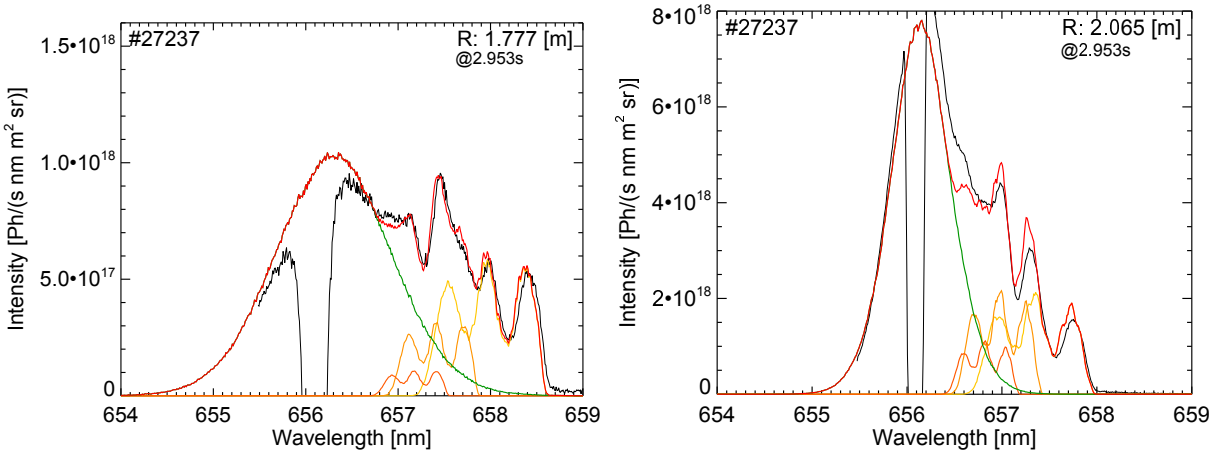

Figure 4.17: Measured active spectra of a beam emission spectroscopy diagnostic at two radial positions (purple), compared to the simulation by F90FIDASIM. In yellow, the simulated radiation of the full, half and third energetic beam neutrals is shown. The predicted radiation from the halo neutrals in indicated in green color. The sum of the simulated contributions is displayed in red. At 656.1nm, the cold, passive D-alpha radiation from the plasma edge is present which is very intense. The BES diagnostic is saturation at this wavelength at a constant photon flux. By subtracting the background radiation to obtain the active spectra, the saturated passive D-alpha line consequently becomes zero.

of the total intensity of beam, halo, FIDA and Bremsstrahlung radiation as a function of the variation of the input parameters. On the right, the effects when varying the electron temperature, the ion temperature and the effective charge are displayed for one LOS. As can be seen, the dependence on variations of these parameters is relatively small. However, it should be noted that the variations in the Z_{eff}, T_e and T_i profiles change the halo population and can thereby vary the level of the FIDA radiation. Furthermore, it should be noted that the measurement of the effective charge has typically large uncertainties. Therefore, it is good to know that the impact of uncertainties of the Z_{eff} level does not significantly influence the FIDA radiation.

On the left side of figure 4.18, the effect when changing the electron density is shown. The variation of the predicted spectra is given for three LOS that intersect NBI at different radial positions. As can be seen, the dependence on the variation of the electron density is strong. For example, when reducing the electron density by the large amount of 30%, the FIDA radiation increases by up to 80% (close to the plasma center at rho=0.08). Thus, uncertainties in the input electron density profiles would result in even larger uncertainties in the simulated spectra. The typical uncertainties in the density measurements at AUG are in the range of 10%. Hence, the simulation of the FIDA radiation would exhibit uncertainties that are in the order of 20%. This shows that not only the uncertainties in the modeled spectra can be high. It also shows that, when analyzing relative changes of the FIDA radiation, possible changes of the electron density profiles need to be analyzed in detail. Fortunately, the FIDA measurement itself provides a possibility to validate electron density profiles as the measured spectra contain the beam, halo and bremsstrahlung radiation. As these three contributions also strongly depend on the electron density (e.g. the beam-emission changes by 50% when reducing the electron density by 30%) the experimental profiles can be validated.

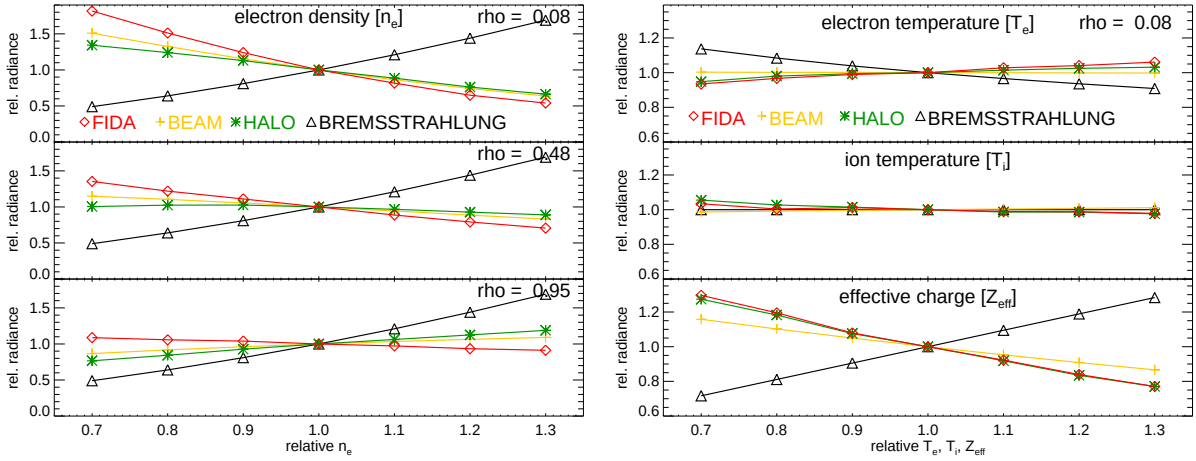

Figure 4.18: Sensitivity study performed for discharge #27237. The kinetic profiles (T_e, T_i and n_e) have been varied relative to the ones displayed in figure 4.2. The level of the effective charge, Z_{eff}, has been varied around a value of 1.5 as the value measured in #27237 was to low for a variation. The relative radiances correspond to the integration over all wavelengths. The strongest variation is observed when varying the electron density. Therefore, the dependence of the electron density is shown on the left for three different radial positions.

4.4 Summary

F90FIDASIM is used to predicted synthetic spectra consisting of the beam, halo and FIDA radiation. It is based on FIDAsim but has been rewritten in Fortran90 and significantly extended. For example, a new approach to simulate halo neutrals has been implemented.

The code models the beam and halo neutrals and the neutralized fast-ions via a Monte Carlo approach in a 3D simulation grid. A time dependent collisional radiative model is applied in every cell of this grid along the path of a simulated particle which uses updated cross-sections between n=1 and n=12 and which applies an analytical solution to determine the particles population of the atomic states.

So called weight functions have been developed that enable to calculate synthetic FIDA spectra without using the standard Monte Carlo approach. In addition, the weight functions can be used for a tomographic reconstruction of the fast-ion velocity space with lines of sight that have different angles to the magnetic field lines and they allow calculating conversion factors from the measured FIDA radiances to approximate fast-ion densities.

The code has been successfully validated by comparing the simulated beam density profiles to the predictions from TRANSP. Furthermore, F90FIDASIM has been tested by comparing the simulated radiation of beam and halo neutrals to the measurements of a beam imaging and a beam emission spectroscopy diagnostic.

Finally, a sensitivity study has evidenced that the FIDA radiation, as well as the beam and halo radiation, strongly depends on the electron density which makes a sophisticated measurement of this parameter essential when investigating the FIDA measurement with F90FIDASIM.

Chapter 5

Properties of the FIDA diagnostic at ASDEX Upgrade

The FIDA diagnostic at ASDEX Upgrade has been built during this Ph.D thesis. It consists of two optical heads situated inside the vacuum vessel which view the region of interest in the plasma. Optical fibers guide the collected light outside of the tokamak to a spectrometer where the spectra are monitored by a charge-coupled device (CCD) camera. In this chapter, first the spectrometer and camera setup are described with a focus on the wavelength and intensity calibration. Then, the line of sight (LOS) setup and the role of active and passive contributions present in the measured spectra are presented. Finally, the determination of radial FIDA intensity profiles and the observed parts of the fast-ion velocity space are discussed and a short summary is given.

5.1 Spectrometer and camera setup

The FIDA spectrometer was designed and built with the aim to obtain a high throughput of photons and a good spectral resolution simultaneously. A Czerny-Turner like spectrometer that uses two lenses with a focal length of 180mm and an F-number[1] of 2.8 instead of two focusing mirrors (see figure 5.1) was selected. The first lens, i.e. the collimator lens, parallelizes the light for the grating. The second lens, i.e. the camera lens, focuses the dispersed light onto a CCD camera that is attached to the spectrometer exit. The design

[1] F=focal length/lens diameter

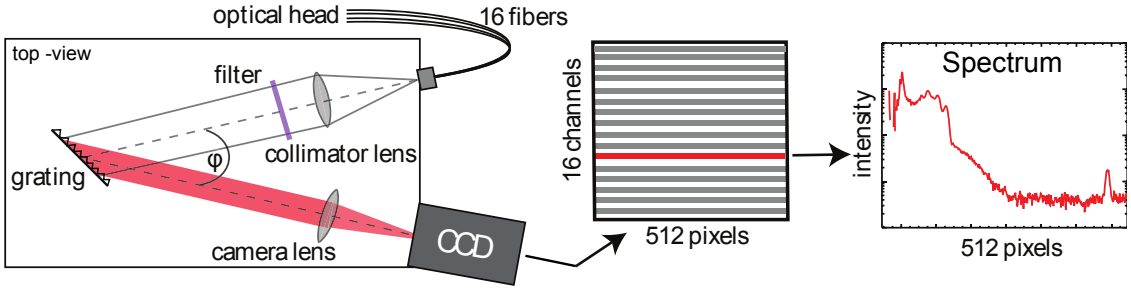

Figure 5.1: Schematic illustration of the FIDA spectrometer and camera setup (top-down view). 16 fibers can be connected at the spectrometer entrance in the vertical direction that are imaged onto the CCD camera. The different wavelengths are measured by 512 pixels in the horizontal direction and yield a spectrum for each of the 16 channels.

Spectrometer	
slit width	100 μm
channels	16
entrance lens	180 mm
camera lens	180 mm
grating	2000 lines/mm
observed order	-1
opening angle	20°
Camera	
manufacturer	Princeton Instruments
product name	ProEM 512B
number of pixels	512×512
pixel size	16×16 μm
readout time	2 ms
dynamic range	16 bit
readout frequency	10 MHz

Table 5.1: Specifications of the FIDA diagnostic

enables to plug an array of 16 vertically stacked fibers (the LOS) to the spectrometer entrance because the grating disperses only in the horizontal plane. The light from the different channels can consequently be observed at different vertical positions on the CCD whereas the horizontal direction of the CCD captures the dispersed radiation at different wavelengths. The theoretical spectral resolution, i.e. the observed wavelength range per pixel, can be expressed by:

$$d\lambda = \frac{\cos(\beta)\ w_{pix}}{f\ g\ |O|} \tag{5.1}$$

where w_{pix} is the width of the camera pixels, f is the focal length of the camera lens, g is the number of lines per mm of the grating, O is the diffraction order and β is an angle defined by:

$$\beta = 0.5\varphi + \arcsin\left(0.5\ O\ g\ \frac{\lambda_0}{cos(0.5\varphi)}\right) \tag{5.2}$$

where φ is the opening angle of the spectrometer and λ_0 is the central wavelength observed on the CCD. The specifications of the FIDA diagnostic are shown in table 5.1. Hence, the theoretical resolution at 656 nm is 0.027 nm per pixel. The spectral range that can be observed by the diagnostic is consequently 512×0.027nm$\sim$ 14 nm. Typically, the wavelength range between 655 nm and 669 nm is observed in FIDA measurements. It should be noted that the spectrometer can change the angle of the grating using a sinus drive. Spectral regions between 350 nm and 700 nm can thereby be analyzed.

The actual spectral resolution of the spectrometer is smaller than the theoretical resolution per pixel because equation 5.1 does not account for the diagnostic instrument function. The instrument function includes all effects that cause a narrow spectral line to be imaged with a certain width and shape onto the CCD camera. It consists of the errors of the lenses and the grating, as well as the width of the spectrometer entrance slit. The latter dominates the instrument function. The fibers at the spectrometer entrance are imaged one to one onto the CCD. Hence, the 400 μm fibers would cover a range of $\frac{400\mu\text{m}}{16\mu\text{m/pixel}} = 25$ pixels and a narrow emission line would be observed with at least a spectral width of 25 pixel$\times$0.027 nm/pixel= 0.67 nm.

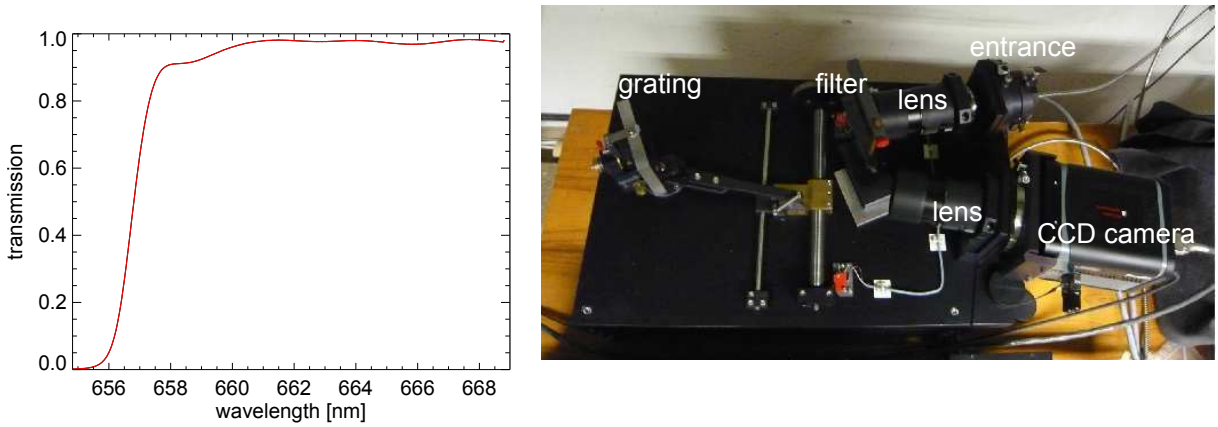

Figure 5.2: Left: Transmission curve of the interference filter situated after the spectrometer's collimator lens, measured by a central channel. Right: Picture of the spectrometer showing the grating, lenses, camera and the interference filter.

For this reason, the spectrometer has been equipped with an adjustable entrance slit that is typically set to 100 μm. Thereby, the spectral resolution is 0.16 nm which is a good compromise between the achieved resolution and the photon throughput of the spectrometer because the slit blocks parts of the incoming radiation.

The FIDA spectrometer is equipped with a high pass interference filter, located in between the collimator lens and the grating. The filter is used to block the intense radiation from the un-shifted D-alpha emission at 656.1 nm that might cause scattered light in the spectrometer and that would saturate in the measured spectra. Saturation must be avoided as it can affect the measurement even at wavelength positions, i.e. pixels, that are distant to the saturated ones. In addition, a strong overexposure can even damage the camera.

The measured transmission curve of the filter is plotted in figure 5.2 for one channel. It is shown how the filter attenuates the radiation below 657 nm while it has a high transmission at higher wavelengths. This is suitable for the FIDA measurements performed at AUG because only the red-shifted part of the spectrum is observed (see section 5.4).

5.1.1 Camera operation and data storage

A CCD camera with a low level of noise and a large quantum efficiency is used for the FIDA diagnostic because the intensity of the FIDA radiation is low. The camera is cooled to -70° C by a Peltier element to reduce the thermal noise and it uses an electron multiplication (EM) gain of the generated photo electrons to reduce the readout noise. It has a quantum efficiency of about 90% at 650 nm and a sensitive area of 512×512 pixels. The camera's CCD chip is back-illuminated and works in the frame-transfer mode where the photo-electrons, collected per pixel, are shifted to a non-illuminated part of the chip after a defined exposure time. At the non-illuminated part of the CCD, the photo-electrons are read out with a frequency of 10 Mhz which yields a minimum readout time of about 27 ms for all 512×512 pixels. However, this readout time can be decreased by binning the pixels in the vertical direction. 16 rows of binned pixels are defined that correspond to each of the fibers, connected at the spectrometer entrance, which yield a readout time of 2 ms.

The camera is operated from a Windows PC and is triggered by a separate module. Typically, 4200 trigger signals with a time-interval of 2 ms are defined to cover the duration

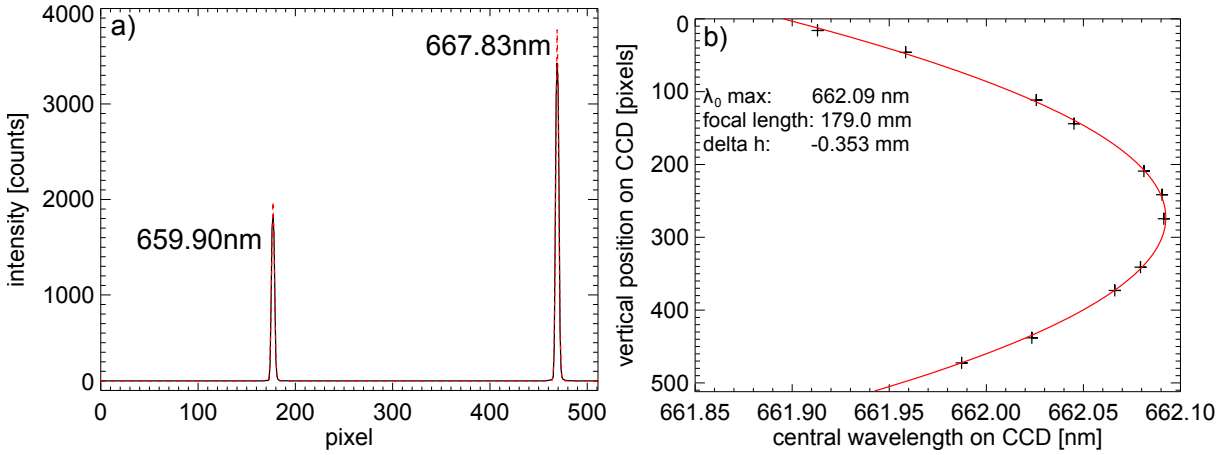

Figure 5.3: a) Measured spectrum of the Neon lamp between 655 nm and 668 nm that is fitted by two Gaussian curves (shown in red) b) Measured central wavelength on the CCD as a function of the channels vertical position on the chip. A fit to the data with a parabola is shown in red.

of plasma discharges at AUG. After the acquisition by the camera, the data is stored in a database of so called shotfiles. The shotfiles consist of the CCD data as well as settings of the diagnostic such as the central wavelength, the exposure time, the applied EM-gain and the names of the LOS connected to the spectrometer.

5.2 Calibration

The CCD camera yields a number of counts per pixel and per second. In oder to obtain spectra as a function of the spectral radiance and wavelength, a calibration must be performed.

5.2.1 Wavelength calibration

The wavelength calibration of the spectrometer is performed by analyzing the spectra of a Neon lamp that has two main emission lines between 656 nm and 670 nm (see figure 5.3a). By knowing the reference wavelengths of these lines from [69] and by determining their positions on the CCD with a Gauss-fit, the central wavelength observed by the CCD-camera can be determined.

One difficulty of the wavelength calibration is that the different channels on the CCD have different central wavelengths. Due to the vertical arrangement of the fibers at the spectrometer entrance, the parallel light, produced by the collimator lens, has an angle in the vertical plane to the grating. As can be seen in figure 5.3b, the central wavelengths, observed by the different channels, i, are situated on a parabola defined by:

$$d\lambda(i) = \lambda_0 \left(1 + 0.5 \left(\frac{h(i) - \triangle h}{f}\right)^2\right) \tag{5.3}$$

where $h(i)$ denotes the vertical position of a given channel on the CCD and $\triangle h$ is the misalignment between the vertical position of the central pixel of the CCD and the vertical position of the center of the two lenses. The wavelength calibrations are performed every time the spectrometer's grating is moved. Thereby, only one channel needs to be connected to the neon lamp because h, $\triangle h$ and the focal length, f, are constant and well known.

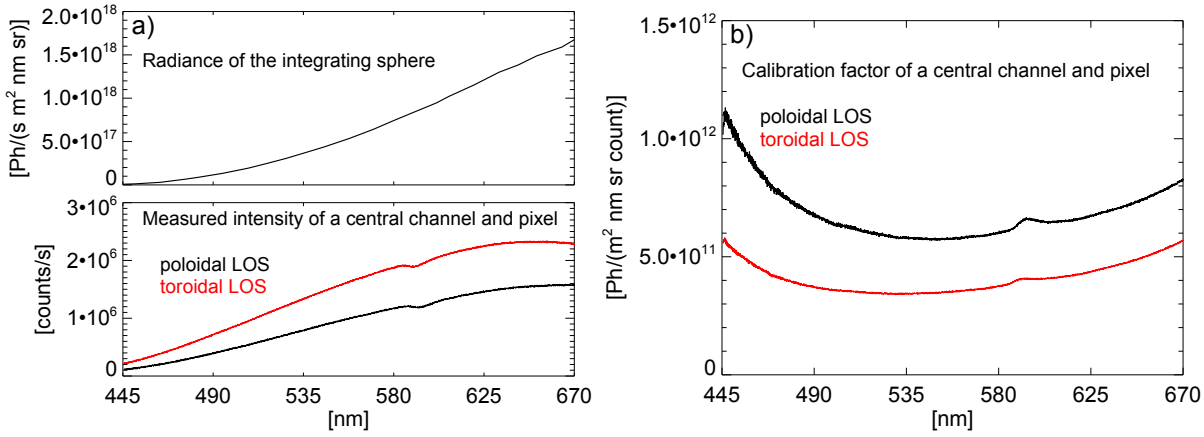

Figure 5.4: a) Tabulated radiance of the integrating sphere (upper plot) and measured counts/s of the central pixel of a toroidal and a poloidal channels (lower plot) that were connected to the integrating sphere as a function of wavelength. b) Corresponding calibration factors for the toroidal and poloidal channel

5.2.2 Intensity calibration

To obtain spectra as a function of [photons/(s nm m^2 sr)] instead of [counts/s], the diagnostic is calibrated with an integrating sphere. The integrating sphere is placed in front of the optical heads inside the vacuum vessel and emits spatially uniform light in the visible range with a well known, continuous spectrum. Figure 5.4a (upper plot) shows the reference emissivity of the integrating sphere as a function of the wavelength between 445 nm and 670 nm. The lower plot of figure 5.4a shows the measured intensities in [counts/s] of two central camera pixels of a so called poloidal and a toroidal channel (explained in the following section) that have been illuminated by the integrating sphere. By moving the spectrometer grating during the illumination, the wavelength range between 445 nm and 670 nm has been scanned. As can be seen, the emissivity of the sphere, and consequently the measured photon fluxes, increase towards higher wavelengths.

The calibration factors in figure 5.4b are determined by dividing the radiance of the sphere by the measured counts per channel and pixel. Due to the wavelength dependent quantum efficiency of the CCD camera, the transmission curve of the fibers and due to the reflection dependence of the grating, the diagnostic is most sensitive at about 500 nm. The toroidal LOS have a higher photon throughput than the poloidal ones because the optical head of the toroidal views uses newer fibers with less connections.

It should be noted that the calibration measurement is performed without using the camera's EM-gain and without the interference filter. Therefore, the calibration factors have to be divided by the transmission curve of the filter and the EM-gain must be taken into account which is typically set to 15 and which has a linear dependence. As shown in figure 5.5, the quantity of measured photo-electrons linearly increases with the applied EM-gain below a value of 30.

Before applying the calibration to the data from the camera, the latter must be corrected by an offset and by the smear effect. The offset is added to the data to avoid negative values. Its value is constant in time and can therefore be obtained from measurements during which the CCD is not illuminated. The smear effect originates from the readout procedure of the camera. As already mentioned, the camera is operated in the frame-transfer mode. After the exposure time, the pixels are shifted to a non-illuminated region of the chip. The time to shift the horizontal rows of pixels by one pixel is 0.6 μ. The camera consequently needs about 310 μs to shift the whole chip of 512 rows to the non-illuminated region. Within this time,

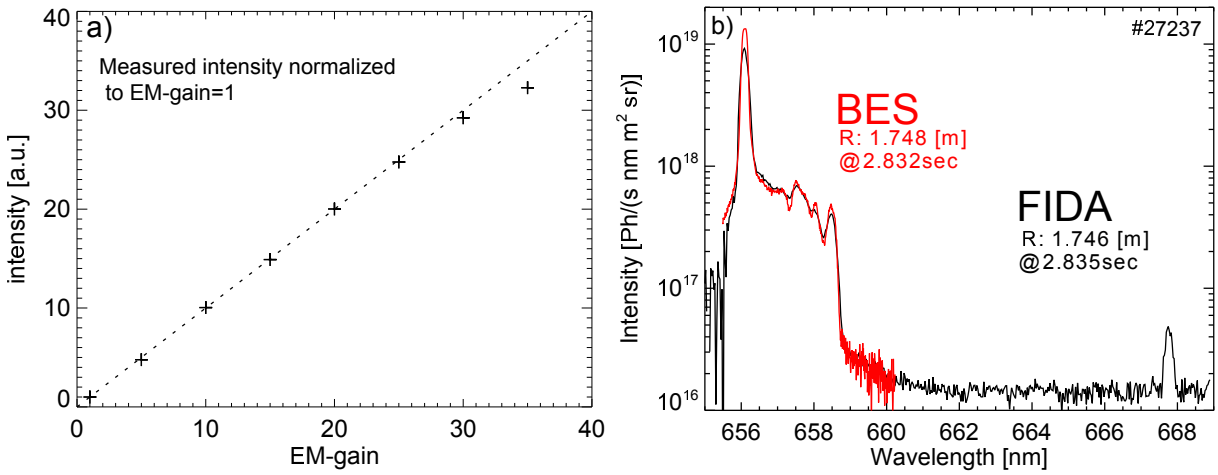

Figure 5.5: a) Measured photon-electrons as a function of the EM-gain, normalized to gain 1. The EM-gain amplifies the photo-electrons linearly up to a gain of $\sim$ 25 b) Comparison of the measured spectra from a BES diagnostic (red) and the FIDA diagnostic (black). The good agreement in the intensity and shape indicates that the intensity calibration is valid

the pixels gather light from other channels which results in smeared spectra. In particular when using short exposure times such as 2ms this effect needs to be corrected. In the AUG FIDA diagnostic one of the 16 channels is not connected to a fiber. It only measures the smeared light which can then be subtracted from the other, illuminated channels.

In order to check the intensity calibration of the FIDA diagnostic, the tabulated radiance of the integrating sphere, used for the calibration, has been validated with a second, newer sphere. Thereby, a very good agreement has been found. In addition, the measured and calibrated spectra have been compared to the ones of a beam emission spectroscopy (BES) diagnostic that has toroidal LOS next to the FIDA diagnostic. In figure 5.5b, the spectra acquired by two adjacent LOS of the two diagnostics are compared. As can be seen, the two spectra are consistent in intensity and shape which indicates a good reliability of the FIDA diagnostic's intensity calibration.

5.2.2.1 Statistical noise in the spectra

The noise contained in the measured spectra mainly consists of the photon noise and the readout noise. The readout noise can be determined from non-illuminated camera frames and is well described by a Gaussian distribution (see figure 5.6). The photon noise follows the Poisson law and can be expressed by:

$$\sigma_{ph} = \sqrt{N_{ph}} = \sqrt{N_{counts} \cdot f_{conv}} \tag{5.4}$$

where N_{ph} is the number of photons that arrives at the CCD camera. It can be calculated from the measured counts, N_{counts}, and a conversion factor from counts to photons, f_{conv}. The conversion factor can be determined from the noise contained in the measured spectra which is represented by the intensity fluctuation between two adjacent pixels, caused by the photon noise. As an example, figure,5.6 shows the square of the measured level of noise between two pixels (red crosses) as a function of the intensity in counts. Clearly, the data for different count levels is consistent with a conversion factor of 2.45 photons/count that is represented by the dashed line.

By applying the Gaussian error propagation the uncertainties, σ, of the measured spectra,

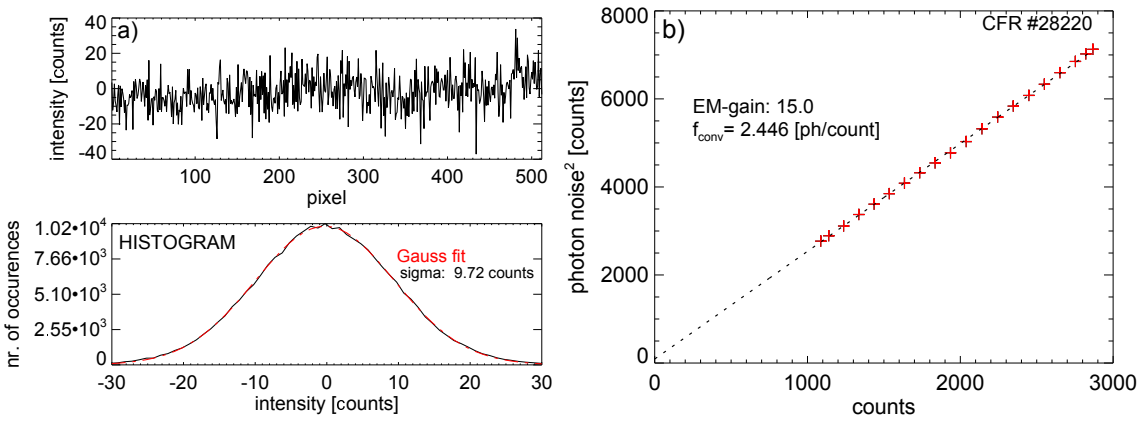

Figure 5.6: a) Measured spectrum without illuminating the CCD (upper plot) and corresponding histogram calculated for several frames and channels. In red, a Gaussian fit to the data is shown. b) Square of the measured photon noise between two neighboring pixels as a function of counts. The data well agrees with a conversion factor from counts to photons of 2.45, represented by the dashed line.

imposed by the readout and photon noise, can be determined:

$$\sigma = \sqrt{\sigma_{readout}^2 + N_{counts} \cdot f_{conv}} \tag{5.5}$$

It should be noted that the uncertainties caused by the correction of the offset and the smear effect are not taken into account in equation 5.5 because they have a small contribution to the noise. The offset is measured in multiple frames and the smear spectra are smoothed over several pixels and consequently contribute little to the level of noise.

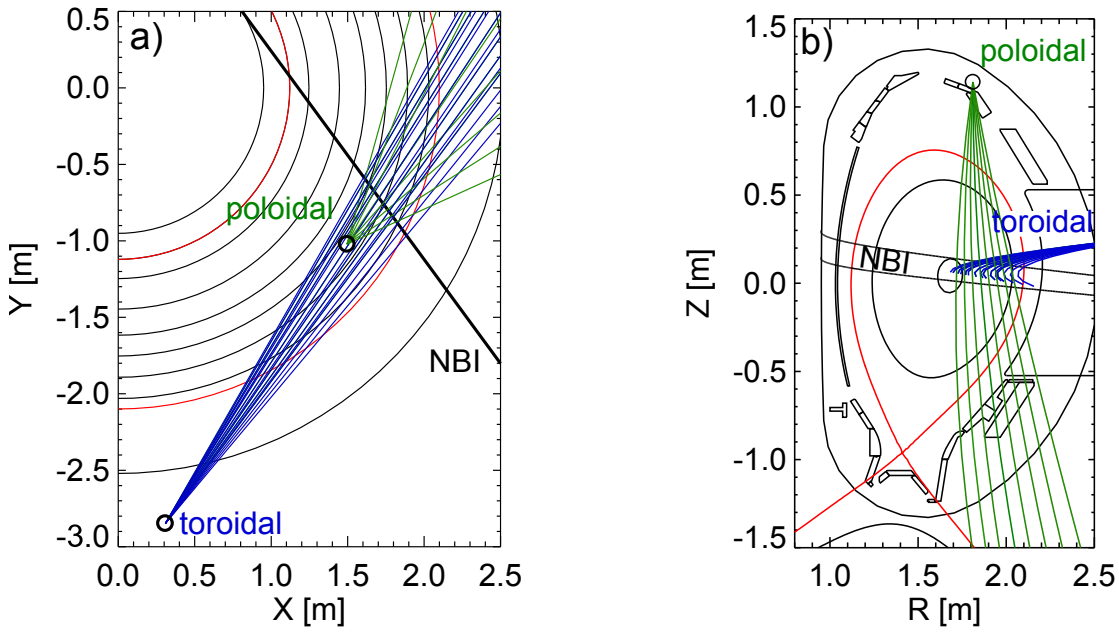

Figure 5.7: Top-down (a) and a poloidal view (b) on the LOS-setup of the FIDA diagnostic at AUG. The toroidal LOS are indicated in blue color and the poloidal ones are shown in green.

5.3 Line of sight setup

The FIDA diagnostic has toroidal and poloidal LOS that are focused on the 60 keV heating beam NBI3. A poloidal and a top-down view on the AUG tokamak is shown in figure 5.7 where the toroidal LOS are illustrated in blue color and the poloidal ones in green color. The optical head of the toroidal LOS is situated about 10 cm above the mid plane of AUG and has an F-number of 1.8. It consists of three horizontal rows of 30 lines of sight that are radially distributed along the NBI from the edge of the plasma to the plasma center. One row is used by the FIDA diagnostic, one by the BES diagnostic and one row is used by the charge exchange diagnostic (CER) that has been described in chapter 3. The radial resolution of the toroidal LOS is on average about 3 cm (2σ) which is determined by the different radii at which a given LOS intersects the density of beam and halo neutrals present along the NBI line. The optical head of the poloidal LOS is situated above NBI3. It has been installed in 2012 and consists of 11 radially distributed LOS. The viewing geometry is adjusted such that the LOS avoid the divertor region where intense passive radiation is present. The radial resolution of the poloidal LOS is on average 2 cm.

5.4 Active contributions in FIDA spectra at AUG

Active emissions are present in the FIDA spectra when the heating source NBI3 is turned on. They consist of impurity line emissions and active D-alpha radiation. The active impurity contributions present in FIDA spectra have typically negligible intensities. Only at 661.2 nm, an ArXVI(16-15) line, at 662.4 nm a CVI(15-11) line [70] and at 661.5 nm, an AlXIII(14-13) can be present whose intensities depend on the impurity content of the plasma. In contrast, the active D-alpha radiation is intense. It consists of the halo, the beam and the FIDA radiation. As the spectral shapes of these emissions depend on the viewing geometry, they are discussed separately for the toroidal and the poloidal LOS.

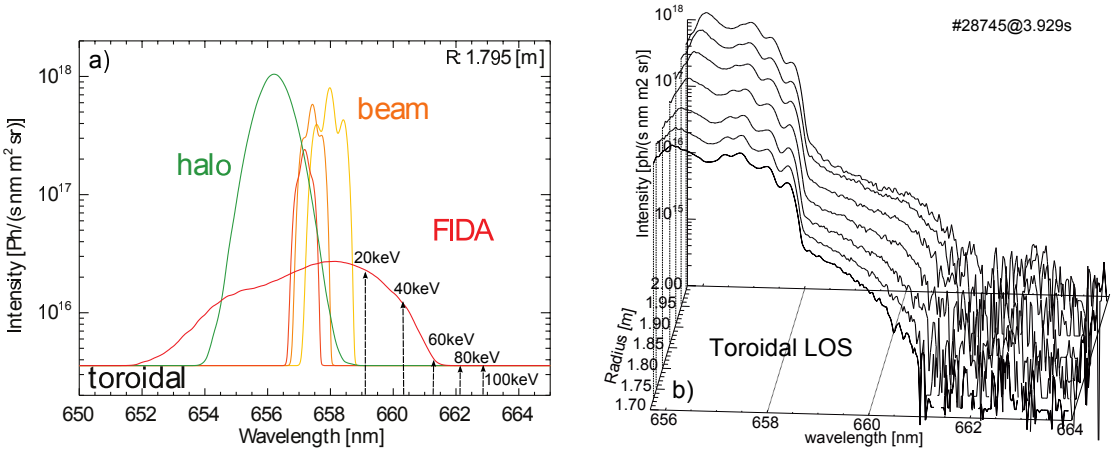

Figure 5.8: a) Simulated spectrum of a central, toroidal LOS consisting of the beam, halo and FIDA radiation. The FIDA radiation has been calculated for fast-ions injected by NBI3(60 keV) only. The arrows indicate wavelengths that correspond to fast-ion energies parallel to the LOS between 20 keV and 100 keV. b) Active spectra of 7 toroidal LOS acquired during NBI heating from source #3 only on a semi-logarithmic scale.

5.4.1 Toroidal LOS

A theoretical spectrum consisting of the beam, halo and FIDA radiation is shown in figure 5.8a for a central toroidal LOS. As can be seen, the beam emission is situated at red-shifted wavelengths (above 656.1 nm) which is due to the geometry of the LOS and the NBI. The absolute shift is relatively small despite the high velocity of the injected beam neutrals because the LOS intersect NBI3 with angles that range from 104° for the outer LOS to 112° for the central LOS (for an angle of 90°, no Doppler shift occurs). As this angle is larger for the inner LOS, they observe the beam emission at higher wavelengths than the LOS situated at the plasma edge. An example is given in figure 5.8b where measured active[2] spectra of 7 toroidal LOS are shown that were observed during operation of NBI3 only. The wavelength of the beam emission slightly increases from the LOS at 2 m to the LOS at 1.7 m.

The spectral position of the halo emission depends on the toroidal plasma rotation which is, in NBI heated discharges, usually co-current[3]. It is observed slightly red-shifted as the LOS point into the same direction. The intensity of the halo radiation is comparable to or even exceeds that of the beam emission and its width scales with the ion temperature. Depending on the plasma rotation and ion temperature, its spectral wings can reach large wavelength shifts. However, under standard plasma conditions present at AUG, such as plasma rotations below 250 km/s and temperatures below 6 keV, the halo radiation is not significantly present above 659.5 nm. Hence, the FIDA radiation, as shown in figure 5.8a and 5.8b, can be studied above this wavelength where it is not superimposed by intense active contributions. The wavelength range above 659.5 nm, which corresponds to fast-ions with at least 25 keV, is well suited to study the fast-ions generated by the NBI heating sources at AUG. The neutral beams inject into the co-current direction. In combination with the geometry of the LOS, this results in mainly red-shifted D-alpha radiation. As can be seen in figure 5.8b, a significant part of the FIDA radiation is observed at the wavelengths above 659.5 nm during the operation of NBI3. It should be noted that the FIDA diagnostic has been optimized for this wavelength range as only little FIDA radiation is present at the blue-shifted part of the D-alpha spectrum.

[2]The passive radiation has been subtracted.

[3]The relatively large torque induced by NBI injection (about 1 Nm per source) results in a counter-clockwise plasma rotation.

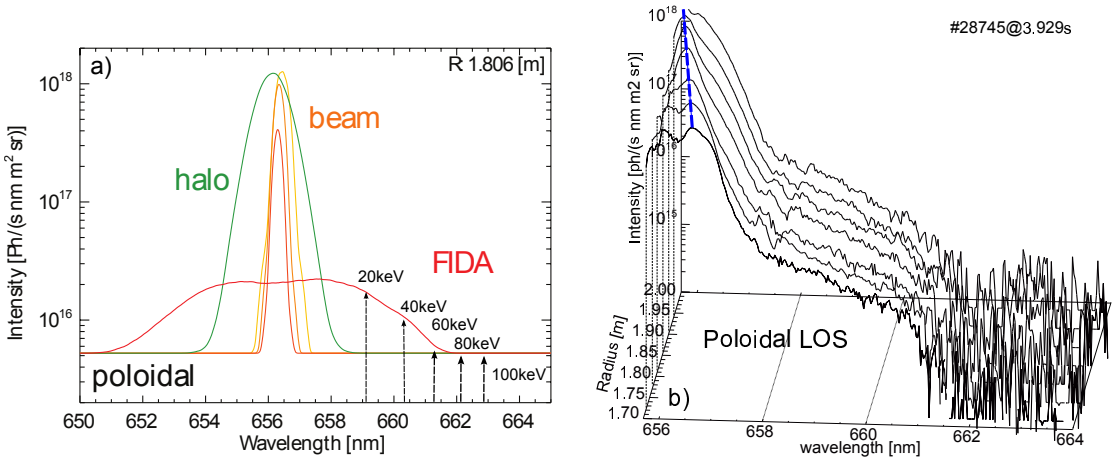

Figure 5.9: a) Simulated spectrum of a central poloidal LOS of the FIDA diagnostic consisting of the beam emission (orange) the halo emission (green) and the FIDA emission (red) present during the operation of NBI3. b) Active spectra on a semi-logarithmic scale for 7 poloidal LOS that were measured during heating from NBI3.

5.4.2 Poloidal LOS

The viewing direction of the poloidal LOS is more perpendicular to NBI3 than that of the toroidal LOS. The angles between the LOS and NBI3 range from 100° in the plasma center to 80° at the plasma edge. Consequently, the spectral shift of the beam emission is small and even changes from slightly red shifted for the central LOS to slightly blue shifted for the LOS close to the plasma edge. This can be seen in figure 5.9b where measured active spectra of 7 LOS, that intersect NBI3 between 1.7 m and 2 m, are shown. The blue, dashed line indicates the spectral position of the beam emission.

The halo emission in the poloidal spectra does not show significant spectral shifts as the poloidal plasma rotation is usually small. Therefore, even in plasmas with a large amount of NBI heating, i.e. high toroidal rotations, the halo radiation does generally not reach wavelengths above 659.5 nm. A simulated spectrum of the FIDA radiation, expected during heating from source NBI3, is shown in figure 5.9a. Its shape is rather symmetric around 656.1nm because the poloidal LOS are sensitive to the gyro motion of fast-ions. Therefore, it would be possible to study also the blue shifted part of the FIDA radiation. However, a different interference filter or other means to block the passive D-alpha radiation would be necessary in the spectrometer setup for such investigations. Therefore, this work focuses on the FIDA radiation situated above 659.5 nm.

5.5 Passive contributions in FIDA spectra at AUG

The passive radiation is present in the spectra even when NBI3 is off. Depending the the experimental conditions, it can be also present in the spectral region where the FIDA radiation is analyzed (between 659 nm and 663 nm) and then needs to be modeled, subtracted or excluded from the analysis. Otherwise it would contribute to the measurement uncertainties.

The passive radiation mainly consists of line emissions from the plasma edge which are impurity line emissions, D-alpha radiation, molecular lines and passive FIDA light. In addition, the Bremsstrahlung radiation is present in the spectra as a passive contribution that originates from the whole plasma.

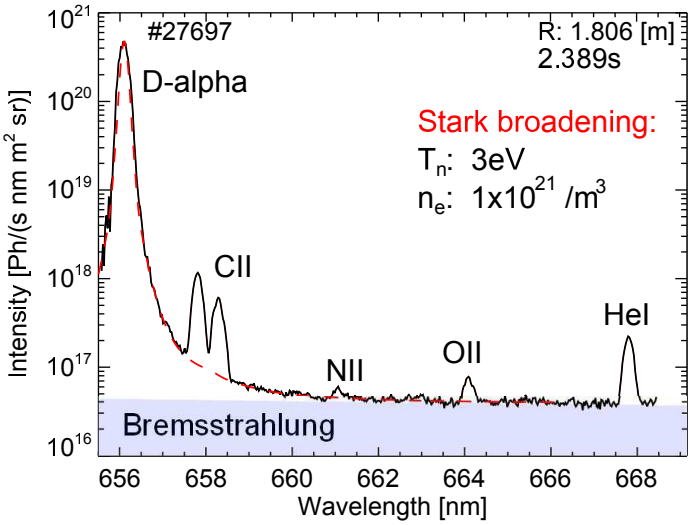

Figure 5.10: Passive spectrum of a poloidal LOS on a semi logarithmic scale that has been observed in the presence of an ELM crash. Two CII emission lines are present at 658 nm, an NII line is situated at 661.3 nm, an OII emission is visible at 664.1 nm, and at 667.9 nm, a HeI line can be seen. The shape of the D-alpha emission is compared to a theoretical curve (red) from [71] that accounts for Stark broadening.

5.5.1 Passive D-alpha line radiation

The passive D-alpha radiation is one of the brightest line emissions of high temperature D-plasmas in the visible range. It is caused by electron impact excitation and by charge exchange reactions of Deuterium neutrals and ions at the plasma edge and is about 100 times more intense than the FIDA radiation. The edge D-alpha emission can be monitored by the FIDA diagnostic because it is strongly attenuated by the interference filter placed inside the spectrometer (section 5.1). Due to its high intensity, the wings of the passive D-alpha radiation can be important for the analysis of the FIDA radiation. In particular, in the presence of high electron densities along the LOS (above 10^{20} m^{-3}), a non-Gaussian shape of the edge D-alpha emission is observed that is most likely due to Stark broadening [72]. Stark broadening is caused by electric micro fields, imposed by charged particles, that split the D-alpha emission mainly into 9 spectra lines (see chapter 4, figure 4.4). Since the strength of the electric micro fields imposed by a charged particle depends on its distance to a given emitting D neutral, different amplitudes of the electric fields and consequently different splittings appear. This leads in total to a broadening of the emission line. Figure 5.10 shows a passive spectrum of a poloidal LOS that has been measured in the presence of an ELM crash during which high electron densities appear along this LOS close to the divertor. Clearly, the passive D-alpha emission at 656.1 nm has a wing that is extended to larger wavelengths. In addition to the measurement, the theoretical shape of the D-alpha emission assuming Stark broadening is plotted with a red, dashed line. The shape, predicted by [71], has been convoluted with the diagnostic's instrument function. It corresponds to a temperature of neutrals of 3 eV and an electron density of 10^{21} m^{-3} and agrees well with the measurement. This suggests that Stark broadening needs to be taken into account when the LOS of the FIDA diagnostic intersect regions with high densities. It should be noted that an electron density of 10^{21} m^{-3} is high compared to the main plasma densities which are typically ten times smaller. However, in the transient phase during ELM crashes, such high densities can appear in the divertor region [72].

It should be noted that only the poloidal LOS are significantly influenced by the Stark broadening. The toroidal LOS of the FIDA diagnostic are unaffected as the LOS rarely intersect regions with densities above 10^{20} m^{-3} (even in the presence of edge-instabilities).

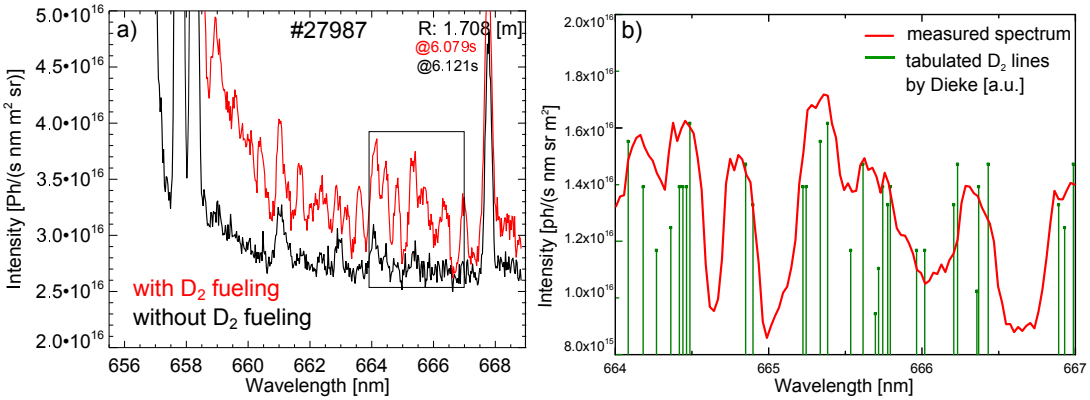

Figure 5.11: a) D_2 Molecular lines are present in CXRS spectra when using fueling from valves close to the diagnostic b) Comparison to the theoretical spectral positions of D_2 molecular lines from [73].

5.5.2 Passive impurity line emissions

As shown in figure 5.10, several line emissions from impurity ions can be present in the FIDA spectra. Typically, two CII lines at about 658 nm and a HeI line emission at 667.8 nm are present with a significant intensity. In addition, line emissions such as a NII line at 661.3 nm or a OII line at 664.1 nm might appear, depending on the impurity content of the plasma.

Compared to other machines like DIII-D or TEXTOR, the level of passive impurity line emissions is very low in FIDA spectra at AUG. This is in part due to the fully tungsten coated walls that yield a strongly reduced content of carbon and in part due to frequently applied boronizations that cover the walls with a thin layer of Boron. Boron acts as a chemical getter for oxygen and consequently decreases the impurity content of plasmas. Boron itself does not emit radiation between 659 nm and 669 nm.

5.5.3 D2 molecular lines

It was found that the use of D_2 fueling valves, situated close to the diagnostic's LOS, strongly affects the spectra and must therefore be avoided during FIDA measurements. Figure 5.11a shows spectra measured with and without D_2 fueling by a valve that is located close to the toroidal optical head of the diagnostic. The spectrum observed with the valve turned on is populated with narrow line emissions which are most likely D_2 molecular lines that correspond to different rotational and vibrational states. In figure 5.11b, a part of a measured spectrum shows a good agreement with the theoretical spectral positions of D_2 molecular lines from [73].

5.5.4 Passive FIDA radiation

Passive FIDA radiation is emitted by fast ions that undergo charge exchange reactions with neutrals at the plasma edge that are also present without NBI heating. It is generally negligible since the overlap of the fast-ion density and the edge neutral density is small. However, significant passive FIDA radiation has been observed in discharges which feature simultaneously high edge neutral densities and large edge fast-ion populations; for example, in the ramp up phase of discharges where off-axis injected fast-ions are poorly confined. Figure 5.12a shows a passive spectrum measured in the initial phase of a discharge that was performed with off-axis heating. The spectrum shows distinct steps in intensity at

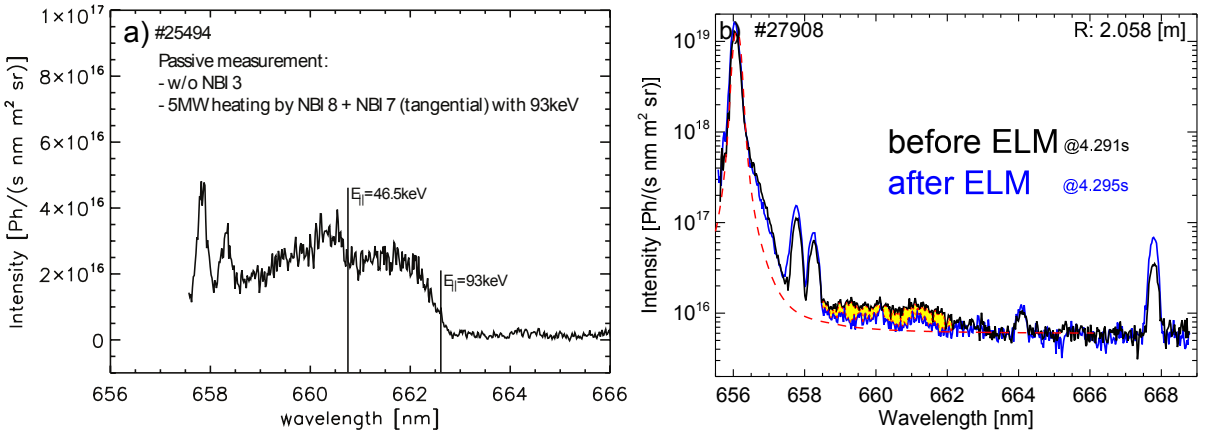

Figure 5.12: a) Passive FIDA radiation observed during high recycling and off-axis NBI with 93 keV. b) Change of passive FIDA radiation observed during D_2-fueling induced by an ELM-crash (b). In red, the theoretical shape of the edge D-alpha emission is shown that corresponds to an electron density of $2{\times}10^{21}\mathrm{m}^{-3}$.

wavelengths that correspond to the full (93 keV, 662.65 nm) and half (46.5 keV, 660.66 nm) injection energies of the NBI. This measured FIDA spectrum can only be of passive nature as NBI3 was off. Another example of measured passive FIDA radiation is shown in figure 5.12b. Here, 5 MW of off-axis NBI heating was applied and a high density of neutrals was present at the plasma edge by moderate D_2-fueling from a valve close to the LOS. As discussed above, D_2-fueling causes molecular lines in the spectra. In addition, it enhances the level of passive FIDA radiation. The two passive spectra shown in 5.12b correspond to time points before and after an ELM crash (black before, blue after). Clearly the CII and the HeI impurity line emissions are increased after the crash indicating that the edge-density of neutrals increases. In contrast passive FIDA radiation is lowered after the ELM crash, indicated in yellow, which can be explained by the fact that ELMs eject fast-ions from the plasma edge.

5.5.5 Bremsstrahlung

Bremsstrahlung originates from the whole plasma and appears as a flat offset in the spectra. As indicated in chapter 4, the level of bremsstrahlung depends on the electron density, temperature and the effective charge, Z_{eff}. The intensity of the radiation from Bremsstrahlung can be similar to, or even exceed the level of the FIDA radiation. It typically reduces the signal to noise ratio of the FIDA measurement since it contributes to the photon noise. To achieve reasonable signal to noise ratios when investigating the fast-ion confinement by FIDA spectroscopy, the level of Bremsstrahlung needs to be low, i.e. discharges with low densities (approximately below 8×10^{19} m^{-3} at AUG) and low Z_{eff} must be performed. These are conditions for which the fast-ion population is substantial in AUG. It should be noted that in future, large scale fusion experiments such as ITER, the level of Bremsstrahlung will be very high which will make FIDA measurements virtually impossible.

5.6 Radial profiles

Radial profiles of FIDA light are provided by the two set of LOS. By integrating the spectra of the various LOS over a specific wavelength range and by subtracting the contributions from passive radiation, a specific part of the fast-ion phase space can be analyzed. As an

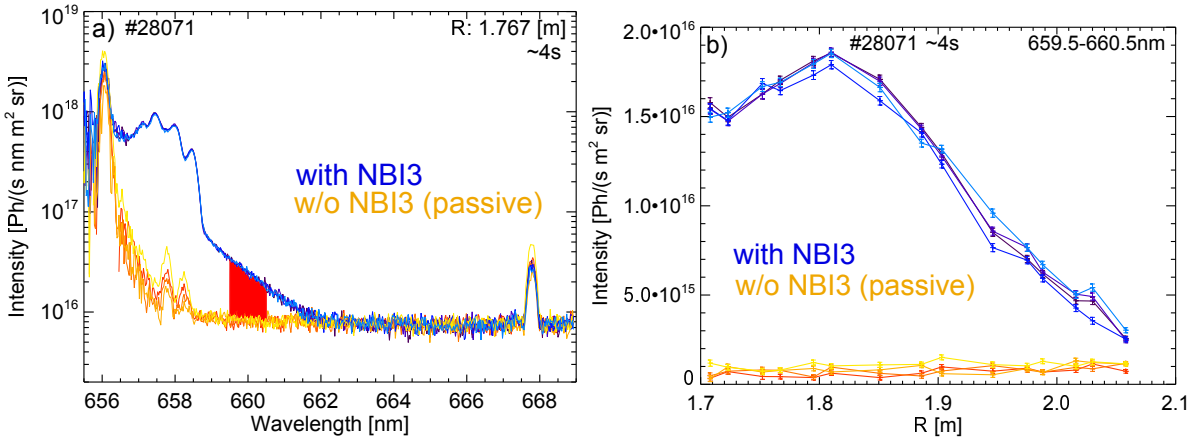

Figure 5.13: a) Measured spectra of a central toroidal LOS measured with (blue) and without the operation of NBI3 in addition to NBI8. b) Radial FIDA intensity profiles obtained by integrating the spectra of the 15 toroidal LOS between 659.5 nm and 660.5 nm. The blue profiles correspond to the active FIDA radiation. The yellow/orange profiles represent the passive radiation.

example, figure 5.13b shows in blue radial FIDA intensity profiles from 15 toroidal LOS where the integrated part of the spectra was between 659.5 nm and 660.5 nm (indicated in red in figure 5.13a). The statistical uncertainties for each point are displayed with error bars, derived from the photon noise and from the diagnostic's readout noise. In order to subtract the passive contributions from the radial FIDA intensity profiles, two different methods can be applied: One can either make use of the beam modulation technique in which passive spectra are directly measured and then subtracted from the total ones (as applied for figure 5.13b) or one can model the passive components within the active spectra. The latter enables continuous measurements. At AUG the clean (free from significant impurity lines) FIDA spectra permit to model the passive radiation by a horizontal line, representing only the radiation from Bremsstrahlung. Possible changes of the level of Bremsstrahlung can be seen via this 'horizontal line approximation' because the level of Bremsstrahlung is also observed in active spectra at wavelengths above 663 nm, where no emissions from fast ions (with the exception of ICRH acclerated fast-ions) are expected as these would correspond to energies well above 100 keV. The additional systematic uncertainties, which arise in the profiles when using the flat line approximation, can be quantified in passive radial profiles, i.e. in profiles that are calculated using passive spectra from which the flat line has been subtracted. In addition to the active radial FIDA intensity profile, figure 5.13b shows passive profiles in yellow/orange. The passive profiles exhibit a small, positive offset, explained by the contributions discussed in the previous sections. The fact that the offset slightly increases towards the plasma edge confirms its passive nature. Passive line radiation is localized at the plasma edge. In this region, the outer LOS are more tangential to the magnetic surfaces. Hence, they intersect the passive radiation on a larger length/volume. Due to the offset in the radial profiles, it can be difficult to interpret the absolute quantity of the continuously observed radial FIDA intensity profiles. However, it is possible to study the temporal evolution of the shape of radial profiles in continuous mode because it is maintained.

5.6.1 Observed velocity space

Due to the additional active and passive contributions present in the FIDA spectra, the FIDA radiation cannot be analyzed at all possible wavelength. Therefore, only certain regions of the fast-ion velocity space can be accessed by the toroidal and poloidal LOS. The parts of the velocity space covered by the toroidal and poloidal LOS between 659.5 nm and 660.5

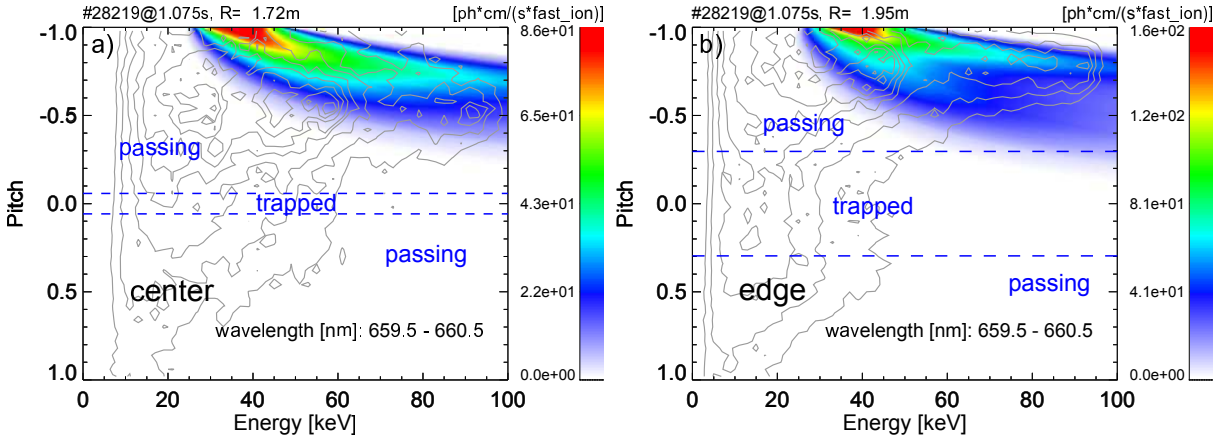

Figure 5.14: Observed velocity spaces of a central (a) and edge (b) toroidal channel, compared to the fast-ion velocity space distributions present during on-axis injection from NBI3 and NBI8 (a) and off-axis injection from NBI6 and NBI7 (b) shown by gray contour lines. The blue dashed lines indicate the trapped-passing boundaries of fast-ions.

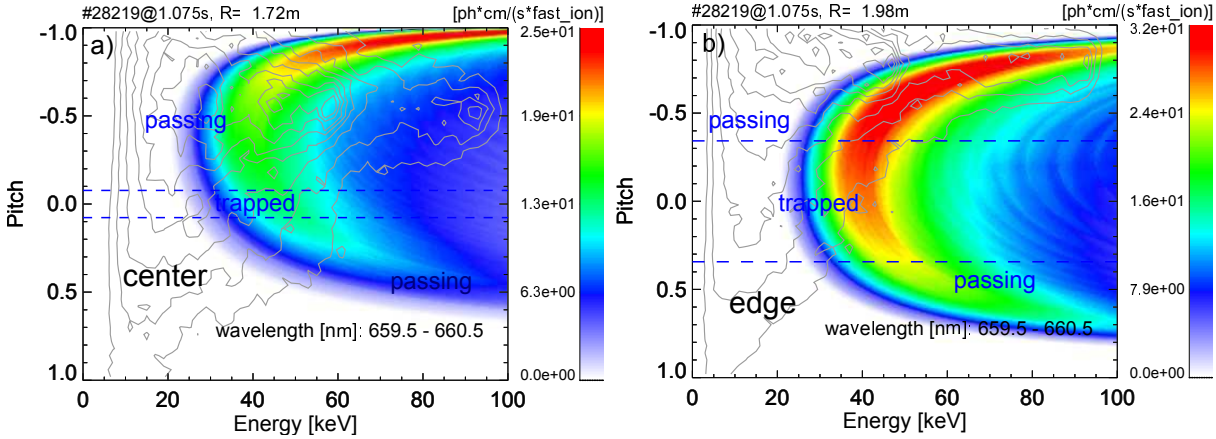

Figure 5.15: a) Observed velocity space of a central poloidal LOS compared to the distribution function of fast-ions from NBI3 and NBI8. b) Weight function of a edge-poloidal LOS combined with the velocity space distribution of fast-ions injected by NBI6 and NBI7. The trapped-passing boundaries are indicated by blue dashed lines.

nm, i.e the weight functions as discussed in chapter 4, are shown in figures 5.14 and 5.15 for two radial positions. At the defined wavelength range, the toroidal LOS are sensitive to co-rotating fast-ions, i.e. passing fast-ions with pitches close to -1. The poloidal LOS are also sensitive to fast-ions with smaller pitches, i.e. trapped fast-ions. In particular the velocity space covered by the poloidal LOS at the plasma edge comprise these trapped fast-ions. The trapped-passing boundaries are indicated by blue, dashed lines in figures 5.14 and 5.15. While the poloidal weight functions overlap the region defined by the tow lines, the toroidal weight functions are situated at larger pitches.

In addition to the weight functions, two example velocity space distributions of fast-ions are plotted in figures 5.14 and 5.15 in order to show that the weight functions well overlap with the fast-ions injected by the different on- and off-axis NBI sources present at AUG (see chapter 3). Figures 5.14a and 5.15a show by gray contour lines a fast-ion distribution function during on-axis injection from NBI3 (60 keV) and NBI8(93 keV). Figures 5.14a and 5.15a illustrate the fast-ion distribution function during the operation of the off-axis sources NBI6 and NBI7 (93 keV) in addition to injection from NBI3. As can be seen, there is a significant overlap between the slowing down distributions with both, the poloidal and the toroidal LOS. Hence, the toroidal as well as the poloidal LOS are well suited for FIDA

measurement at AUG. In addition, the differences between the toroidal and poloidal weight functions enable the study of velocity space dependent effects on the fast-ion confinement.

5.7 Summary

The two optical heads of the FIDA diagnostic, situated inside the tokamak, are focused on the heating source NBI3 with angles close to 90 degree and define 15 toroidal and 11 poloidal LOS. These enable to observe the FIDA radiation above 659.5 nm without superimposed active radiation from NBI. No beam emission with large Doppler shifts is observed.

To measure the FIDA radiation from the various LOS, a high photon throughput Czerny-Turner spectrometer with a good spectral resolution (0.16 nm) has been built. It uses a low noise EM-CCD camera to simultaneously measure the light from 15 LOS and has been equipped with an interference filter that attenuates the intense passive D-alpha radiation from the plasma edge. A sophisticated wavelength and intensity calibration is applied and the level of noise contained in the spectra is determined by the camera's readout noise and by using a conversion factor from measured counts to photons.

Several passive contributions have been identified in the spectra that limit (if present) the spectral range in which the FIDA radiation can be analyzed. The passive D-alpha radiation at 656.1 nm is about 100 times more intense than the FIDA radiation and can show, in the spectra from the poloidal LOS, broad spectral wings caused by Stark broadening. In particular in the presence of high electron densities that appear in the divertor region in the transient phases during edge-instabilities, the Stark broadening needs to be taken into account for analysis of the FIDA spectra. In addition, D_2 molecular lines have been found to populate the FIDA spectra when using D_2-fueling valves close to the LOS and passive FIDA radiation is observed when large neutral densities are present at the plasma edge.

Radial fast-ion density profiles are obtained from the radially distributed toroidal and poloidal LOS. By integrating the spectra in wavelength ranges without significant contributions from passive line radiation and by accounting for Bremsstrahlung with a constant offset, the shape of radial FIDA intensity profiles can be analyzed continuously. Depending on the integrated spectral range, different regions of the fast-ion velocity space are accessible. The toroidal LOS observe mainly co-rotating fast-ions and the poloidal ones also cover the velocity space of trapped particles.

Chapter 6

Fast-ion transport studies in the absence of strong MHD activity

The interaction of fast-ions with the thermalized plasma is an active field of investigations in plasma physics. Along their orbits through the plasma, fast-ions transfer energy and momentum to the background ions and electrons and can contribute to the plasma current. In case of an MHD-quiescent background plasma, two mechanisms have to be considered in order to estimate the phase space distribution of fast-ions: the slowing down of fast-ions and the radial fast-ion transport. While the slowing down is dominated by Coulomb collisions with electrons and ions, the radial fast-ion transport can be described by a collisional, i.e. neo-classical, diffusion plus a possible anomalous diffusion that might be caused by small scale turbulence (discussed in chapter 2).

In AUG, the fast-ion current drive efficiency has been studied previously in MHD quiescent plasmas during 5 MW of on- and off-axis NBI heating [30]. Thereby, the analysis of the current profiles by MSE measurements revealed that in particular during a low triangular plasma shape, the experimentally inferred current profiles during off-axis NBI do not significantly differ from those measured during on-axis NBI. TRANSP simulations, however, indicate that the current driven by a neo-classical, off-axis fast-ion slowing down distribution should have a measurable effect on the current profiles. One possibility to explain this discrepancy between the measurement and the simulation is that micro-turbulence redistributes the off-axis injected fast-ions and thereby broadens the current drive profiles. This assumption is supported by FIDA experiments performed at DIIID, [29], where an anomalous fast-ion diffusion caused by micro-turbulence is assumed because the measured FIDA radiances are significantly lower than predictions from neo-classical simulations.

The new FIDA diagnostic at AUG now enables to address the possible anomalous fast-ion transport in MHD-quiescent discharges by measuring the fast-ion distribution function with a high radial resolution and a good signal to noise ratio. By comparing measured and simulated FIDA spectra and radial intensity profiles with neo-classical simulations, the radial fast-ion transport is investigated under different plasma conditions. In addition, this chapter gives comparisons to simulated distribution functions in which a predefined and constant anomalous fast-ion diffusion is assumed.

First, FIDA measurements with the poloidal and toroidal LOS during 2.5 MW of on-axis NBI are presented and compared to the simulations from F90FIDASIM and TRANSP. Then, investigations of the fast-ion confinement during 5 MW of on- and off-axis NBI are illustrated in experiments similar to those reported in [30]. Two discharges with different ion-collisionalities are presented, whereby the second discharge permits, due to a better signal

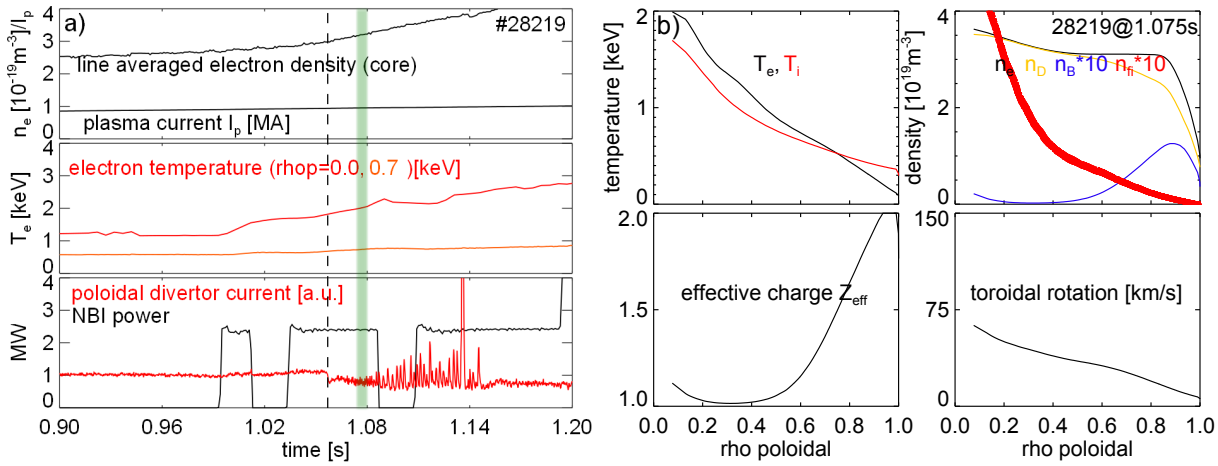

Figure 6.1: a) Time traces of discharge #28219 showing the evolution of the electron density, the plasma current, the electron temperature, the poloidal current measured at the inner divertor and the power of NBI3. The dashed line illustrates the L-H transition and the time range investigated by the FIDA measurement is indicated in green. b) Kinetic profiles at 1.075 s that are used in F90FIDASIM and TRANSP. In the upper right plot, the different densities are plotted. In black, the electron density from the IDA analysis is shown. The boron density, derived from the effective charge profile and the electron density has been multiplied by ten and is drawn in blue. The D-ion density is shown in yellow and the fast-ion density that corresponds to all possible pitches and energies of a TRANSP predicted neo-classical slowing down distribution and that has been multiplied by ten is illustrated in red.

to noise ratio, the study of different energy ranges of fast-ions. Finally, a short summary and outlook are given.

6.1 Toroidal and poloidal FIDA measurements during 2.5 MW of NBI

The confinement of fast-ions injected by the 2.5 MW heating source NBI3 has been studied in the early phase of discharge #28219 that showed a rather low density and high temperature. This ensures a large population of fast-ions and consequently a good signal to noise ratio of the FIDA measurement. A few representative time-traces of the discharge are presented in figure 6.1a and profiles for one time point are illustrated in figure 6.1b. The NBI heating from NBI3 has been switched on at about 1 s while the plasma current was still ramped up. The plasma density was in the range of $2 - 4 \times 10^{19}/\mathrm{m}^3$ and the electron temperature in the plasma center was about 2 keV. The transition from L to H mode appeared at ~ 1.06 s which can be seen by a drop of a thermo-current, measured at the divertor target plates that represents the temperature difference between the inner and outer divertor. After the L-H transition, the plasma does not show strong MHD-activity until the first significant (type 1) ELM appears at 1.13s. This opens a time window of several tens of milliseconds before the ELM crashes perturb the poloidal FIDA spectra[1].

During discharge #28219, 8 toroidal and 7 poloidal LOS were connected to the FIDA spectrometer. The spectra observed by a central toroidal and a central poloidal LOS are shown in figure 6.2 for four successive time points around 1.075 s. The spectra only consist of the active contributions because the background radiation without NBI3, measured at $\sim$ 1.1s, has been subtracted.

[1]The effect of ELM crashes on the poloidal spectra is discussed in chapter 5.

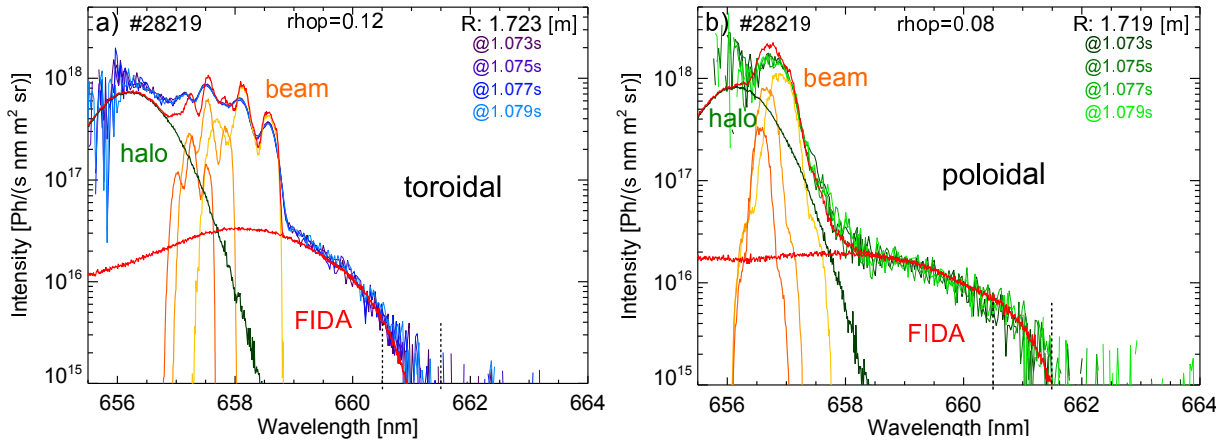

Figure 6.2: a) Active spectra of a central, toroidal (a) and poloidal (b) channel compared to the neo-classical simulation from TRANSP and F90FIDASIM. The halo radiation is shown in dark green, the beam emission in orange and the FIDA radiation in red.

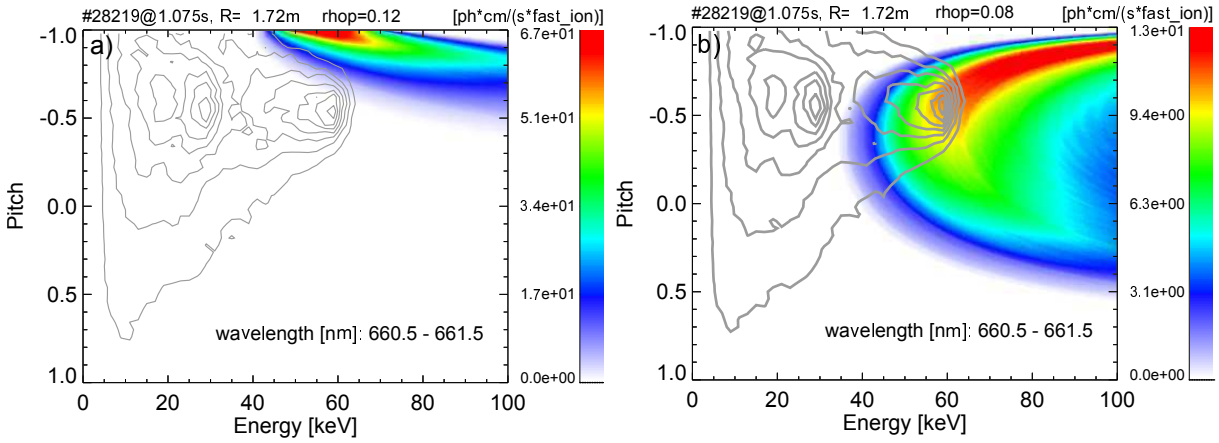

Figure 6.3: Toroidal (a) and poloidal (b) weight function for wavelength between 660.5 nm and 661.5 nm compared to the velocity space distribution of fast-ions injected by NBI3 (gray contour lines), as predicted by TRANSP.

It is noteworthy that the measured FIDA radiation has different spectral shapes in the toroidal (blue) and poloidal (green) spectra because different regions of the velocity space are accessed. As an example, the poloidal spectra show a higher level of FIDA radiation between 660.5 nm and 661.5 nm than the toroidal ones. While the toroidal LOS observe above 660.5 nm a region of the velocity space where only few fast-ions from NBI3 are present, the region in the velocity space observed by the poloidal LOS overlaps well with the distribution function from NBI3. This can be seen in figures 6.3a and 6.3b where a toroidal and a poloidal weight function are plotted together with a TRANSP predicted fast-ion velocity distribution from NBI3. Clearly, the weight function of the poloidal LOS well overlaps with the fast-ion velocity space from NBI3, shown with gray contour lines, while the toroidal one does not.

In addition to the measurement, figure 6.2a and 6.2b show simulated spectra from F90-FIDASIM that were calculated with the kinetic plasma profiles illustrated in figure 6.1b. As can be seen, the simulated beam emission (orange) and the halo emission (green), situated between 656 nm and 659 nm, are in good agreement with the measurement. This proves that the neutrals present along the beam line have been reliably modeled and that the input kinetic plasma profiles were consistently measured by the diagnostics described in chapter 3. This consistency check is necessary to proceed investigating the fast-ion transport with the FIDA measurement; otherwise, possible differences between the simulated and the measured

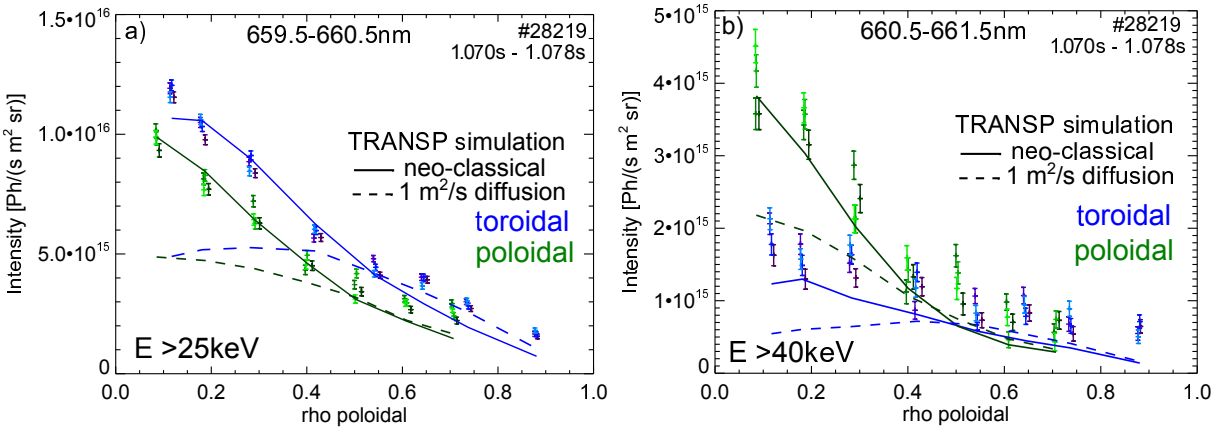

Figure 6.4: a) Measured and simulated radial FIDA intensity profiles of 8 toroidal (blue) and 7 poloidal (green) LOS for fast-ion energies above 25 keV. The solid lines show simulated profiles that correspond to a neo-classical fast-ion distribution function from TRANSP. The dashed lines correspond to an anomalous fast-ion transport of $1m^2/s$. b) Measured and simulated profiles for fast-ion energies above 40 keV.

level of the FIDA radiation could be unrelated to the fast-ion distribution function.

The red curves in figures 6.2a and 6.2b represent the F90FIDASIM simulations of the FIDA spectra, where the input distribution function has been predicted by TRANSP, assuming no anomalous transport. The measured intensities are well reproduced by the TRANSP simulation for both, the toroidal and the poloidal spectra. Moreover, the shapes of the simulated radiation follow closely those of the measurements, suggesting that the TRANSP predicted fast-ion velocity space is valid.

To illustrate that the neo-classical simulation describes well also the spectra from the other toroidal and poloidal channels of the FIDA diagnostic, figure 6.4a and 6.4b show toroidal (blue) and poloidal (green) radial profiles as a function of the radius, i.e. the normalized poloidal flux. Two different integration ranges have been chosen to access different fast-ion energies. Figure 6.4a corresponds to an integration range of 659.5-660.5 nm and hence monitors fast-ions above 25 keV. For figure 6.4b, the toroidal and poloidal spectra have been integrated between 660.5-661.5 nm which represent, as shown by the weight functions in figures 6.3a and 6.3b, fast-ions above 40 keV. At the lower integration range, the toroidal profiles show a higher level of FIDA radiation than the poloidal ones. In contrast, the poloidal profiles plotted in figure 6.4b clearly show a larger amount of FIDA radiation than the toroidal ones which is, as expected, due to the better overlap of the poloidal weight function with the velocity space of NBI3 between 660.5-661.5 nm (see figure 6.3b).

In addition to the measurements, the results from a neo-classical simulation (solid lines) and from a simulation assuming $1m^2/s$ of anomalous transport (dashed lines) are illustrated. As can be seen, the neo-classical simulation describes the poloidal and toroidal profiles for both integration ranges well. Not only the intensities but also the shapes of the measured and simulated profiles are in agreement. In contrast, assuming a high fast-ion diffusion yields results which are outside the error-bars of the measurement. This shows that in the initial phase of discharge #28219, the fast-ion velocity space and the absolute fast-ion density are well described by the neo-classical assumption. If there is an anomalous contribution to the fast-ion transport, it must be well below $1m^2/s$ in absence of significant MHD activity. This consequently suggests that, under the investigated plasma conditions, small scale turbulence has no significant impact on the fast-ion confinement.

6.2 FIDA measurements during 5 MW of on- and off-axis NBI

Several experiments have been conducted to study the fast-ion transport during 5 MW of on- and off-axis NBI heating in order to investigate a possible anomalous broadening of the fast-ion distribution function with the FIDA diagnostic, as suggested by [30]. For the discharges, conditions similar to the previous current drive experiments were reproduced, such as a toroidal magnetic field of -2.5 T, a plasma current of 800 kA and a low triangular poloidal plasma shape. In order to improve the signal to noise ratio in the FIDA measurement, low plasma densities are required. For this reason, the discharges have been performed shorty after boronizations which stabilize low density plasmas. The external heating sources were applied relatively late to keep the level of MHD activity as low as possible. Also the timing of the on-and off-axis sources was similar to earlier experiments. First 5 MW of on-axis NBI from sources NBI3 and NBI8 were applied for about 2 s and then replaced by a 2 s phase of heating by the two off-axis sources NBI6 and NBI7 (5 MW). During the off-axis phase, central ECRH heating has been used to prevent impurity accumulation in the plasma center and to keep the electron temperature profile constant[2]. In addition, short pulses from NBI3 were applied to enable the FIDA measurements.

In the following, the FIDA measurements during two such discharges, #27237 and #28071, are presented which were performed with 15 toroidal LOS. The two discharges showed different densities and temperatures which permit the study of the fast-ion confinement in the presence of different collisionalities.

6.2.1 High collisionality: discharge #27237

Discharge #27237 has already been introduced in chapter 4 when validating F90FIDASIM given the good diagnostic coverage. Representative time traces of the discharge are drawn in figure 6.5a. The line averaged electron density, measured by an interferometer channel that is situated close to the plasma center, was about $7 \times 10^{19}\mathrm{m}^{-3}$ and the central electron temperature was reaching up to 3 keV. The TRANSP calculated collisionality for this discharge was about 0.52 for $\mathrm{rho_p} < 0.8$, which is, for a discharge performed to study the fast-ion confinement, relatively high. Between 3 s and 5 s, on-axis NBI has been replaced by 5 MW of off-axis NBI, by 0.5 MW of central ECRH heating and with four 50 ms pulses from NBI3 on top. No significant MHD activity was present throughout the discharge, as has been determined from magnetic measurements. However, the existence of small scale turbulence can be inferred from the gradients in the measured temperature profiles. The power balance, i.e. the balance between the temperature gradients, the density and the heat fluxes, yields heat diffusivities that are significantly higher than the neo-classical predictions. As an example, figure 6.5b shows ion-heat diffusivity profiles during on- and off-axis NBI as calculated from the power balance by TRANSP. The diffusivity ranges from $\sim 1\mathrm{m}^2/\mathrm{s}$ in the plasma core to $\sim 6\mathrm{m}^2/\mathrm{s}$ at the plasma edge. The over plotted neo-classical ion-heat diffusivity profiles from TRANSP (dashed lines) are well below. This indicates that micro turbulence is present in discharge #27237 as it determines the ion heat transport. It is interesting now to address the question whether turbulence also causes a significant transport of fast-ions that can be resolved by the FIDA diagnostic.

[2]For the analysis of fast-ion current drive by the MSE measurement, a constant electron temperature profiles is necessary because changes of the profile shape affect the radial current distribution.

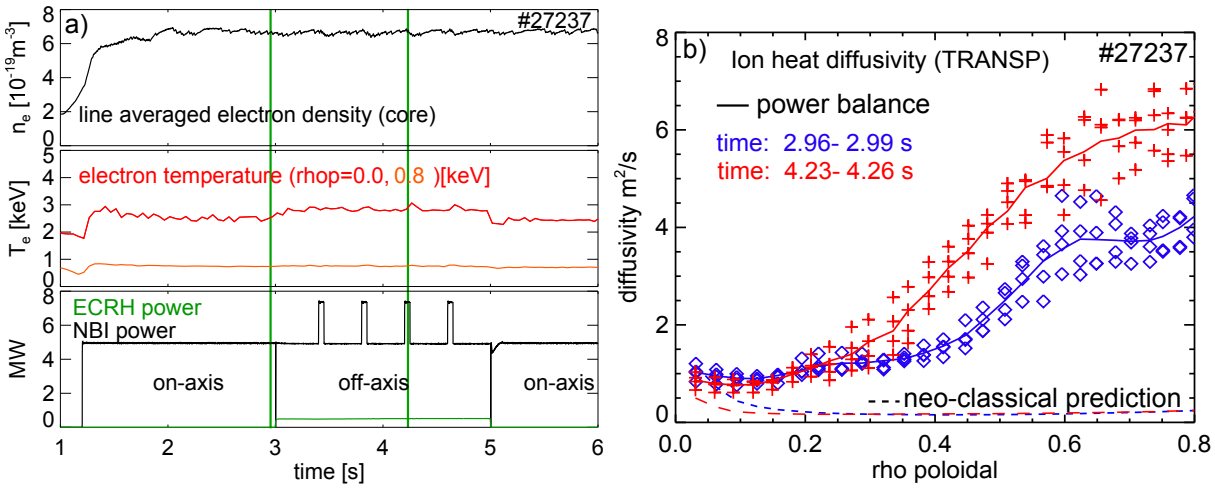

Figure 6.5: a) Time traces of discharge #27237 showing the plasma current, the plasma stored energy, the electron density and temperature and the timing of the external heating sources. The two time ranges that are investigated with the FIDA diagnostic are emphasized in green. b) Ion heat diffusivity profiles during on-axis NBI (blue) and off-axis NBI (red) by the power balance and the neo-classical prediction from TRANSP for discharge #27237.

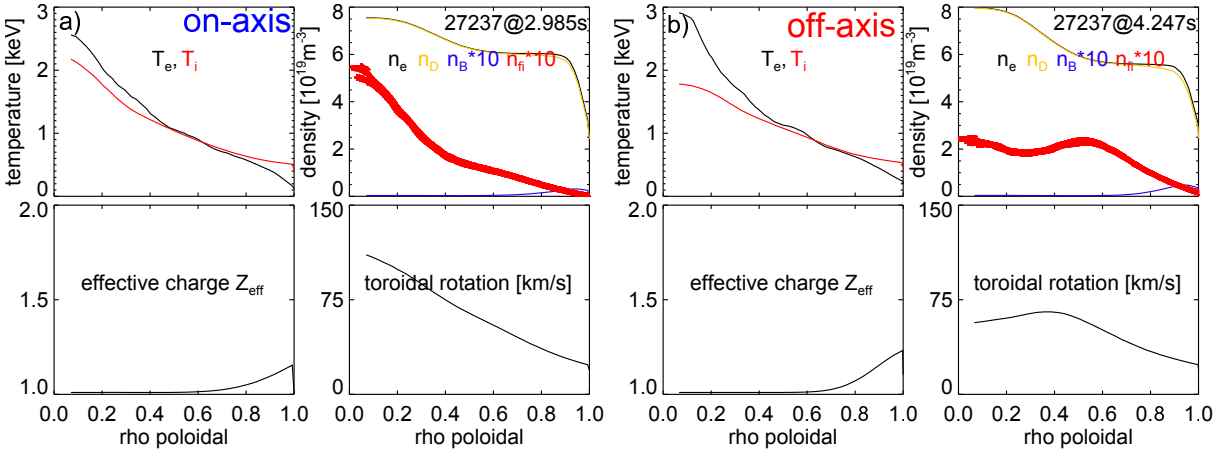

Figure 6.6: Radial profiles of the plasma parameters measured during on-axis NBI at 2.985 s (a) and during off-axis NBI at 4.247 s (b) that have been input to F90FIDASIM and TRANSP. In the upper right plots, the electron (black), D-ion (yellow), boron (blue) and the fast-ion (red) density profiles are illustrated.

Typical active FIDA spectra measured in the discharge are plotted in figures 6.7a and 6.7b. Figure 6.7a shows four successively measured spectra during 5 MW of on-axis NBI of a central channel. Figure 6.7b illustrates spectra observed during off-axis NBI heating that were measured by a LOS that intersects NBI3 close to the plasma edge. Clearly, the spectra in both figures show significant amounts of FIDA radiation between 659 nm and 662 nm which are not superimposed by strong active or passive contributions.

With the use of the kinetic input profiles shown in figures 6.6a and 6.6b, theoretical spectra have been calculated by F90FIDASIM. As shown in figure 6.7, a good agreement is found between the measured and simulated beam (orange) and halo (green) components during on- and off-axis NBI. This proves that the kinetic profiles are consistent, thus allowing the quantitative comparison between simulated and measured FIDA intensities. The simulated FIDA radiation, displayed in red in figures 6.7a and 6.7b, corresponds to a neo-classical simulation from TRANSP. It agrees very well with the measurement in both cases which indicates that, in contrast to the ion heat transport, the fast-ion transport is not affected by a significant additional diffusion. The corresponding radial FIDA intensity profiles mea-

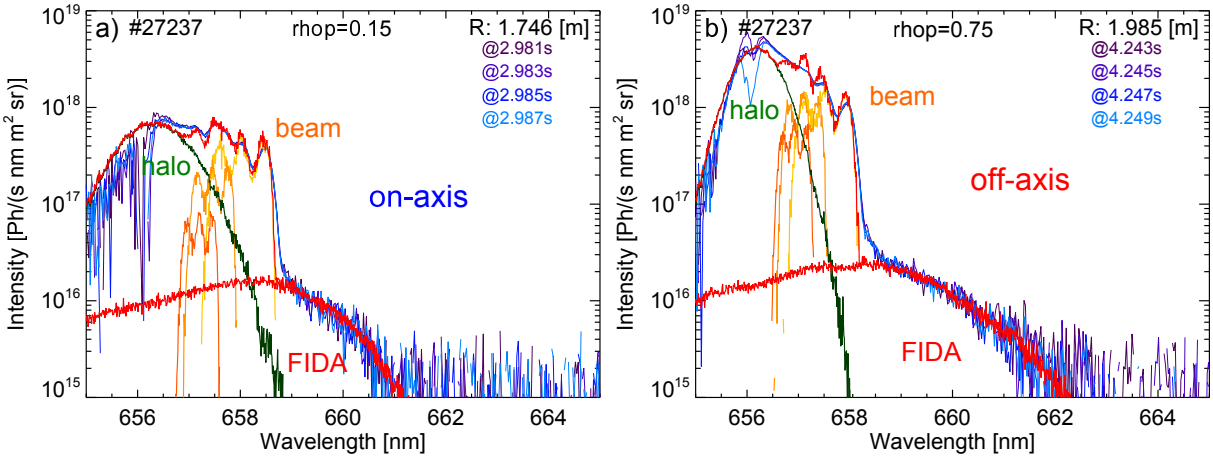

Figure 6.7: FIDA spectra observed during on-axis NBI (a) and during off-axis NBI (b). In addition to the spectra the results from F90FIDASIM are plotted. The halo emission is shown in green and the beam emission is plotted in orange. The simulated FIDA radiation, which corresponds to a neo-classical slowing down distribution from TRANSP, is drawn in red.

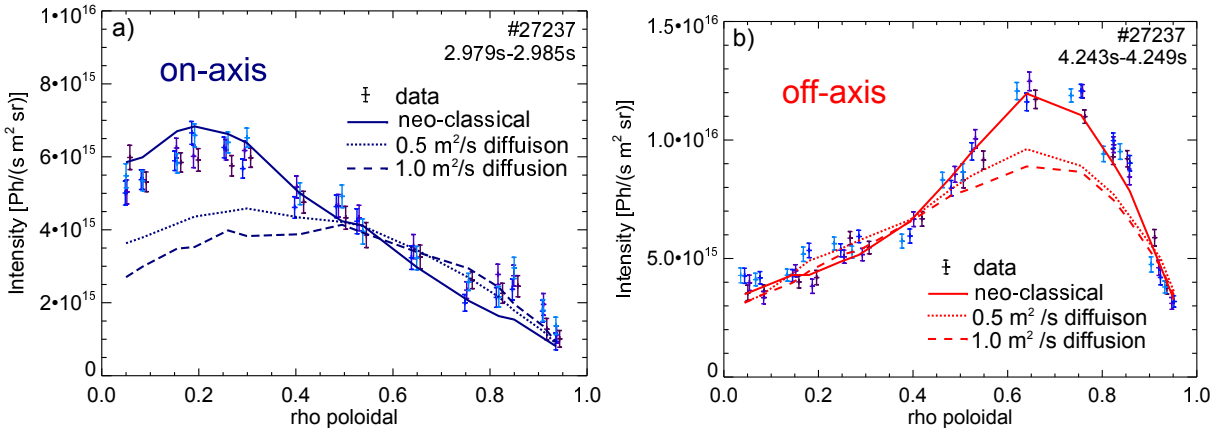

Figure 6.8: Measured and simulated radial FIDA intensity profiles during on-axis (a) and off-axis (b) heating. The profiles have been determined by integrating the simulated and measured spectra of 15 toroidal channels between 659.5 nm and 661 nm. The simulated profiles representing the neo-classical fast-ion slowing down distribution are plotted with solid lines. The predicted FIDA intensity profiles assuming a constant anomalous diffusion of $1\mathrm{m}^2/\mathrm{s}$ and $0.5\mathrm{m}^2/\mathrm{s}$ are represented by the dashed and dotted lines, respectively.

sured in discharge #27237 are displayed in figures 6.8a and 6.8b. Each figure shows four successively measured intensity profiles as a function of the normalized poloidal flux. The passive radiation, observed when NBI3 was off, has been subtracted from all cases. As the individual spectra from the 15 toroidal LOS have been integrated between 659.5 nm and 661 nm, the profiles represent fast-ions with energies above 25 keV. The radial FIDA intensity profiles measured during on-axis NBI are, as expected, peaked close to the plasma center while the ones measured during off-axis NBI show their maximum at $\mathrm{rho_p} \approx 0.7$. This position is in good agreement with the injection geometry of the off-axis NBI sources, illustrated in chapter 3.

The simulated FIDA intensity profiles that represent a neo-classical slowing down distribution from TRANSP are plotted with solid lines. As it can be seen, the shapes, as well as the absolute intensities of the measured profiles, agree very well with the simulations in both cases. Instead, the profiles associated with diffusion coefficients of $\mathrm{D_{fi}} = 1\mathrm{m}^2/\mathrm{s}$ (dashed lines in figure 6.8) and $\mathrm{D_{fi}} = 0.5\mathrm{m}^2/\mathrm{s}$ (dotted lines in 6.8) do not fit the measurements. This disagreement proves that the neo-classical slowing down distribution from TRANSP represents the experimental data very well. The anomalous fast-ion transport is consequently well

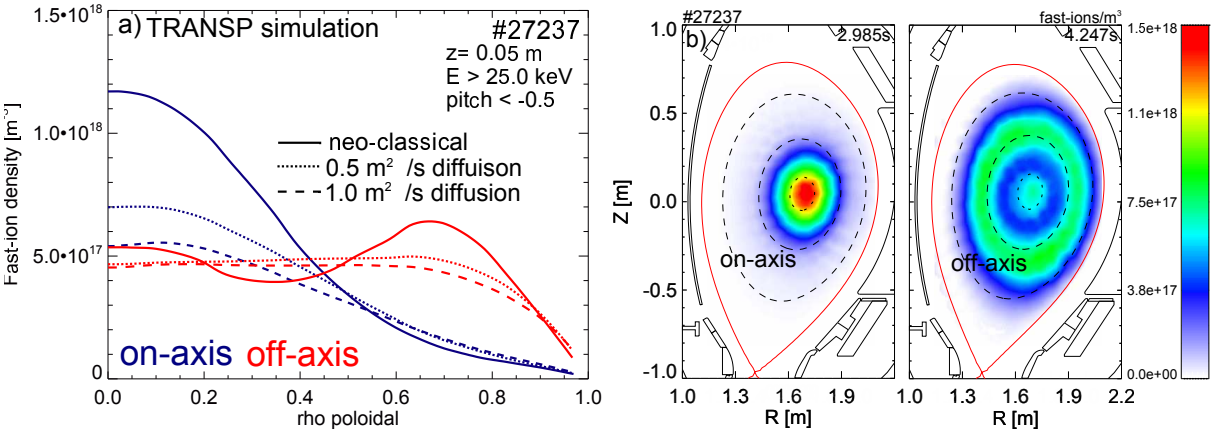

Figure 6.9: a) Radial fast-ion density profiles from TRANSP during on- and off-axis NBI heating that correspond to a neo-classical slowing down distribution and a to distribution functions assuming $1m^2/s$ and $0.5m^2/s$ of anomalous transport. b) Poloidal cross section of AUG showing the neo-classical fast-ion slowing down distribution during on- and off-axis NBI heating for fast-ions in the velocity space accessed by the velocity space of the FIDA diagnostic.

below $1m^2/s$.

Fast-ion density profiles from the applied neo-classical slowing down distribution, restricted to the velocity space observed by the toroidal LOS, are illustrated in figures 6.9a with solid lines. During on-axis NBI heating, the profiles plotted in blue have, as expected, their maximum in the plasma center where NBI3 and NBI8 deposit most of the fast-ions. The simulated neo-classical profile for the off-axis case, plotted with a red solid line, has two peaks. One peak is located at about $rho_p \approx 0.7$ and corresponds to fast-ions from NBI6 and NBI7. The other peak is situated in the plasma center and is due to fast-ions from NBI3 since a 50 ms blip of NBI3 was necessary for the FIDA analysis. This is large enough to produce a significant fast-ion population from NBI3. The measurements cannot be analyzed shortly after turning on NBI3 because the latter needs, when operated in pulses, about 30ms to reach a stable injection voltage and focus.

It should be noted that the FIDA intensity profiles plotted in figure 6.8 have a different shape than the fast-ion density profiles because they also depend on the density of neutrals present along NBI. The latter decreases towards the plasma center and imposes an additional contribution to the shape.

As a final result, the predicted neo-classical fast-ion densities from TRANSP are illustrated on a poloidal cross-section in figure 6.9b. Left, the distribution function during on-axis NBI is drawn and right, the off-axis fast-ion distribution is illustrated. These two distributions are in excellent agreement to the FIDA measurement of discharge #27237.

6.2.2 Low collisionality: discharge #28071

In order to study the fast-ion confinement in presence of a lower collisionality, discharge #28071 was performed with a reduced level of D_2 fueling during the ramp up phase and with an increased level of ECRH heating. Thereby, lower densities and higher electron temperatures were achieved yielding longer slowing down times, larger fast-ion densities and consequently a better signal to noise ratio. Time traces of discharge #28071 are displayed in figure 6.10a and the kinetic profiles during the off-axis NBI phase are shown in figure 6.10b.

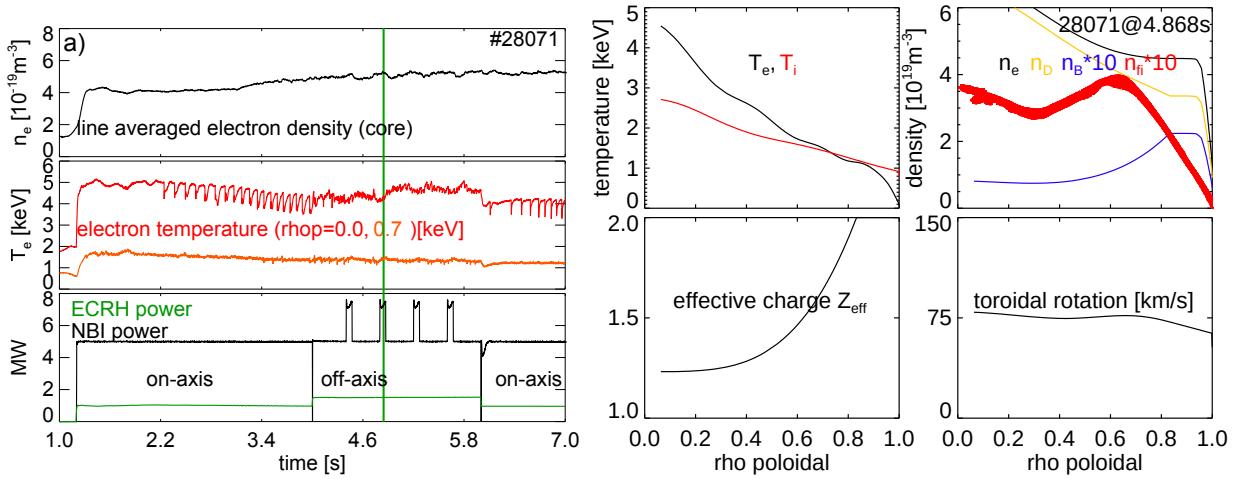

Figure 6.10: a)Time traces of discharge #28071 consisting of the line averaged electron density from interferometry, the electron temperature and the NBI heating power. b) Radial kinetic profiles during off-axis NBI.

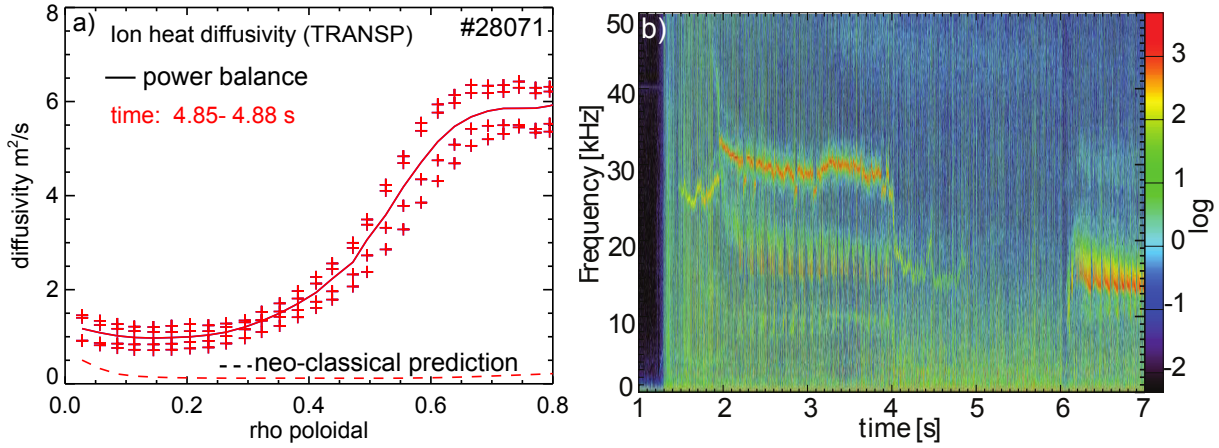

Figure 6.11: a) Ion heat diffusivity predicted by TRANSP for discharge #28071 during off-axis NBI. The neo-classical prediction is given in dashed lines. The calculation from the power balance is shown by the solid line. b) Spectrogram of a magnetic coil situated close to the plasma. During on-axis heating (1.5 s-4 s and 6 s-7 s) a magnetic island is present at ∼30 kHz and the footprint of fishbones and sawteeth becomes visible at ∼20 kHz. However, an MHD-quiescent phase is present between 4 s and 6 s.

The line averaged electron density was about $5 \times 10^{19}/\mathrm{m}^3$ and the electron temperature in the plasma core was reaching up to 6 keV. The resulting collisionality was on average 0.13 for radii inside $\mathrm{rho_p}$=0.8, as calculated by TRANSP. This is about a factor of 4 smaller than in discharge #27237. Between 4 s and 6 s, the NBI heating from the on-axis sources NBI3 and NBI8 was replaced by the off-axis sources, with 70ms blips from NBI3 on top. In addition, the central ECRH heating was increased from 1 MW to 1.5 MW to maintain a constant electron temperature profile.

A magnetic spectrogram for discharge #28071 is illustrated in figure 6.11b. The spectrogram is calculated by a Fourier analysis and it illustrates the amplitudes of magnetic fluctuations as a function of time and of frequency. As is can be seen, the MHD activity during this discharge was not negligible. In particular, a magnetic island with a frequency of about 30 kHz was present at the q=4/3 surface ($\mathrm{rho_p}$ ≈0.35) which can be seen by an increased amplitude in the spectrogram. Furthermore, the magnetic signal at about 20 kHz, as well as the fluctuation of the central electron temperatures shown in figure 6.10a, indicates that sawteeth and fishbones were present during the on-axis phases. As will be shown

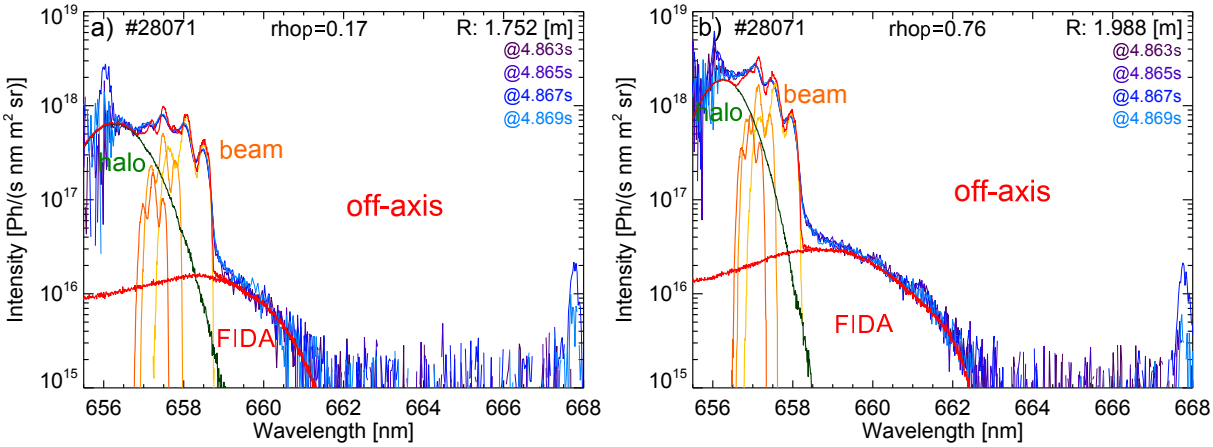

Figure 6.12: Active toroidal spectra of a central channel (a) and a channel close to the plasma edge (b) observed in discharge #28071 during off-axis NBI. In addition, the simulated FIDA emission is shown in red that represents a neo-classical fast-ion distribution function.

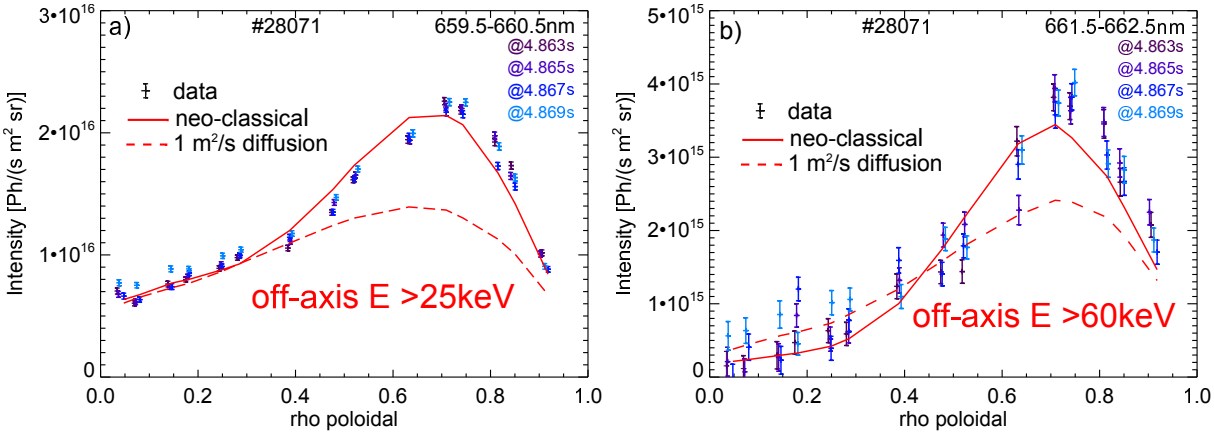

Figure 6.13: Radial FIDA intensity profiles measured during off-axis NBI heating that correspond to the integration range between 659.5 nm and 660.5 nm (a) and 661.5 nm and 662.5 nm (b). In addition the predicted profiles from F90FIDASIM and TRANSP are shown that represent a neo-classical fast-ion distribution (solid lines) and a distribution function assuming 1 m^2/s of anomalous transport (dashed lines).

in the next chapter, these modes redistribute the fast-ions and thereby modify the fast-ion distribution function. The investigation of an anomalous fast-ion transport caused by micro turbulence is not possible as it would be superimposed by that from the MHD instabilities. During the off-axis phase, however, the spectrogram and the central electron temperature show only weak fluctuations. This allows the investigation of the fast-ion transport under MHD-quiescent conditions. Here again, the presence of small scale turbulence is likely as the ion-heat diffusivity profiles from TRANSP plotted in 6.11a show values above $5m^2/s$ at the off-axis position (outside rho_p=0.5).

The FIDA measurements at two radial positions during off-axis NBI are displayed in figures 6.12a and 6.12b for four successive time points. In addition to the measured active spectra, the simulation from F90FIDASIM is overlaid. As in the previous examples, here also the simulated beam emission (orange) and halo emission (green) fit well to the data which allows the comparison between the simulated FIDA radiation and the measurement. The simulated FIDA spectra that represent a neo-classical fast-ion distribution function from TRANSP are plotted in red. Their shape and intensity are in good agreement with the measurement, which indicates that the velocity distribution of the off-axis injected fast-ions is well described by the simulation.

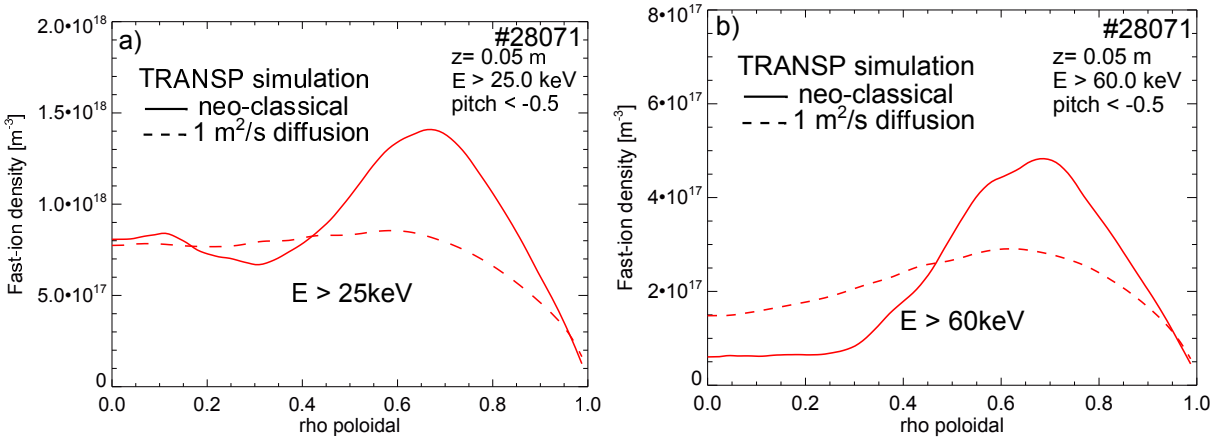

Figure 6.14: TRANSP predicted radial fast-ion density profiles for fast-ions above 25 keV (a) and fast-ions above 60 keV (b). The solid lines represent a neo-classical slowing down distribution while the dashed lines correspond to a simulation in which an anomalous fast-ion diffusion of 1 m^2/s was assumed.

The corresponding radial FIDA intensity profiles are illustrated in figure 6.13 for two different integration ranges. Figure 6.13a shows radial FIDA intensity profiles for fast-ions above 25 keV. Figure 6.13b shows profiles for an integration range between 661.5-662.5 nm, covering the velocity space above 60 keV. As the on-axis source NBI3 injects with a maximum energy of 60 keV, this wavelength range contains only radiation from fast-ions injected by the two off-axis sources (93 keV).

The neo-classical simulations are indicated in figures 6.13a and 6.13b with solid lines. They correspond to the radial fast-ion distribution functions plotted in figure 6.14a for fast-ions above 25 keV and in figure 6.14b for fast-ion above 60 keV. Clearly, the simulated and measured radial FIDA intensity profiles fit well together at both integration ranges when assuming neo-classical fast-ion diffusion only. Only at the outer parts, the simulated profiles appear to be slightly shifted relative to the measurement which is possibly explained by uncertainties in the magnetic equilibrium reconstruction.

The simulation overall fits the measured data very well. In particular, the simulation matches the measured gradients of the profiles very well, which suggests that also in this discharge the fast-ion transport is neo-classical rather than significantly anomalous. In addition, the level of FIDA radiation in figure 6.13b, which represents fast-ions above 60 keV, is close to zero in the plasma center. This is consistent with the off-axis deposition position of the 93 keV fast-ions from sources NBI6 and NBI7. The simulations assuming an anomalous transport of $1m^2/s$ well confirm the observed neo-classical fast-ion behavior. The profiles shown with the dashed lines exhibit a large discrepancy with respect to the shape and the intensity of the measured FIDA intensities. Therefore, also in the presence of a lower collisionality, a possible anomalous fast-ion diffusion must be well below $1m^2/s$.

6.3 Summary and outlook

Three different experiments with different plasma conditions have been discussed in which the fast-ion transport properties were investigated by the FIDA technique. The kinetic profiles inputted to F90FIDASIM and TRANSP were validated by comparing the simulated beam and halo radiation with the measured spectra. Thereby, the systematic uncertainties introduced by the forward modeling could be reduced.

By comparing simulated and measured spectra and radial FIDA intensity profiles, an overall good agreement between the neo-classical slowing down distributions from TRANSP and the measurement has been observed. Not only during 2.5 MW of NBI heating but also when applying 5 MW of on- and off-axis NBI in the presence of different collisionalities, the measured spectra and radial profiles fit very well the neo-classical predictions. In contrast, the simulations assuming a constant anomalous fast-ion diffusion of $1\mathrm{m}^2/\mathrm{s}$ and $0.5\mathrm{m}^2/\mathrm{s}$ are outside the statistical uncertainties of the measurements. This is good news for future fusion experiments such as ITER because, in the absence of MHD activity, a neo-classical fast-ion transport would guarantee an efficient heat transfer from fast-ions to the thermalized plasma which is essential to reach a significant fusion yield.

As the fast-ions are found to mainly remain on their deposition radii, the observed differences between the predicted and measured fast-ion current drive efficiency, as reported in [30], are unlikely to be caused by a strong anomalous fast-ion transport. This can in particular be stated as the measurements presented in this chapter with 5 MW on- and off-axis heating were performed similar to these previous experiments. The observation of a missing off-axis current drive efficiency must consequently be explained by different mechanisms, such as by a more efficient electron shielding of the positive fast-ion current than assumed in the simulations.

Here, it should be noted that the interpretation of the MSE measurement performed during the presented discharges was, unfortunately, not possible. The MSE diagnostic was not absolutely calibrated and showed a limited signal to noise ratio. However, the inversion radii of sawtooth crashes measured in discharge #28071 by the ECE diagnostic before and after using the off-axis sources indicate that the current profile is not significantly changed: The position of the sawtooth inversion radii, which are situated close to the q=1 surface, are not modified[3]. This indicates that also in the new experiments, the current profiles were not significantly changed by the off-axis NBI sources which is in agreement with the missing off-axis NBI current reported in [30].

In future investigations of a possible anomalous fast-ion redistribution in the absence of MHD activity, the level of turbulence can be increased. By using larger amounts of external heating power, such as from ECRH, stronger turbulent fluctuations are expected which might then cause an observable effect on the fast-ion distribution function. In addition, it is supposed that the turbulent fast-ion transport increases with a decreasing value of the fast-ion energy divided by the electron temperature, E_{fi}/T_e [28]. This can be tested in future experiments by e.g. reducing the injection voltage of the NBI sources and by increasing the electron temperature.

In addition, radial heat deposition profiles of fast-ions can be studied by modulating the NBI sources and then analyzing the corresponding amplitudes in the electron and ion temperature fluctuation (comparable to the experiments performed by [74] where the ECRH deposition profiles were analyzed). Thereby additional information of the radial fast-ion distribution might be obtained which can then be compared to the results from the FIDA measurement. Finally, it should be noted that the MSE diagnostic is being refurbished which might, in future investigations, enable to study the evolution of the safety factor profile. Thereby, it will be possible to compare the MSE measurement to simulations using fast-ion distribution functions validated by the FIDA diagnostic.

[3]If the current profile was changed by the off-axis NBI sources, it would remain changed after turning back to on-axis heating as the current diffusion times are in the rage of several hundreds of ms. Thus, the position of the q=1 surface, and consequently the sawtooth inversion radii would be at a different position after switching back to on-axis NBI

Chapter 7

Fast-ion transport induced by sawtooth crashes

In fusion experiments, a very fast reconnection of the magnetic field lines can be observed during sawtooth crashes. As already described in chapter 2, sawtooth crashes appear periodically in the plasma center when the q=1 surface is present. They radially redistribute heat and particles across the q=1 surface. It is very difficult to diagnose the crash phase itself because the crash times are in the range of 10-100 μs and the crash has a complex 3D structure. However, the strength of the redistribution and the recovery phase after sawtooth crashes can be studied [75]. During the last decades, the impact of the sawtooth crashes on the core plasma has been extensively studied in particular with temperature, density and soft X-ray measurements. Thereby, several models could be developed that describe this phenomenon, such as the Porcelli or the Kadomtsev model [40].

The study of the effect of the sawtooth crashes on the fast-ion distribution function is very important because a strong fast-ion redistribution might limit the heating and current drive efficiency in future fusion devices. Moreover, a detailed investigation of the fast-ion redistribution during sawtooth crashes can give a better insight into the physical processes that appear during the magnetic reconnection and can even yield information on fast-ion transport properties. Therefore, much effort has been made to diagnose the fast-ion distribution function in the presence of sawtooth crashes in the last decades. Already twenty years ago, neutron measurements evidenced that a large fraction of fast-ions are expelled from the plasma center [76]. In addition, more recent investigations carried out at the TEXTOR tokamak by CTS measurement [42] indicated that the central fast-ion density can be reduced by more than 50% and that passing fast-ions are more affected by the sawtooth instability than trapped ones. This could be supported by FIDA measurements at DIIID [77] where a decreased FIDA radiation was observed after the sawtooth crashes, in particular by toroidal LOS.

However, the detailed temporal evolution of the fast-ion density profiles has not yet been studied. For the first time, this is now possible with the FIDA diagnostic at AUG and is presented in this chapter. First, FIDA measurements of the redistribution of fast-ions, injected by the 60 keV source NBI3, are presented. The strength of the fast-ion redistribution measured by the poloidal and toroidal LOS is studied. Furthermore, the phase following the sawtooth crash is investigated: The decay of the fast-ions, situated outside the q=1 surface after the crashes and their effect on the electron temperature is investigated. Finally the radial FIDA intensity profiles and approximate fast-ion densities, measured with 15 toroidal LOS that provide a good radial resolution, are compared to predictions from the Kadomtsev model.

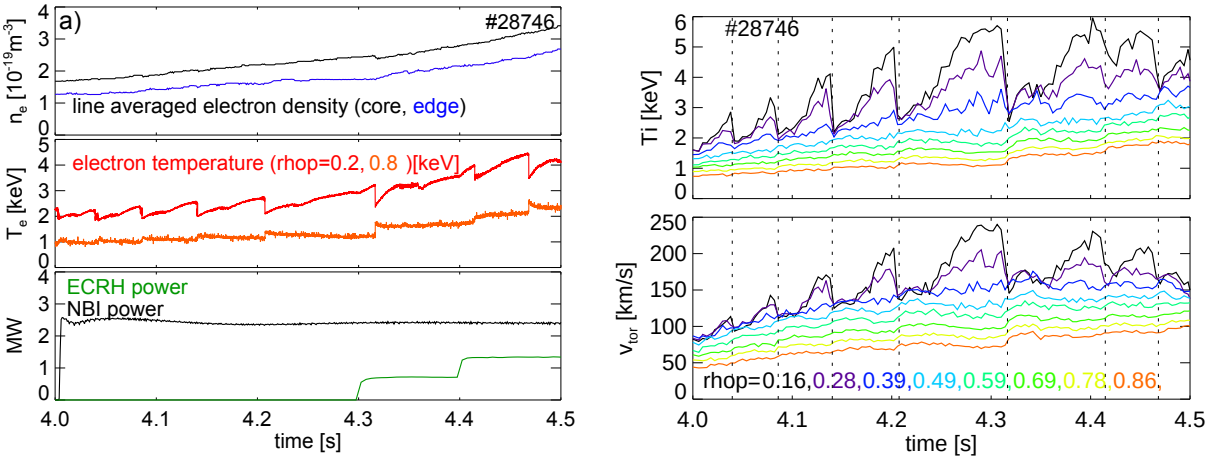

Figure 7.1: a) Time traces of discharge #28746: The measured line averaged density of a central and edge LOS are shown in the top plot. In the middle, the evolution of the electron temperature is plotted of a central channel and of a channel situated at $rho_p \approx 0.8$. The NBI and ECRH heating power is shown in the bottom plot. b) Evolution of the ion temperature and toroidal rotation measured by the CXRS diagnostic. The data is given for different radial positions, indicated by the normalized poloidal flux.

7.1 Observation of sawtooth crashes

Sawtooth crashes routinely appear in experiments at AUG when the q=1 surface is present. Discharge #28746 has been selected to present the FIDA measurements during the sawtooth crashes and to study their effect on the fast-ion distribution function because strong crashes and a low electron density were present. The discharge was operated with a toroidal magnetic field of -2.3T and a plasma current of 1 MA, while heating from the 2.5 MW source NBI3 (60 kV) was applied. Figure 7.1a shows an overview of the plasma parameters of discharge #28746. After turning on NBI heating at 4 s, a periodic variation of the central electron temperature, linked to the sawtooth crashes, is observed. The sawteeth are also visible in the central ion temperature and toroidal rotation, measured by the CXRS diagnostic (CER), as plotted in figure 7.1b. After each sawtooth crash, the ion temperature as well as the rotation is reduced up to 50%. In contrast, the electron density is not strongly affected by the instability as indicated by the core and edge line-averaged electron density, plotted in the top of figure 7.1a. This is attributed to the fact that the density profile is rather flat in the core, even before the crash.

For discharge #28746, 7 toroidal and 7 poloidal channels were connected to the FIDA spectrometer. As the density in the divertor was relatively low and did not show strong fluctuations (no significant edge-instabilities such as ELMs appeared), the FIDA measurement from both, the toroidal and the poloidal LOS, can be investigated[1].

Figures 7.2a and 7.2b show representative spectra measured in the presence of a sawtooth crash at about 4.316 s by a central toroidal and central poloidal LOS. The measured FIDA radiation between 659 nm and 662 nm is clearly lowered after the crash (yellow/orange) relative to that observed before the crash (blue/green). In contrast, the FIDA spectra illustrated in figures 7.2c and 7.2d evidence an increased level of FIDA radiation after the crash. These correspond to two channels which intersect NBI3 outside the q=1 surface at R≈2 m. (The plasma center is situated at 1.69 m and the separatrix for z=0 is at 2.15 m.)

The beam and halo radiation, observed below 659 nm, does not significantly vary which

[1]The spectra from the poloidal LOS can be affected by a variation of the edge D-alpha radiation in the transient phase during ELMs.

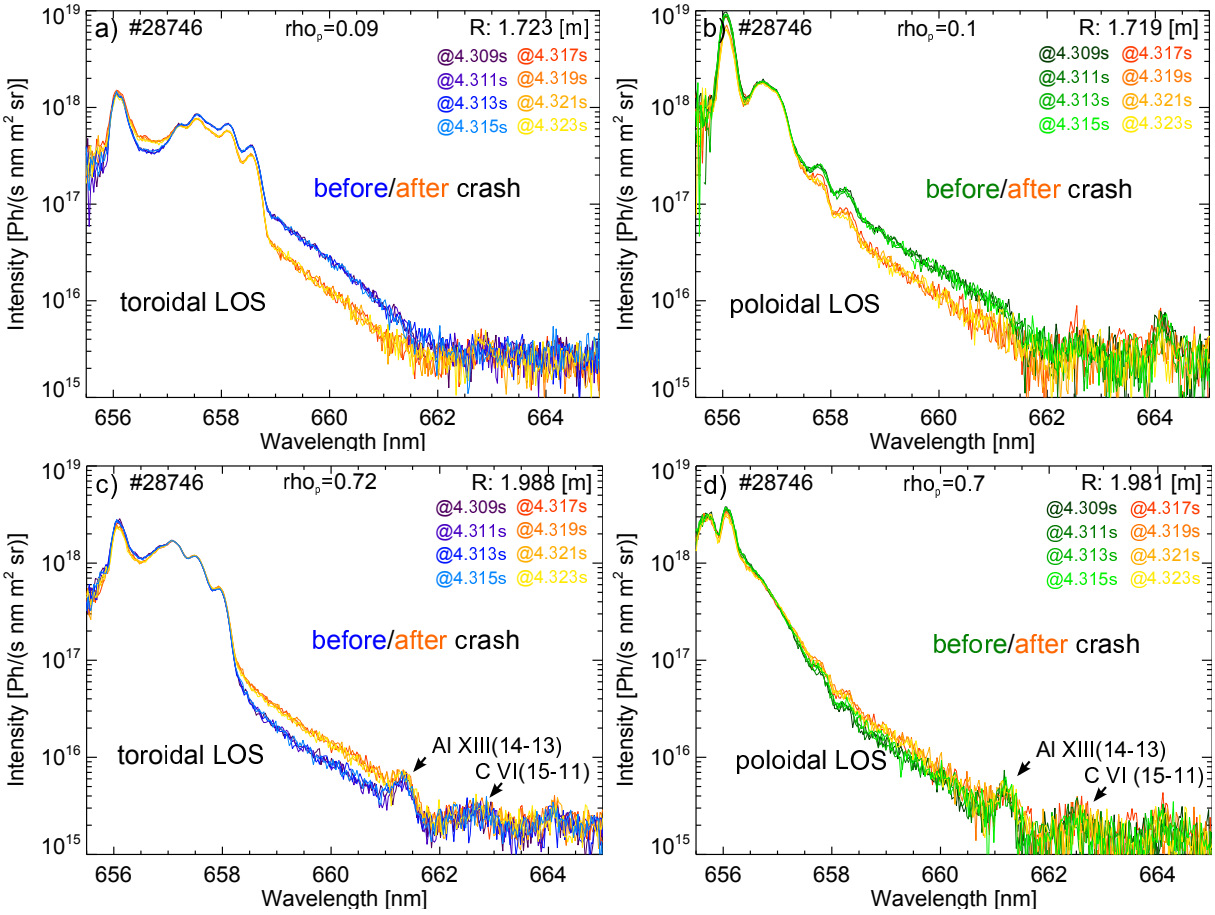

Figure 7.2: Measured FIDA spectra from a central toroidal LOS (a) and poloidal LOS (b) and from a toroidal and poloidal LOS situated outside the q=1 surface (c+d). In blue/green the spectra measured before the crash are shown. The spectra measured after the crash are illustrated in yellow/orange. The FIDA radiation from the central LOS between 659 nm and 662 nm is significantly lower after the crash while that of the LOS at rho_p ~0.7 is increased. Above 661 nm, impurity lines are present that restrict the wavelength range in which the FIDA radiation can be analyzed.

indicates that the density of neutrals along NBI3 does not strongly change. This is in agreement with the constant electron density because the attenuation of NBI and the generation of halo neutrals, as well as the local thermal equilibrium, strongly depend on the plasma density. Only in the spectra from the central toroidal LOS a change of the radiation is visible. Here, the shape of the halo radiation changes because the sawtooth induced drop of the central ion temperature and toroidal plasma rotation reduces the Doppler shift and spectral width of the halo emission line. In addition, it should be noted that the toroidal and poloidal spectra at R≈2 m measure two impurity line emissions at 661.2 nm and 662.4 nm which originate most likely from aluminum and carbon. As these two contributions are present, the analysis of the FIDA radiation is limited to wavelengths below 661.0 nm (30 keV).

The radial FIDA intensity profiles of the poloidal and toroidal LOS are illustrated in figures 7.3a and 7.3b as a function of time. The profiles represent fast-ions above 30 keV because the spectra of the toroidal and poloidal LOS have been integrated between 660 nm and 661 nm whereby the background radiation has been modeled with the horizontal line approximation discussed in chapter 5. The radial change of the radiation before and after the sawtooth crashes is clearly visible and a good agreement between the temporal behavior of the FIDA radiation and the evolution of the electron and ion temperatures, plotted in figure 7.1, is observed. Moreover, the radial change of the FIDA intensity profiles indicates

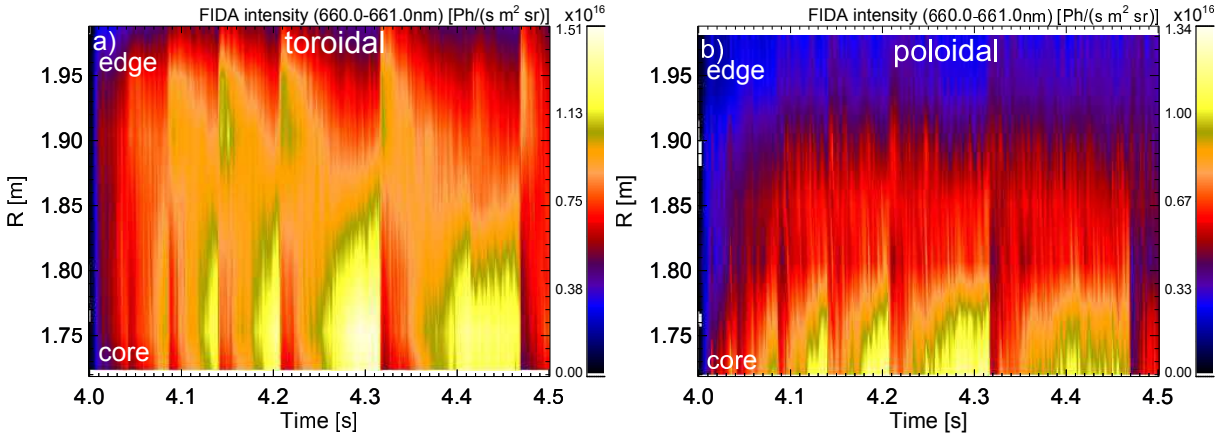

Figure 7.3: Measured radial FIDA intensity profiles as a function of time for the toroidal LOS (a) and the poloidal LOS (b). The plasma center was at a radius of 1.69 m and the separatrix at z=0 was situated at 2.15 m.

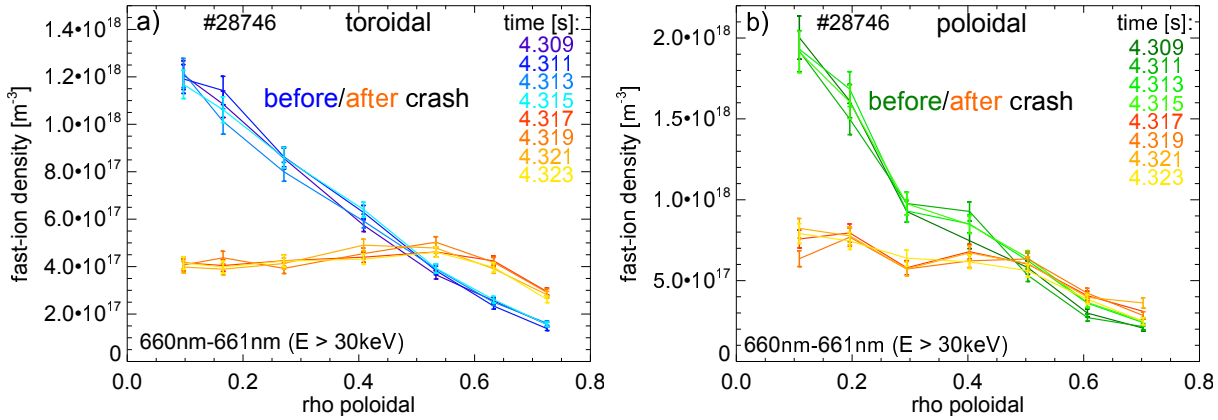

Figure 7.4: Approximate fast-ion density profiles of the toroidal (a) and the poloidal (b) LOS before (blue/green) and after (yellow/orange) a sawtooth crash.

that the sawtooth crashes radially redistribute fast-ions.

However, to quantitatively interpret the FIDA radiation, the density of neutrals present along the NBI line must be determined. Therefore, approximate fast-ion densities have been calculated from the measurement by using weight functions. The weight functions account for possible variations of the kinetic plasma profiles and consequently consider changes of the density of beam and halo neutrals. As described in chapter 4, the weight functions enable the calculation of synthetic FIDA radiances by folding them with predicted fast-ion distribution functions from TRANSP. In addition, they can also be used to calculate conversion factors from the measured FIDA radiances to approximate fast-ion densities by folding them with a normalized fast-ion distribution function. However, it should be noted that the conversion factors are based on the assumption that a given velocity space distribution of fast-ions is present and does not change. A redistribution in the fast-ion velocity space induced by the sawtooth crashes would hence falsely result in a change of the approximate fast-ion densities.

The calculated approximate fast-ion density profiles, which correspond to the sawtooth crash at 4.316s, are plotted in figure 7.4a for the toroidal LOS and in figure 7.4b for the poloidal LOS. The applied conversion factors have been calculated for every time point and radial position by calculating the specific weight functions and by applying a TRANSP predicted fast-ion velocity space.

As can be seen, both, the toroidal LOS and poloidal LOS show a drop of the fast-ion

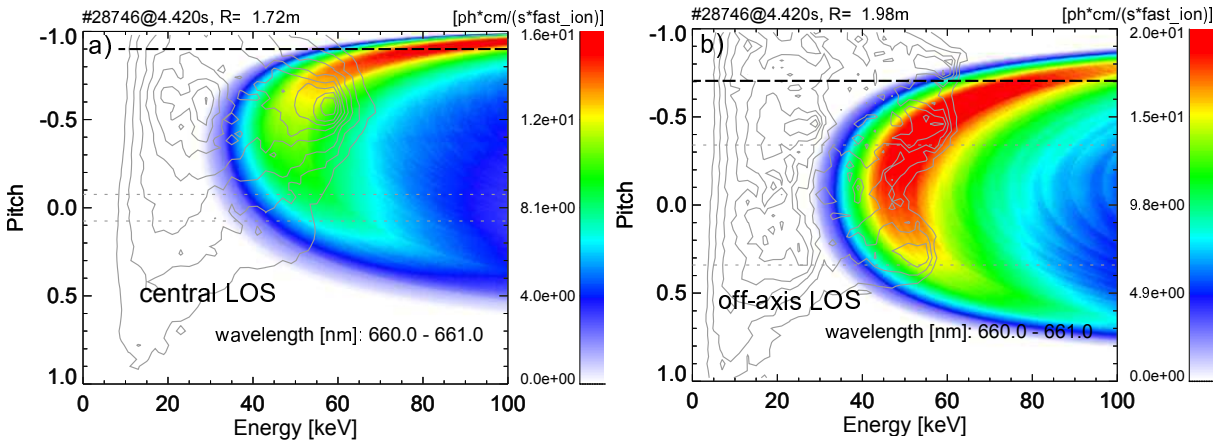

Figure 7.5: Fast-ion velocity space observed by a central (a) and off-axis (b) poloidal LOS. The black, dashed lines illustrate the boundary up to which 60 keV fast-ions can be observed by the LOS. In addition, the velocity space of fast-ions predicted by TRANSP for discharge #28746 is shown with gray contour lines.

density by about 50% which becomes flat in the center, while the LOS futher out show an increased fast-ion density. This clearly indicates that the sawtooth crashes radially redistribute fast-ions and also suggests that the assumption of a unchanged velocity space, made when computing the approximate fast-ion density profiles, is valid. If the fast-ions in the center would only be redistributed in the velocity space, they would not appear off-axis.

Interestingly, the amplitudes of the redistribution measured at $\mathrm{rho_p} \approx 0.6$ differ between the toroidal and poloidal observations. The toroidal LOS exhibit an increase of approximately 40%, while the increase observed by the poloidal ones only reaches 10%. This can be explained if dominantly passing fast-ions were affected by the sawtooth instablity. In the center, the two viewing geometries show a similar drop of the fast-ion densities because the weight function of the central poloidal LOS cover, as the toroidal ones mainly do, also passing fast-ions with pitches above -0.9 (see figure 7.5a). However, the poloidal LOS at the larger radii do not observe these ions. As illustrated in figure 7.5b, the LOS at R≈2m is only sensitive to fast-ions with pitches larger than -0.7, i.e. angles to the magnetic field lines smaller than 45° because the LOS is more perpendicular to the magnetic field lines. Hence, the redistribution of fast-ions with pitches below -0.7 would be observed by the central poloidal LOS while the LOS further out would not measure these redistributed fast-ions.

This explanation is in agreement with the already mentioned observations by CTS measurements at TEXTOR [42] and by the FIDA measurement at DIII-D [77] that also report an anisotropy in the velocity space of ejected fast-ions. Another explanation of the measurement would be that the fast-ions with larger gyro radii, i.e. those observed by the poloidal LOS, are further redistributed or even ejected from the plasma and do consequently not appear in the poloidal measurement at $\mathrm{rho_p} \approx 0.6$. However, this is rather unlikely as fast-ion loss detectors (FILD) at AUG, which are sensitive to trapped fast-ions, do typically not observe fast-ion losses in the presence of sawtooth crashes. Thus, no definitive conclusion can be drawn from the measurement but the first hypothesis is very likely. For further investigations, a tomographic reconstruction of the fast-ion velocity space with multiple viewing directions would be necessary to analyze the velocity space-dependent effects more in detail.

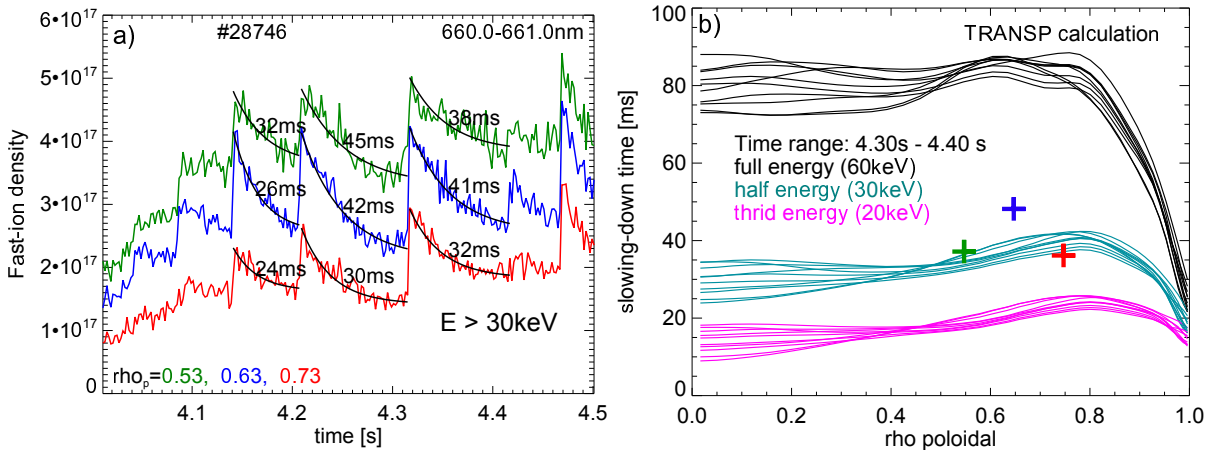

Figure 7.6: a) Temporal evolution of the approximated density of fast-ions above 30 keV, measured by three LOS that intersect NBI3 outside the q=1 surface. The decay of the increased fast-ion density, present after the crashes, is fitted by an exponential function. b) TRANSP predicted slowing down times of 60 keV, 30 keV and 20 keV fast-ions. The crosses illustrate the experimentally determined decay times between 4.3 s and 4.4 s that are shown in in a).

7.2 Investigation of the fast-ion transport after sawtooth crashes

The fast-ion transport properties can be investigated by analyzing the decay of the fast-ion distribution present outside the q=1 surface after the sawtooth crashes. Figure 7.6a shows the temporal evolution of approximated fast-ion densities that were calculated with the method described above using weight functions. The data from three different toroidal LOS is plotted that represent fast-ions above 30 keV since the FIDA spectra have been integrated between 660 nm and 661 nm. In addition to the measurement, fits to the data are shown in black that correspond to an exponential function defined by:

$$F(t) = C - A\left(1 - \exp\left(-\frac{t_s - t}{\tau}\right)\right) \tag{7.1}$$

Here, C is the fast-ion density right after a given sawtooth crash, A is the amplitude of the change of the fast-ion density, t_s the onset-time of a given crash and τ is the decay time. The function has been fitted to the data whereby C and t_s were predefined by the maximum of the fast-ion density right after the crash and by the crash time observed in the electron temperature measurement.

Next to the fitted lines, the corresponding decay times are printed which range from 24ms to 45ms. In addition, figure 7.6b shows slowing down times from TRANSP for the time range between 4.3s-4.4s and for fast-ions with 20 keV, 30 keV and 60 keV. As can be seen, the experimentally derived decay times, indicated with crosses, well match the predicted slowing down times of 30 keV fast-ions. This is a very good agreement because the approximate fast-ion densities also correspond to fast-ions with mainly 30 keV. By integrating the FIDA spectra between 660 nm and 661 nm, fast-ions above 30keV are monitored whereby the toroidal weight functions, such as shown in chapter 5, are most sensitive to the low energies, i.e. 30 keV.

The good agreement between the measurement and the simulated slowing down times indicates that the fast-ions remain at the radial locations where they have been placed after the sawtooth crash. A strong anomalous fast-ion diffusion would, as suggested by simula-

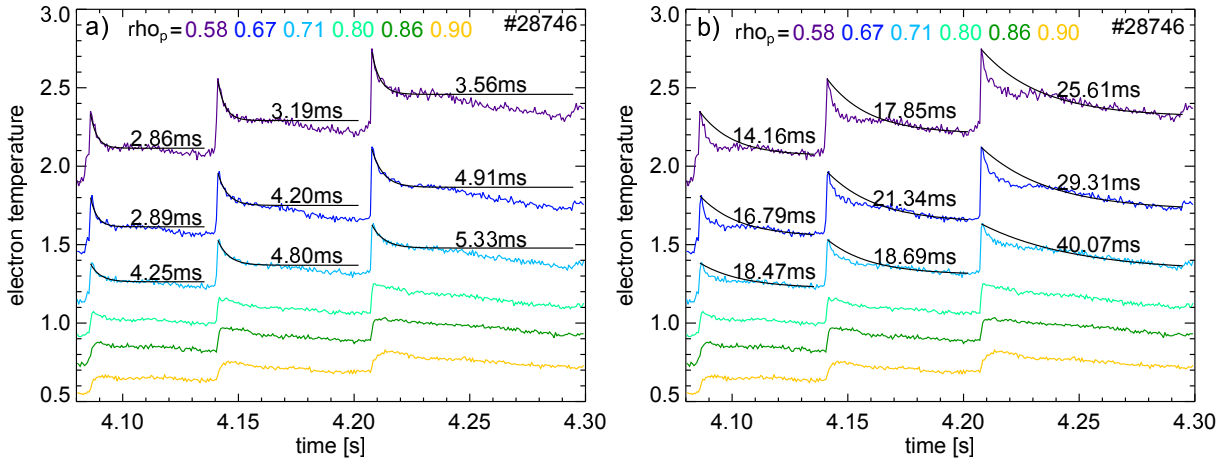

Figure 7.7: Evolution of the off-axis electron temperatures in the presence of sawtooth crashes which are fit by an exponential decay function. In figure a, the data of the first 30ms after each crash is fitted. In b, the exponential function is fitted between 20 ms after each crash and the next one.

tions[2], reduce the decay times by more than 50%. Therefore, this measurement indicates that in the analyzed discharge the fast-ion confinement is, in between the sawtooth crashes, not affected by a strong anomalous transport.

In contrast to the relatively slow decay of the fast-ion distribution present outside the q=1 surface after the crash, the behavior of the electron temperature is different. It is known for several decades that sawtooth crashes induce electron heat pulses outside the q=1 surface that diffuse towards the plasma edge. This effect has been extensively investigated in transport studies [78] by analyzing the propagation of these heat pulses through the induced T_e perturbation. Dominated by a large radial electron heat diffusion, the T_e pulses generated by the crash, diffuse outwards while their amplitude decreases and their shape becomes smoother. In AUG, the traveling time of the heat pulses lasts typically about 5 ms. This is also found in our experiments. Figure 7.7 shows the evolution of the electron temperature measured by six channels of the ECE diagnostic that are located outside the q=1 surface. The time traces, shown in blue and purple (rho_p<0.75), are fitted by the exponential function described in equation 7.1 which clearly indicates an exponential decay of the electron temperature with about 5 ms. Moreover, the channels at rho_p>0.75 do not show a peaked, but rather smooth shape which, as discussed, evidences a radial propagation of the electron heat pulse.

In addition, it seems that the T_e measurement reveals a second phase after the sawtooth crash. Once the heat pulse propagation is completed (3-5ms), the electron temperature first remains flat and then decreases with a large time constant of 20-40 ms, as shown in figure 7.7b. We attribute this time constant to the heating power provided by the fast-ions which have been redistributed by the sawtooth crash. As the fitted decay times, shown in figure 7.7b, are comparable to the fast-ion slowing down times, it yields a confirmation of the results obtained above: The fast-ions remain on their obits, rather than being displaced by an anomalous transport. Finally, it should be noted that also the evolution of the ion temperature and rotation at about rho_p=0.7, plotted in figure 7.1b, indicates this slow decay after the sawtooth crashes. It can again be attributed to the heating and torque from the redistributed fast-ions. However, in this case, the fast decay after the sawtooth crashes cannot be observed as the time resolution of the CXRS measurement is limited to 4 ms.

[2]The evolution of the fast-ion density after switching off NBI heating has been simulated by TRANSP. When assuming an anomalous transport of $1m^2/s$ in the simulation, the decay time was found to be reduced by more than 50%.

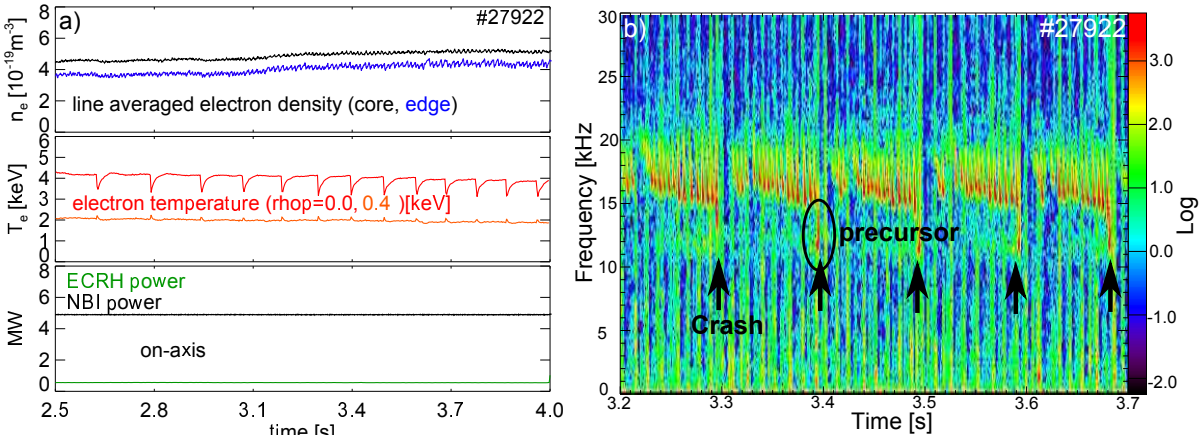

Figure 7.8: a) Time traces that characterize discharge #27922. From 2.5 seconds on, the sawtooth crashes are clearly visible in the central electron temperature. b) Spectrogram of a magnetic pick up coil that evidences the presence of sawtooth crashes and fishbones between 10 kHz and 20 kHz.

7.3 Comparisons to the Kadomtsev model

The quantitative analysis of the FIDA measurements in the presence of sawtooth crashes using forward modeling by TRANSP and F90FIDASIM is presented in this section. The TRANSP code enables to account for sawtooth crashes by the Kadomtsev model which describes, besides the redistribution of heat and thermal particles, also the redistribution of fast-ions. While the onset-times of the sawtooth instabilities need to be predefined, the amplitude of the redistribution and the mixing radius are calculated. The mixing radius is the radius up to which heat and particles are redistributed by a given crash. It is defined by the Kadomtsev model as the position where the helical magnetic flux[3], is similar to that in the plasma center. By furthermore assuming that the toroidal magnetic flux is unchanged and that the sawtooth crash results in a reconnection of the magnetic field lines inside the q=1 surface with those situated between the q=1 surface and the mixing radius, a new field line topology is determined. The redistribution of heat and particles is finally calculated by assuming that the latter are bound to the reconnected helical flux surfaces and that the pressure and the quantity of the particles are conserved.

To compare the simulation to the experimental data, discharge #27922 has been analyzed. The experiment was performed similarly to discharge #28071 (presented in the previous chapter) with a toroidal magnetic field of -2.5 T and a plasma current of 0.8 MA and with 5 MW of on-axis NBI. As large and well observable sawtooth crashes could be measured, it has been selected for this section. Figure 7.8a shows in the middle row the time traces of the electron temperature in the plasma core and at $rho_p \approx 0.7$. The sawtooth crashes are evidenced by the periodic drop of the central temperature with a frequency of about 10 Hz. In the spectrogram shown in figure 7.8b, the magnetic footprint of fishbone instabilities are visible between 15 kHz and 20 kHz. These are, approximately every 100 ms, first followed by a mode that drops to approximately 12 kHz (a sawtooth precursor) and then by a quiescent phase of 10ms present after the sawtooth crashes.

During the experiment, the 15 toroidal LOS were connected to the FIDA spectrometer which cover well the radii from the core to the edge and which are sensitive to passing fast-ions. The spectra observed with two toroidal LOS that intersect NBI3 at about 1.7 m and 1.9 m are illustrated in figures 7.9a and 7.9b. In blue, the spectra measured before a sawtooth crash are shown and in yellow/red, the spectra measured after the appearance of

[3]The helical flux is perpendicular to the helix, defined by the field lines on the q=1 surface.

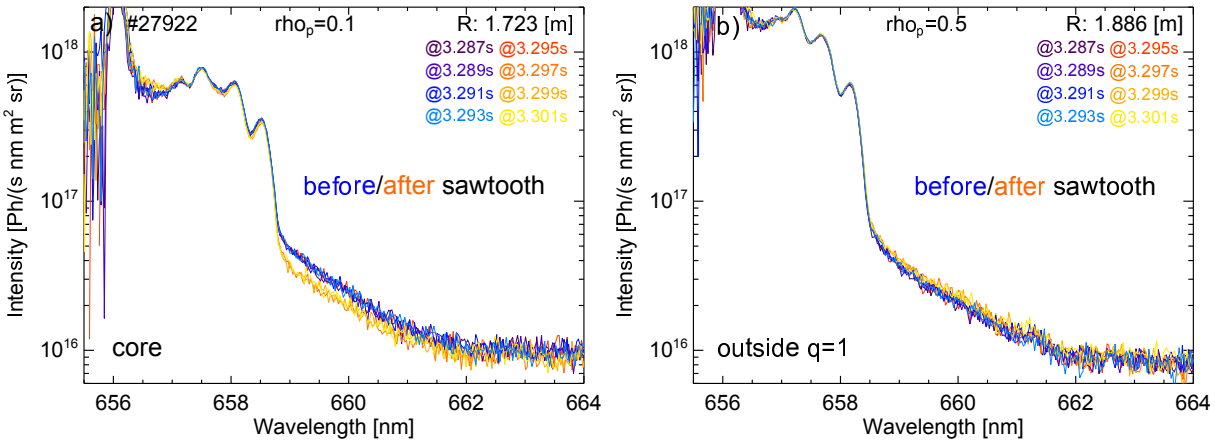

Figure 7.9: a) Measured FIDA spectra of a central toroidal LOS before and after a sawtooth crash. b) Measured spectra by a toroidal LOS situated outside the q=1 surface which show an increased FIDA radiation after the crash.

the instability are plotted. The beam and halo emission do not significantly vary during the sawtooth crash which suggests that the density of neutrals present along the line of NBI3 is constant. The FIDA contribution, however, changes. While it is decreased in the spectra of the central LOS, the channel at R≈1.9 m observes an increased emission after the sawtooth crash. Thereby, not only low wavelength shifts, but also wavelengths up to 662 nm are affected. This, in combination with the behavior of the beam and halo radiation, evidences that energetic fast-ions are redistributed by the magnetic reconnection during this discharge. It should be noted that one might think that, in particular at R≈1.9 m, the observed increase of the FIDA radiation cannot be well separated from the noise contained in the spectra. However, as will be shown in the following, the increase of the FIDA radiation at R≈1.9 m becomes much clearer by integrating the spectra over a wavelength range of 1 nm.

In figure 7.10a, measured and simulated radial FIDA intensity profiles are illustrated that correspond to passing fast-ions above 25 keV (the integration range between 659.5 nm and 660.5 nm has been chosen). Four radial profiles measured before the sawtooth instability are shown in blue and four profiles after the instability are shown in yellow/orange. The central FIDA radiation is clearly decreased while the channels at about rho$_p$ ≈0.6 observe an increased radiation. It should be noted that the radial profiles have been measured in the continuous mode whereby the passive radiation has been modeled by a horizontal line. Hence, a small offset might be present in the data which has to be regarded as an uncertainty in the data.

In addition to the measurement, three simulated profiles from F90FIDASIM are plotted that represent the predicted radial fast-ion density profiles from TRANSP, displayed in figure 7.10b. The two solid lines correspond to a time range of 8 ms before the sawtooth crash and represent a neo-classical distribution function (gray) and a fast-ion distribution function that has been calculated assuming a constant anomalous fast-ion transport of 0.15m^2/s. As can be seen, the latter fits better to the measurement for the time range before the crash. This shows that the fish-bone instabilities present in the discharge redistribute fast-ions and that they thereby flatten the central fast-ion density. The third profile, indicated by the dashed line, represents the simulated fast-ion distribution function after the sawtooth crash. It also corresponds to an anomalous diffusion of 0.15m^2/s and accounts for the sawtooth induced fast-ion redistribution from the Kadomtsev model.

The amplitude of the simulated change of the central FIDA radiation is in very good

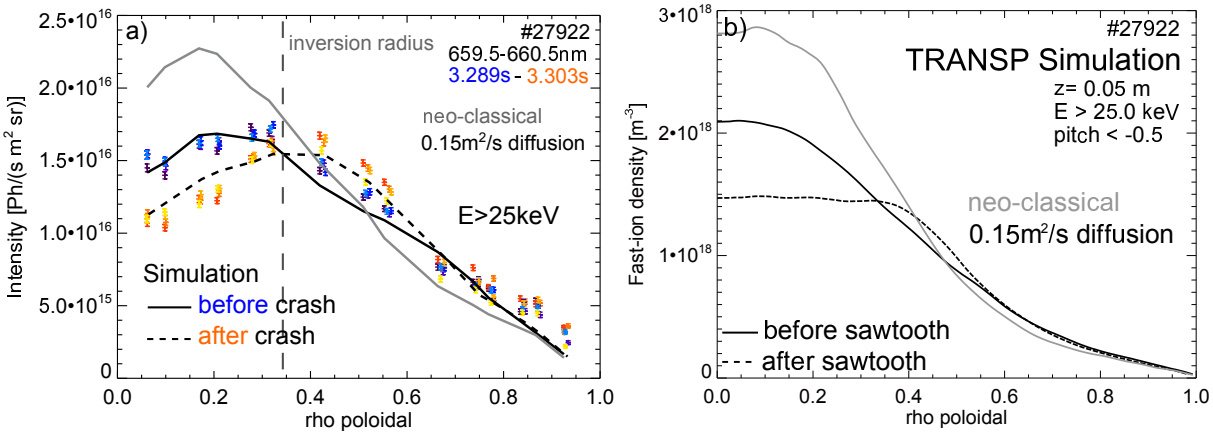

Figure 7.10: a) Measured radial FIDA intensity profiles, compared to simulated profiles before and after a sawtooth crash. b) Corresponding predicted radial fast-ion density profiles from TRANSP before and after a sawtooth crash which represent co-rotating fast-ions above 25 keV situated close to the midplane of AUG. These fast-ions can be observed by the toroidal LOS of the FIDA diagnostic.

agreement with the measurement. In addition, the predicted change of the FIDA radiation between rho_p=0.3 and rho_p=0.7 matches well the experimental data. As can be seen, not only the amplitude but also the sawtooth inversion radius, i.e. the position at which the profile before the crash is identical to the one after the crash, is well modeled. In addition, the simulated radius up to which the FIDA radiation is changed and which depends on the mixing radius, describes the experimental profiles well. This indicates that the magnetic equilibrium has been reliably calculated by the TRANSP code as it determines the position of the q=1 surface and of the mixing radius. Moreover, this shows that the assumption of the Kadomtsev model that fast-ions are bound to the magnetic field lines, is reasonable. The fast-ions are not expelled further out by effects such as from large electric fields imposed by the reconnection.

Analogue to the previous section, approximate fast-ion density profiles have been determined from the measurements by using conversion factors calculated with the weight functions. As a result, figure 7.11b shows the temporal evolution of the fast-ion densities for various channels of the FIDA diagnostic. In addition, the fast-ion energy density of passing fast-ions, predicted by TRANSP, is plotted that has been normalized to the approximate fast-ion densities. As can be seen, a good agreement between the temporal evolution from TRANSP and the measured one is obtained. This indicates that, again, the Kadomtsev model well describes the effect of sawteeth on the fast-ion distribution, not only for one single sawtooth crash but for several ones.

In addition, the behavior of the redistributed fast-ions has been investigated by using time-coherent averaging of the fast-ion density profiles which reduces the noise of the measurement. The temporal evolution of the fast-ion densities relative to the onset of sawtooth crashes is shown in figure 7.11. The measurement is compared to the normalized TRANSP predicted fast-ion energy density of passing fast-ions. As can be seen, the recovery phase of the central fast-ion density is well modeled by the simulation that assumes a small anomalous transport of $0.15 m^2/s$. Moreover, the simulated temporal evolution of the redistributed fast-ions outside the q=1 surfaces well fits to the measured one. At the positions above rho_p=0.6, no change of the fast-ion density is observed which, again, indicates that passing fast-ions follow the reconnected field lines, rather than being expelled by other mechanisms.

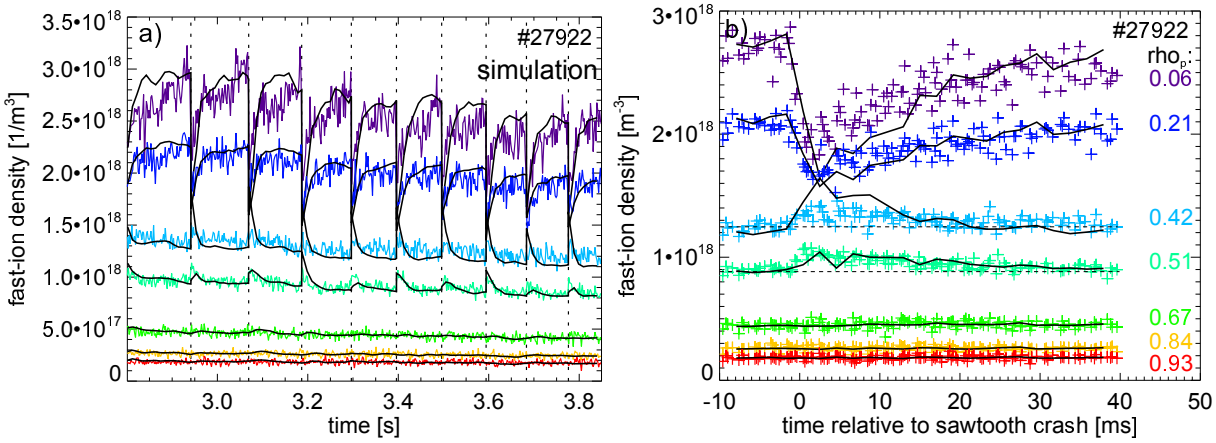

Figure 7.11: a) Temporal evolution of approximated fast-ion densities measured at different radial positions. In black, the normalized, TRANSP predicted evolution of the energy density of passing fast-ions is plotted. b) Evolution of the approximate fast-ion densities shown in a) mapped in time relative to the onset of the sawtooth crashes. The evolution of the fast-ion energy density from TRANSP is shown in black.

7.4 Summary

The fast-ion transport has been investigated in the presence of sawtooth instabilities. On the one hand, the effect of the sawtooth crash itself has been studied by the FIDA technique. A drop of the central fast-ion density of up to 50% has been observed with both, the poloidal and toroidal LOS. In contrast, a significant increase of the fast-ion density outside the q=1 surface has only been observed by the toroidal LOS which might be explained as the passing fast-ions are more effectively redistributed than the trapped ones. Furthermore, results from the Kadomtsev model, implemented in the TRANSP code, have been compared to the FIDA measurement. Thereby, a very good agreement is observed which supports the hypothesis that passing fast-ions are well bound to the magnetic field lines that reconnect during the sawtooth crashes.

On the other hand, the fast-ion transport properties have been studied by analyzing the fast-ion behavior in between sawtooth crashes. A neo-classical behavior of fast-ions has been observed by comparing the decay time of redistributed fast-ions to TRANSP predicted slowing down times. Moreover, no radial propagation of the redistributed fast-ions after the crash is observed which again implies that fast-ions remain on their orbits until they are slowed down by collisions with electrons and ions.

Finally it should be noted that in the presence of the fishbone activity in discharge #27922, an anomalous fast-ion diffusivity of $0.15\mathrm{m}^2/\mathrm{s}$ was necessary in the simulation to describe the FIDA measurement. This shows that the FIDA diagnostic is well suited to study the effect various MHD instabilities in future investigations.

Chapter 8

Summary and outlook

The fast-ion confinement is of special interest for future fusion devices because fast-ions significantly contribute to plasma heating and current drive and can, if poorly confined, even damage the first wall. Produced by fusion reactions and external heating systems such as neutral beam injection (NBI) and ion cyclotron resonance heating (ICRH), fast-ions can be redistributed by processes such as MHD instabilities or micro turbulence. The so called anomalous transport of fast-ions related to these processes must consequently be investigated and understood. A relatively new approach to study the fast-ion confinement is fast-ion D-alpha (FIDA) spectroscopy which analyzes strongly Doppler shifted Balmer alpha radiation (λ_0=656.1 nm) of neutralized fast deuterium ions. This so-called FIDA radiation can be observed locally along NBI lines thanks to the high density of neutrals that provides a significant probability to neutralize fast-ions through charge exchange reactions. The intensity of the FIDA radiation yields information on the fast-ion density and the measured wavelength shifts contain information on the fast-ion velocity distribution.

8.1 Development of forward modeling

In order to quantitatively interpret the FIDA measurement, forward modeling is needed because the FIDA radiation is a convoluted, one-dimensional, measurement of the 3D fast-ion velocity space that, in addition, depends on the charge exchange probability with neutrals. Therefore, a code called F90FIDASIM (originally FIDASIM) has been implemented for the ASDEX Upgrade tokamak and has been rewritten in Fortran90. It uses a Monte Carlo approach in a 3D simulation grid to predict synthetic FIDA spectra based on theoretical fast-ion distribution functions. The code first simulates the density and spectra of beam and halo neutrals which surround the NBI lines. Then, it calculates the neutralization probability and subsequent radiation of fast-ions.

Since the beam and halo neutrals, as well as neutralized fast-ions, only differ by their velocity distribution, the code could be rewritten in a modular way in which a new, iterative approach to model the halo neutrals was implemented. The collisional radiative model that is used to describe the attenuation, excitation and photon emission of the neutrals that transit the simulation grid has been updated with new and corrected cross-sections that account for excited states up to n=12. Moreover, an analytical solution of the differential equation defined by the collisional radiative model has been implemented that yields results which are in good agreement with those provided by the ADAS database which is an important confirmation.

In addition to the Monte Carlo approach, a new method to calculate the FIDA radiation from theoretical fast-ion distribution functions has been developed that uses 'weight functions'. The weight functions represent the probability that a fast-ion with a given velocity vector and position in the plasma undergoes a charge exchange reaction with beam or halo neutrals and that it then emits FIDA radiation which can be measured by a given line of sight (LOS) in a defined wavelength range. By multiplying various weight functions with a theoretical fast-ion distribution, artificial FIDA spectra can be calculated. Moreover, it was found that the weight functions enable the calculation of conversion factors from measured spectral radiances to approximate fast-ion densities which then permit the study of the temporal evolution of the fast-ion densities via FIDA measurements.

The geometry of the NBI lines and the LOS used in the simulation has been validated by analyzing the footprint of the radiation emitted by the neutral beam with a 2D camera. By comparing the measurement to simulations of the beam and halo emission, a good agreement was found which indicates that the vertical focus and divergence of the heating beams are well described in F90FIDASIM. Moreover, the horizontal focus and divergence of the NBI have been checked by a beam emission diagnostic that has a high spectral resolution. Thereby, again, a good agreement between the simulated beam and halo spectra and the measurement was obtained. It is remarkable and essential that the absolute intensities of the predicted beam and halo emission are in very good agreement with the measurement, which indicates than F90FIDASIM accurately models the neutrals present along the NBI lines.

In the context of a sensitivity study it was shown that the FIDA radiation, as well as the beam and halo radiation, depends strongly on the electron density. When analyzing the FIDA measurement quantitatively, this requires firstly that the electron density must be measured with small uncertainties and secondly that the beam and halo radiation is investigated in addition to the FIDA radiation. The beam and halo radiation, which is also contained in FIDA spectra, could reveal possible errors in the kinetic profiles inputted to F90FIDASIM.

8.2 Properties of the FIDA diagnostic

A new spectroscopic diagnostic has been installed at the ASDEX Upgrade tokamak that is optimized for the analysis of the FIDA radiation. Two optical heads, situated inside the vacuum vessel, define 15 toroidal and 11 poloidal radially distributed lines of sight (LOS), which are focused on a 2.5 MW heating beam (NBI3) in horizontal and vertical planes, respectively. Thereby, different parts of the fast-ion phase space are accessed. While the toroidal LOS mainly observe co-rotating fast-ions, the poloidal LOS observe fast-ions with smaller pitches (pitch=$v_{||}/v_{tot}$).

The radiation collected by the LOS is guided to a spectrometer which permits the simultaneous observation of 15 channels (LOS). The spectral range defined by the spectrometer is about 14 nm which can be monitored by an attached CCD camera with a high quantum efficiency, low readout noise and a temporal resolution of 2ms. An accurate intensity calibration using an integrating sphere is applied to the diagnostic that allows the quantitative interpretation of the measured spectra. The statistical uncertainties in data are characterized by analyzing the photon and readout noise.

Due to the geometry of the LOS and the NBI sources at ASDEX Upgrade, mainly redshifted FIDA radiation is expected. However, the FIDA radiation cannot be investigated at all possible wavelengths because additional active and passive contributions are present in

the spectra. The active radiation is only present during operation of NBI3 and consists, in addition to the FIDA radiation, of the beam and halo emission. These two intense contributions are situated below 659.5 nm where they make the analysis of the FIDA radiation impossible. Hence, only FIDA radiation with large Doppler shifts can be analyzed which corresponds to a minimum fast-ion energy of 25keV. The passive contributions in the spectra are also present without operation of NBI3 and consist of line radiation from the plasma edge and of Bremsstrahlung. The Bremsstrahlung is present in the spectra as a horizontal offset and contributes to the photon noise. The line radiation mainly consist of the very intense and un-shifted passive D-alpha radiation from the plasma edge which is attenuated in the spectrometer by an interference filter. Moreover, several line emissions have been found that appear in the spectra under certain conditions such as D_2 fueling near the LOS of the FIDA diagnostic or the appearance of edge-instabilities such as edge localized modes. However, in general, clean spectra are observed at AUG which can be explained by a low concentration of impurities in the plasmas thanks to the fully tungsten coated walls of the device.

Radial FIDA intensity profiles can be determined by integrating the spectra of the various LOS in wavelength. Thereby, the background radiation can be taken into account by two methods: First, the heating from NBI3 can be modulated which enables the subtraction of the passive components, also measured in phases when the beam is off. Second, the background radiation can be modeled with a horizontal line, allowed by the absence of significant impurity line emissions. This line represents the radiation from Bremsstrahlung and permits, in contrast to the beam-modulation technique, to study the fast-ion distribution in continuous mode with a higher time resolution.

8.3 Experimental results

In MHD-quiescent plasmas, the possible effect of micro-turbulence on the fast-ion transport has been investigated under different experimental conditions. During phases with 2.5 MW of on-axis NBI, the measurements from the toroidal and poloidal LOS were compared to the simulated spectra and radial intensity profiles that represent theoretical fast-ion distribution functions from TRANSP. A clear disagreement between the simulations and measurements was observed when applying a fast-ion distribution function that was calculated with a predefined anomalous fast-ion transport of $1\mathrm{m}^2/\mathrm{s}$. In contrast, the neo-classical prediction (without the assumption of an additional anomalous transport) describes the absolute intensity and the measured shape of the FIDA radiation very well. Even the different spectral shapes of the FIDA radiation, measured by the toroidal and poloidal LOS, which correspond to different parts of the fast-ion velocity distribution, are well described. This indicates that TRANSP models the fast-ion velocity distribution very well and that the anomalous transport is small for plasmas with low levels of on-axis NBI heating.

In addition, the possible effect of micro-turbulence on the fast-ion transport has been studied in discharges that were performed similarly to previous NBI current drive experiments where differences between the measured and predicted off-axis fast-ion current drive efficiency had been attributed to a possible anomalous fast-ion transport. To test this hypothesis, two discharges with different collisionalities (0.52 and 0.13) were analyzed in which 5 MW of on-axis NBI heating power was replaced by 5 MW of off-axis NBI. A clear difference between measured shapes of the radial FIDA intensity profiles is observed in the experiments during on-axis and off-axis NBI: During on-axis NBI the profiles are peaked close to the plasma center while during off-axis NBI, the FIDA intensity is maximal further

out. This observation is supported by the neo-classical simulations from TRANSP in combination with F90FIDASIM. In both experiments, the measured radial profiles agree very well with the neo-classical simulations. In contrast, the simulations that assume an anomalous transport of $1\mathrm{m}^2/\mathrm{s}$ and $0.5\mathrm{m}^2/\mathrm{s}$ do not agree with the measurement. The possible fast-ion diffusion, induced by micro-turbulence is consequently below the diagnostic sensitivity.

In contrast to the good fast-ion confinement observed in the MHD-quiescent plasmas, a strong fast-ion redistribution has been observed in the presence of magnetic reconnection events caused by sawtooth crashes. Sawtooth crashes are routinely observed in the experiments at ASDEX Upgrade and appear when the q=1 surface exists.

After sawtooth crashes, the toroidal and poloidal LOS of the FIDA diagnostic observe a drop of the central fast-ion distribution of up to 50% while the fast-ion density outside the q=1 surface increases. This increase is different for the toroidal and poloidal LOS which can be explained if passing fast-ions were dominantly redistributed, as reported from other fusion experiments. Furthermore, comparisons to simulations that use the Kadomtsev model to predict the fast-ion redistribution during sawtooth crashes show good agreement with the measurement of passing fast-ions. This implies that the fast-ions follow closely the magnetic field lines during the reconnection imposed by the sawtooth crash and that they are not ejected further out.

It has also been found that the fast-ion transport can be analyzed by studying the recovery phase after sawtooth crashes. By analyzing the decay of the increased fast-ion density outside the q=1 surface in the absence of MHD-activity between the crashes, a neo-classical fast-ion behavior is again indicated by the fact that the observed decay times fit well to the TRANSP predicted slowing down times. However, in the presence of fishbone activity, the fast-ion distribution function is found to deviate from the neo-classical simulation and a moderate anomalous fast-ion diffusion is needed to fit the measurements.

8.4 Outlook

In further investigations using the FIDA diagnostic, not only the effect of sawtooth crashes on the fast-ion distribution function, but also the redistribution caused by magnetic islands, Alfvén Eigenmodes or ELMs could be investigated. Moreover, the FIDA diagnostic could be used to study the further acceleration of beam ions by the second harmonic ICRH frequency. Thereby, in particular the poloidal LOS of the diagnostic could be used to investigate, for example, the power deposition position of ICRH, since the accelerated particles are supposed to have large velocity vectors perpendicular to the magnetic field lines (small pitches).

The MSE diagnostic is currently being refurbished with the aim to perform absolutely calibrated measurements of the q-profile with a high signal to noise ratio. This will enable to investigate the NBI current drive efficiency in detail by comparing the MSE measurement to simulations that are based on fast-ion distribution functions, validated by the FIDA measurement.

In addition, the FIDA diagnostic capabilities could be upgraded for future investigations. By installing two additional optical heads at ASDEX Upgrade whose LOS have angles to the magnetic field lines close to 90° and 30°, a tomographic reconstruction of the fast-ion velocity space could be performed. Thereby, for example the temperature dependence of the critical energy for the onset of pitch angle scattering with ions could be investigated or the effect of sawtooth crashes on the fast-ion velocity space distribution could be further clarified. Furthermore, photo multipliers could be used to measure the FIDA radiation with

a higher temporal resolution than 2ms. This would permit to study perturbations of the fast-ion distribution function that are, for example, induced by single fishbone instabilities or by magnetic islands. The interference filters that would be necessary for such measurements must define a narrow wavelength range of approximately one nanometer with very sharp edges. If they were available, they could also be used at ASDEX Upgrade for a 2D imaging diagnostic that would allow 2D measurements of the FIDA radiation as reported in [79].

Acknowledgment

First of all, I would like to thank my academic supervisor Professor Hartmut Zohm who enabled this Ph.D work and who helped a lot with his great expertise. Furthermore I would like to thank Dr. Manuel Garcia Munoz for his excellent supervision during this thesis. In plenty of discussions he introduced me into the field of fast-ion physics.

I would also like to express my deep gratitude to my group leader Dr. François Ryter who always had time for me to discuss my work and to decide in which direction my research should be directed. For his help building the spectrometer and installing the optics inside the torus of ASDEX Upgrade, I am especially indebted to Dr. Ralf Dux who was also involved in the interpretation of the beam emission spectra and in the development of the collisional radiative of F90FIDASIM. I would also like to thank Dr. Giovanni Tardini for helping me with the TRANSP simulations. Without him, it would not have been possible to take advantage of this code.

Special thanks also go to Professor Bill Heidbrink who originally wrote FIDAsim and who kindly offered his version to the ASDEX Upgrade team. We further developed FIDASIM in a good collaboration and will soon release the new Fortran version to the fusion community.

For renewing the optics of the toroidal LOS, I would like to thank Dr. Rachael McDermott. This significantly increased the signal to noise ratio of the FIDA measurements and made the results obtained during this thesis possible. I would also like to thank Dr. Jörg Hobirk who was involved in the planning and carrying out of the discharges presented in this thesis and to Dr. Mirko Salewski with whom I developed the method of simulating FIDA spectra by using the weight functions.

I am grateful to Dr. Rainer Fischer who helped me learning the Fortran programming language an who provided sophisticated electron temperature and density profiles used in the analysis of the FIDA spectra. I also want to thank Dr. Thomas Pütterich and Dr. Luis Menchero who helped me understanding the atomic physics of the cross-sections. Also many thanks go to Dr. Emiliano Fable and Dr. Valentine Igochine who explained the physical background of the MHD effects, such as the sawteeth, with great patience. I also want to thank Dr. Tilmann Lunt who enabled the 2D beam imaging measurements that were used to check the beam divergence and focus of NBI3.

For providing the theoretical wavelengths of D2-molecular lines, I would like to thank Dr. Dirk Wünderlich. Furthermore, I would like to extend my thanks to Reinhard Treske who spent plenty of time sharpening the spectrometer entrance slit, to Karl Eismann for organizing the construction of the individual parts of the spectrometer, to Michael Ebner who helped to install the poloidal optical head in the torus and to Helmut Blank and Roland Merkel who helped with the computer installation.

I would also like to thank Eleonora Viezzer, Dr. Steffen Potzel and Felix Reimold for a very good collaboration when calibrating the various spectrometers present at ASDEX Upgrade. Moreover, I thank my colleagues Dr. Jurrian Boom, Dr. Ivo Classen, Dr. Philip

Schneider, Sina Fietz, Christian Vorpahl and Mike Dunne for their continuing help with day to day problems.

For the good time we had in the European Ph.D Network in Padua and Lisbon I would like to thank Fabian Sommer, Andreas Burkhart, Matthias Bernert and Silvia Rathgeber.

To conclude these acknowledgments, have to cordially thank the whole ASDEX Upgrade team for their continuous help and assistance and for the very good working atmosphere.

Bibliography

[1] http://en.wikipedia.org/wiki/File:FusionintheSun.svg (2012).

[2] LANGMUIR, I., Proc. Natl. Acad. Sci. U.S.A. **14** (1928) 627.

[3] SPITZER, L. et al., *A Proposed Stellarator*, Princeton University Plasma Physics Laboratory, 1951.

[4] RUTHERFORD, P., Nuclear Fusion **20** (1980) 1086.

[5] EDITORS, I. P. B. et al., Nuclear Fusion **39** (1999) 2137.

[6] http://www.efda.org/2011/09/tokamak-principle-2/?view=gallery-273 (2012).

[7] WESSON, J., *Tokamaks*, Clarendon Press Oxford, 1997.

[8] http://www.iter.org/mach/heating (2012).

[9] FASOLI, A. et al., Nuclear Fusion **47** (2007) S264.

[10] ZOHM, H., Fusion science and technology **58** (2010) 613.

[11] GARCIA-MUNOZ, M. et al., Review of Scientific Instruments **80** (2009) 053503.

[12] HUTCHINSON, I. H., *Principles of Plasma Diagnostic's*, New York: Cambridge University Press, 1987.

[13] KIPTILY, V. et al., Nuclear Fusion **42** (2002) 999.

[14] BINDSLEV, H. et al., Phys. Rev. Lett. **83** (1999) 3206.

[15] HELLESEN, C. et al., Plasma Physics and Controlled Fusion **52** (2010) 085013.

[16] HEIDBRINK, W. W. et al., Plasma Physics and Controlled Fusion **46** (2004) 1855.

[17] DELABIE, E. et al., Review of Scientific Instruments **79** (2008) 10E522.

[18] OSAKABE, M. et al., Review of Scientific Instruments **79** (2008) 10E519.

[19] HEIDBRINK, W. W. et al., Review of Scientific Instruments **77** (2006) 10F120.

[20] GEIGER, B. et al., Plasma Physics and Controlled Fusion **53** (2011) 065010.

[21] MARTY, C. et al., Plasma Physics and Controlled Nuclear Fusion Research **1** (1969) 847.

[22] STIX, T. H., Plasma Physics **14** (1972) 367.

[23] SAUTER, O. et al., Physics of Plasmas **6** (1999) 2834.

[24] FISCH, N. J., Rev. Mod. Phys. **59** (1987) 175.

[25] HONDA, M. et al., Nuclear Fusion **52** (2012) 023021.

[26] RYTER, F. et al., Phys. Rev. Lett. **86** (2001) 2325.

[27] WOOTTON, A. J. et al., Physics of Fluids B: Plasma Physics **2** (1990) 2879.

[28] HAUFF, T. et al., Phys. Rev. Lett. **102** (2009) 075004.

[29] HEIDBRINK, W. W. et al., Phys. Rev. Lett. **103** (2009) 175001.

[30] GüNTER, S. et al., Nuclear Fusion **47** (2007) 920.

[31] HEIDBRINK, W. et al., Nuclear Fusion **31** (1991) 1635.

[32] CLASSEN, I. G. J. et al., Phys. Rev. Lett. **98** (2007) 035001.

[33] ZOHM, H., Plasma Physics and Controlled Fusion **38** (1996) 105.

[34] GARCIA-MUNOZ, E. A., Phys. Rev. Lett. **104** (2010) 185002.

[35] GARCIA-MUNOZ, M. et al., Nuclear Fusion **51** (2011) 103013.

[36] PORCELLI, F., Plasma Physics and Controlled Fusion **33** (1991) 1601.

[37] CHEN, L. et al., Phys. Rev. Lett. **52** (1984) 1122.

[38] KADOMTSEV, B. B., Reports on Progress in Physics **50** (1987) 115.

[39] PARKER, Journal of Geophysical Research **62** (1957) 509.

[40] PORCELLI, F. et al., Plasma Physics and Controlled Fusion **38** (1996) 2163.

[41] KOLESNICHENKO, Y. et al., Nuclear Fusion **36** (1996) 159.

[42] NIELSEN, S. K. et al., Plasma Physics and Controlled Fusion **52** (2010) 092001.

[43] VON HELLERMANN, M. G. et al., Plasma Physics and Controlled Fusion **35** (1993) 799.

[44] LUO, Y. et al., Review of Scientific Instruments **78** (2007) 033505.

[45] ISLER, R. C., Plasma Physics and Controlled Fusion **36** (1994) 171.

[46] ROSENBLUTH, M. N. et al., Phys. Rev. **107** (1957) 1.

[47] PANKIN, A. et al., Computer Physics Communications **159** (2004) 157 .

[48] WAGNER, F. et al., Phys. Rev. Lett. **49** (1982) 1408.

[49] SCHNEIDER, W. et al., Fusion Engineering and Design **48** (2000) 127 .

[50] SHAFRANOV, V., Sov. Phys. JETP **6** (1958) 545.

[51] FISCHER, R. et al., Plasma Physics and Controlled Fusion **50** (2008) 085009.

[52] RATHGEBER, S. K. et al., Plasma Physics and Controlled Fusion **52** (2010) 095008.

[53] HEIDBRINK, W. et al., Commun. Comput. Phys. **10** (2011) 716.

[54] CARTHY, P. J. M., Physics of Plasmas **6** (1999) 3554.

[55] R. FISCHER, E. A., Fusion Science and Technology **58** (2010) 675.

[56] SCHRöDINGER, E., Annalen der Physik **385** (1926) 437.

[57] http://en.wikipedia.org (2012).

[58] SALEWSKI, M. et al., Nuclear Fusion **52** (2012) 103008.

[59] ZEELAND, M. A. V., Plasma Physics and Controlled Fusion **52** (2010) 045006.

[60] WIESE, W. L. et al., *Atomic Transition Probabilities*, NSRDS- NBS 22. U.S.A. National Bureau of Standards, Washington DC, 1969.

[61] HUTCHINSON, I. H., Plasma Physics and Controlled Fusion **44** (2002) 71.

[62] JANEV, R. K. et al., Nucl. Fusion Suppl. Special Issue **4** (1993) 172.

[63] JANEV, R. K. et al., B2EIRENE report (2004).

[64] MULLANE, M. O., (2009).

[65] REINHOLD, C. O. et al., Phys. Rev. A **41** (1990) 4837.

[66] http://www.efunda.com/math/ode/syslinearode1.cfm (2012).

[67] http://www.adas.ac.uk (2012).

[68] DUX, R., EPS Strasbourg (2011).

[69] http://physics.nist.gov/cgi-bin/ASD/lines1.pl (2012).

[70] GARCIA, J. D. et al., J. Opt. Soc. Am. **55** (1965) 654.

[71] STEHLÉ, C. et al., Astron. Astrophys. SuppL. Ser. **140** (1999) 93.

[72] POTZEL, S., EPS Strasbourg (2011).

[73] FREUND, R. et al., J. Phys. Chem. Ref. **14** (1985) 235.

[74] KIROV, K. K. et al., Plasma Physics and Controlled Fusion **44** (2002) 2583.

[75] IGOCHINE, V. et al., Nuclear Fusion **47** (2007) 23.

[76] MARCUS, F. B. et al., Plasma Physics and Controlled Fusion **33** (1991) 277.

[77] MUSCATELLO, C. M. et al., Plasma Physics and Controlled Fusion **54** (2012) 025006.

[78] CARDOZO, N. J. L., Plasma Physics and Controlled Fusion **37** (1995) 799.

[79] ZEELAND, M. A. V. et al., Plasma Physics and Controlled Fusion **51** (2009) 055001.

Appendix A

Analytic solution of equation 4.27 used by F90FIDASIM

F90FIDASIM calculates the population of the individual excited states of Deuterium neutrals (see chapter 4.1.8) by solving a system of first order linear ordinary differential equations:

$$\dot{\vec{N}} = \mathbf{A} \cdot \vec{N} \tag{A.1}$$

Here, $\vec{N}$ is a vector of fluxes (density per second) of neutrals in the different atomic states (n=1 to n=6) and $\dot{\vec{N}}$ is its time derivative. $\mathbf{A}$ is a matrix consisting of the rates that describe the excitation, de-excitation and ionization of the neutrals.

An analytic approach to calculate the flux of neutrals after a time interval, dt, from this differential equation has been applied in F90FIDASIM according to [66]. It is based on the determination of the eigenvectors, $\vec{s_i}$, and the eigenvalues, λ_i, of the matrix $\mathbf{A}$ which fulfill:

$$\mathbf{A} \cdot \vec{s_i} = \vec{s_i} \cdot \lambda_i \tag{A.2}$$

By applying the following substitution in equation A.1:

$$\vec{N} = \mathbf{S} \cdot \vec{Y} \tag{A.3}$$

one obtains

$$\dot{\vec{Y}} = \mathbf{S}^{-1} \cdot A \cdot \mathbf{S} \cdot \vec{Y} \tag{A.4}$$

where $\mathbf{S}$ is the matrix of eigenvectors $\vec{s_i}$ and $\mathbf{S}^{-1}$ is its inverse. By applying equation A.2, equation A.4 becomes:

$$\dot{\vec{Y}} = \mathbf{\Lambda} \cdot \vec{Y} \tag{A.5}$$

where $\mathbf{\Lambda}$ is a diagonal matrix containing the eigenvalues λ_i. This differential equation can be solved by the Ansatz:

$$\vec{Y} = \vec{C} \cdot \ \exp(\mathbf{\Lambda}\ dt) \tag{A.6}$$

where dt is the time interval for which the flux of neutrals, $\vec{N}(dt)$, should be calculated and $\vec{C}$ is a vector of integration constants. The back-substitution of equation A.6 yields:

$$\vec{N} \cdot \mathbf{S} = \vec{C} \cdot \ \exp(\mathbf{\Lambda}\ dt) \tag{A.7}$$

By using the definition that at $dt = 0$, the flux of neutrals, $\vec{N}(dt)$, is equal to the initial flux, $\vec{N}(0)$, the vector of integration constants, $\vec{C}$, can be replaced by $\vec{N}(0) \cdot \mathbf{S}$ which finally yields the analytic solution shown in chapter 4.1.8:

$$\vec{N}(dt) = \mathbf{S}^{-1} \cdot \vec{N}(0) \cdot \mathbf{S}\ \exp(\mathbf{\Lambda}\ dt) \tag{A.8}$$

Appendix B

Cross-sections used in F90FIDASIM

In this section, all cross-sections used in F90FIDASIM are presented. The cross-sections are given as a function of collision energy per atomic mass unit, i.e. are given for hydrogen atoms. When applying these cross-sections to reactions with deuterium atoms, different relative collision energies must be taken into account.

First, cross-sections are described that correspond to collisions between hydrogen atoms and electrons. Then the cross-sections for collisions between hydrogen atoms and ions are illustrated. Finally the cross-sections for collisions between fully stripped boron ions and hydrogen atoms are given.

B.1 Collisions between hydrogen atoms and electrons

The cross-sections for collisions between hydrogen atoms and electrons have been taken from a report by R.K. Janev [63].

B.1.1 Electron impact ionization

The cross-sections for impact ionization of hydrogen atoms by electrons are displayed in figure B.1 for initial states between n=1 and n=12. Clearly the cross-sections for impact ionization decrease with increasing collision energies.

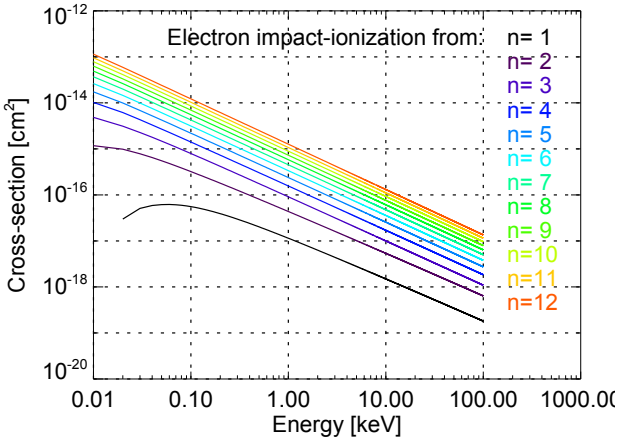

Figure B.1: Cross-sections for electron impact ionization of hydrogen atoms ($e^- + H(n) \rightarrow e^- + H^+ + e^-$)

B.1.2 Electron impact excitation

The cross-sections for electron impact excitation are depicted in figure B.2 as a function of the relative collision energy of the electrons in $[keV]$. As can be seen, the probability for electron impact excitation decreases with the collision energy.

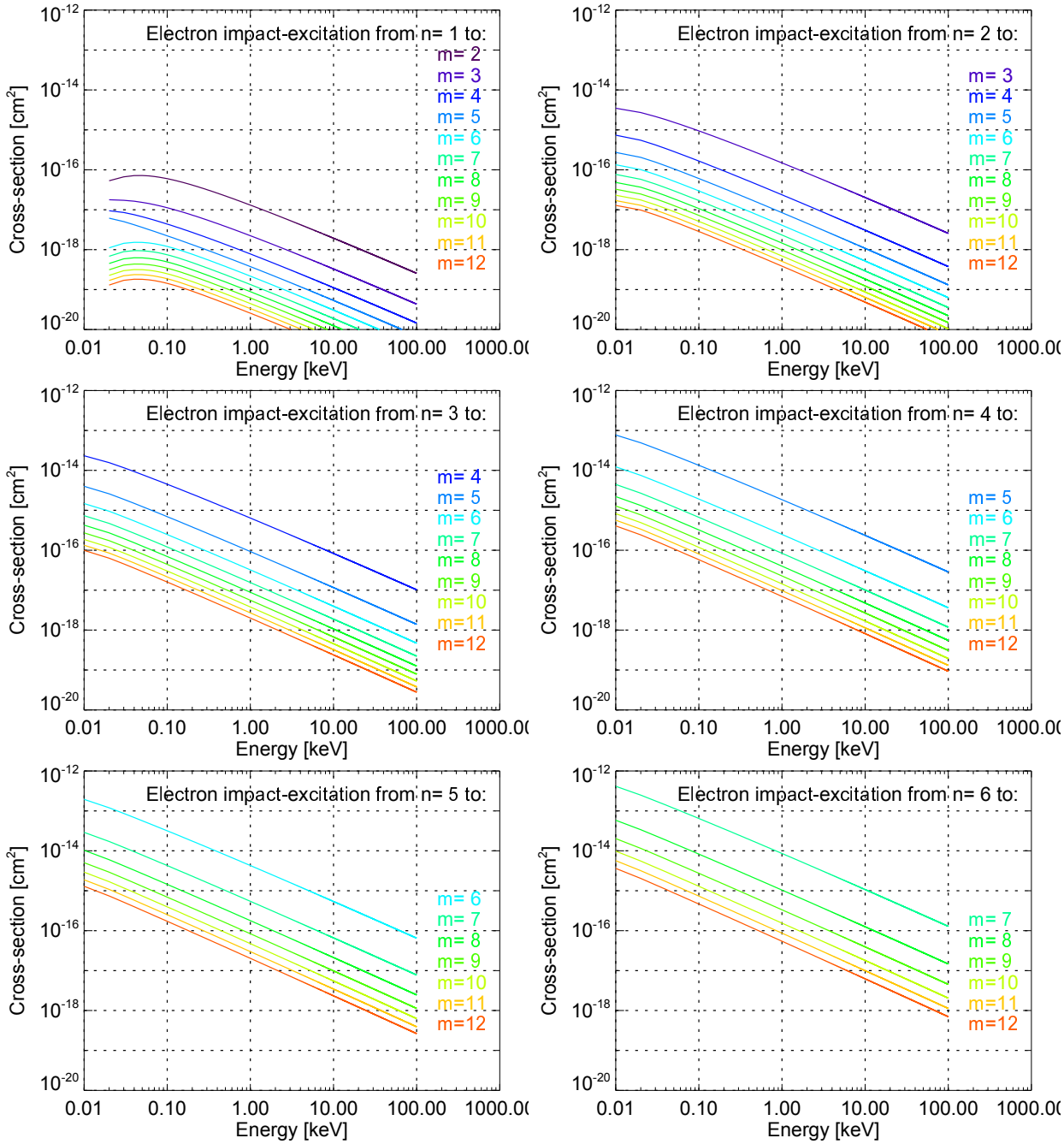

Figure B.2: Cross-sections for electron impact excitation of hydrogen atoms for initial states between n=1 and n=6 and for final states up to m=12. $(e^- + H(n) \rightarrow e^- + H(m))$

B.2 Collisions between hydrogen atoms and ions

The collisions between hydrogen atoms and hydrogen ions can result in an excitation, ionization or a charge exchange process.

B.2.1 Charge exchange

The charge exchange cross-sections between hydrogen ions and atoms have been taken from Janev and Smith [62] and ADAS [67]. The dotted lines in figure B.3 indicate the total, bundled cross-sections from Janev and Smith which are used in the collisional radiative model of F90FIDASIM. The m-resolved cross-sections, displayed in color, are applied when

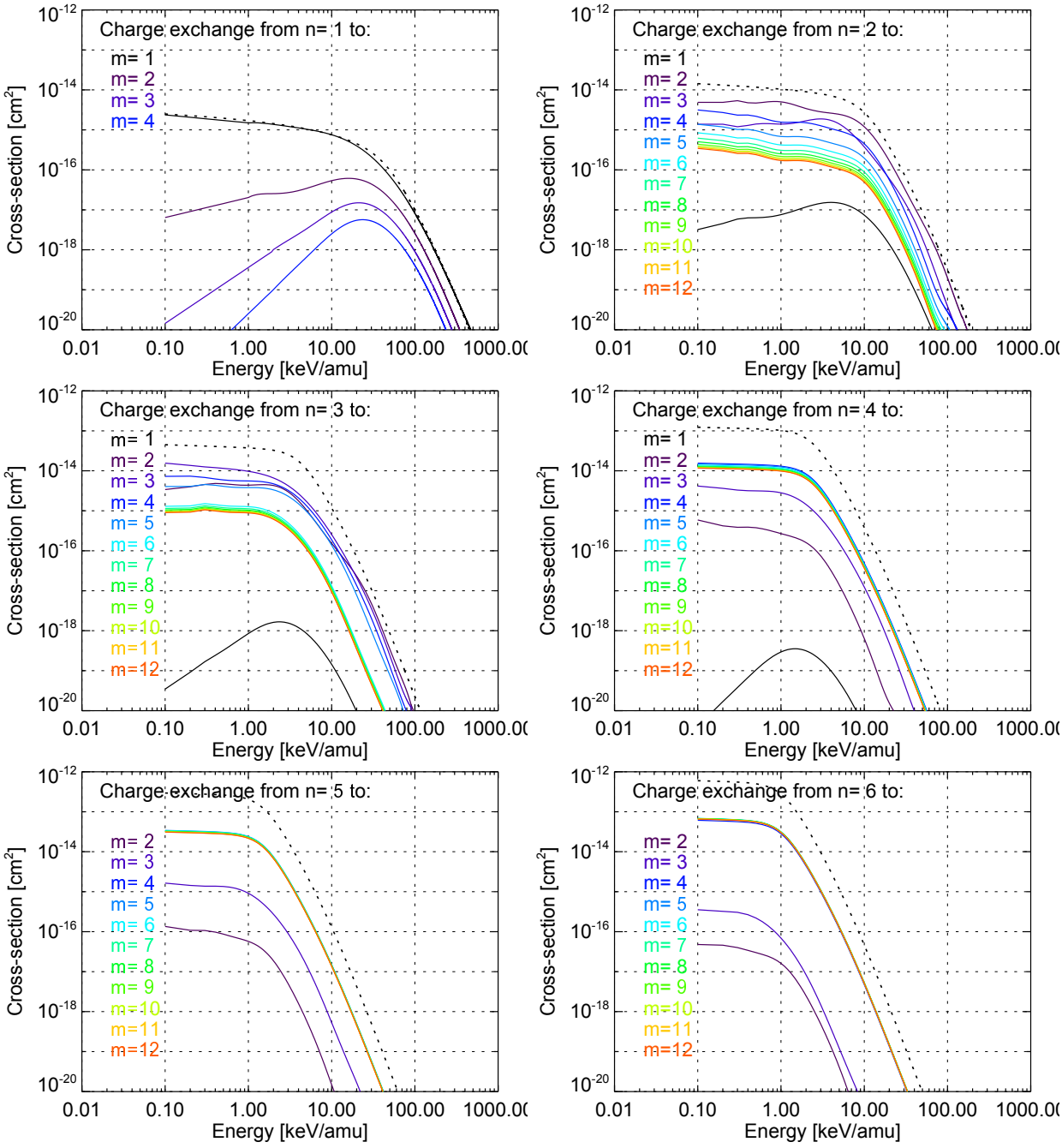

Figure B.3: Charge-exchange cross-sections between hydrogen atoms and hydrogen ions. The dotted lines are the total cross-sections into all m-states. The m-resolved cross-sections are shown in color ($H^+ + H(n) \rightarrow H(m) + H^+$).

determining the neutralization rates of fast- and thermal ions (see section 4.1.9). The m-resolved cross-sections for n=1,n=2 and n=3 are provided by the ADAS database whereby it was found that the cross-sections for n=2 and for n=3 needed to be corrected because the ADAS routines that calculate the cross-sections from fitting formulas, erroneously do not scale the relative collision energy by n^2. The m-resolved cross-sections between m=4

and m=6 have been approximated by the reversibility formula (see equation 4.34) and by un-bundling the Janev cross-sections. To un-bundle the Janev cross-section, the assumption has been made that the probability for a charge exchange reaction from a initial state, n, to a final state, m, depends exponentially on the energy difference between the states.

B.2.2 Proton impact ionization

Figure B.4 illustrates the cross-sections for impact ionization by collisions between hydrogen ions (protons) and hydrogen atoms with excited states up to n=12. The cross-sections for impact ionization of hydrogen atoms with excited states up to n=5 are taken from a report by M. O'Mullane [64]. The cross-sections for initial states above n=5 are derived using a scaling law provided by Janev and Smith [62].

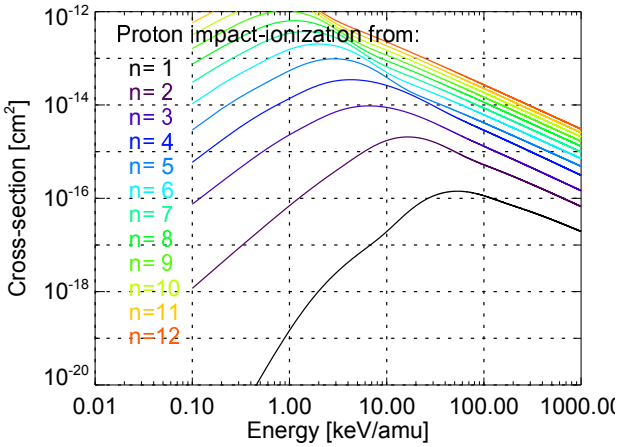

Figure B.4: Cross-sections for proton impact ionization of hydrogen atoms with atomic states between n=1 and n=12 ($H^+ + H(n) \rightarrow H^+ + H^+ + e^-$).

B.2.3 Proton impact excitation

The cross-sections for the impact excitation of hydrogen atoms by the collision with hydrogen ions (protons) are depicted in figure B.5. As can be seen, the cross-sections, which have been taken from [63], increase as a function of the initial state n and decrease with the final state m.

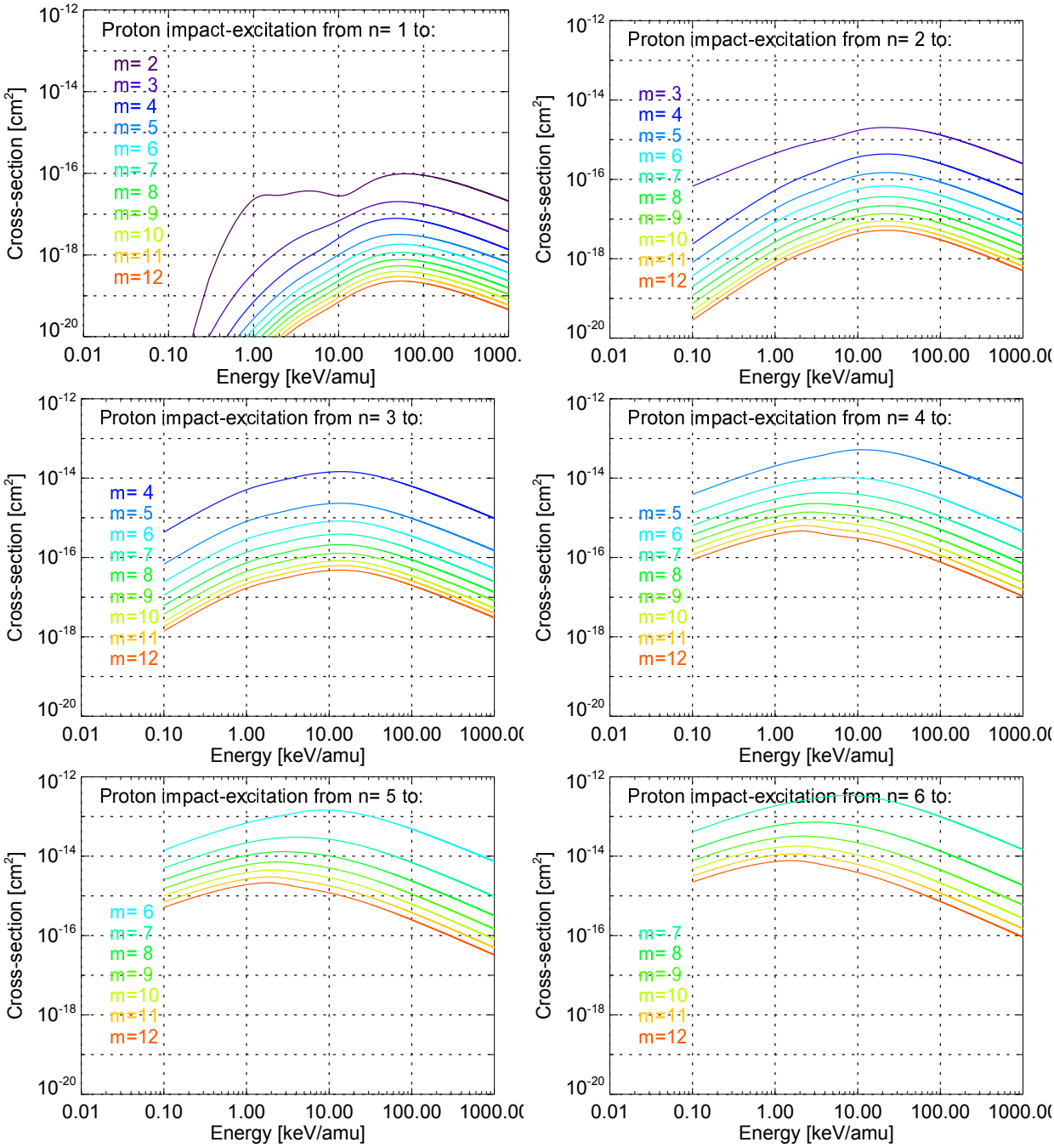

Figure B.5: Cross-sections for impact excitation of hydrogen atoms by collisions with protons for initial states between n=1 and n=6 and for final states up to m=12 ($H^+ + H(n) \rightarrow H^+ + H(m)$).

B.3 Collisions between hydrogen atoms and boron ions

Here, the cross-sections for reactions between hydrogen atoms and boron ions are plotted. This element is, in particular after boronizations, the dominant impurity species in ASDEX Upgrade plasmas and this therefore used in F90FIDASIM as the main impurity species.

B.3.1 Boron impact ionization and charge exchange

The cross-sections for boron impact excitation and for charge exchange reactions are shown in figure B.6. The cross-sections for excited states above n=2 are taken from Janev and Smith [62] and the cross-sections for the atomic states n=1 and n=2 are taken from ADAS the database [67].

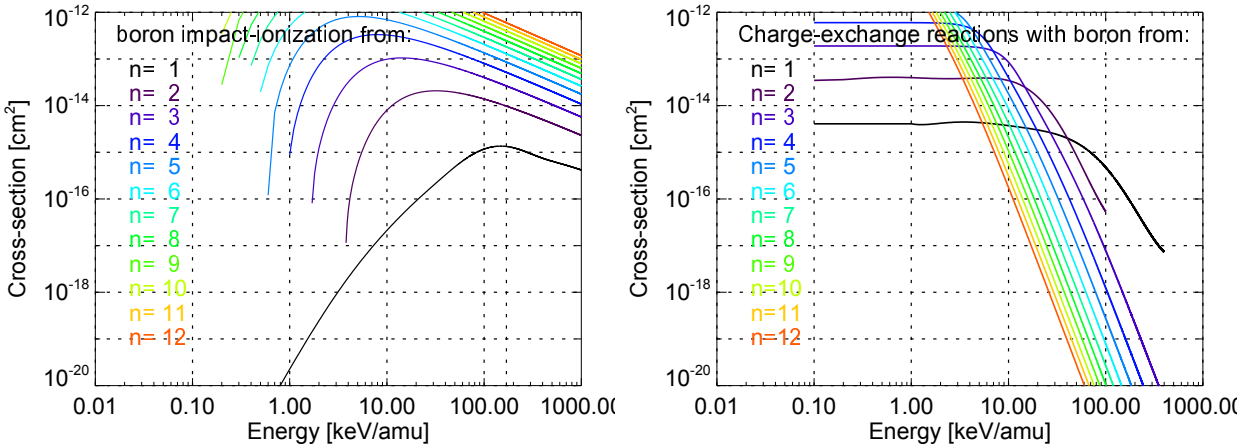

Figure B.6: Left: Cross-sections for impact ionization of hydrogen atoms by fully stripped boron ions ($B^{5+} + H(n) \rightarrow B^{5+} + H^{+} + e^{-}$). Right: Cross-sections for charge-exchange between fully stripped boron ions and hydrogen atoms with excited states between n=1 and n=12 ($B^{5+} + H(n) \rightarrow B^{4+} + H^{+}$).

B.3.2 Boron impact excitation

The cross-sections for impact excitation of hydrogen atoms by collisions with fully stripped boron ions are shown in figure B.7. They have been taken from the report by Janev and Smith [62].

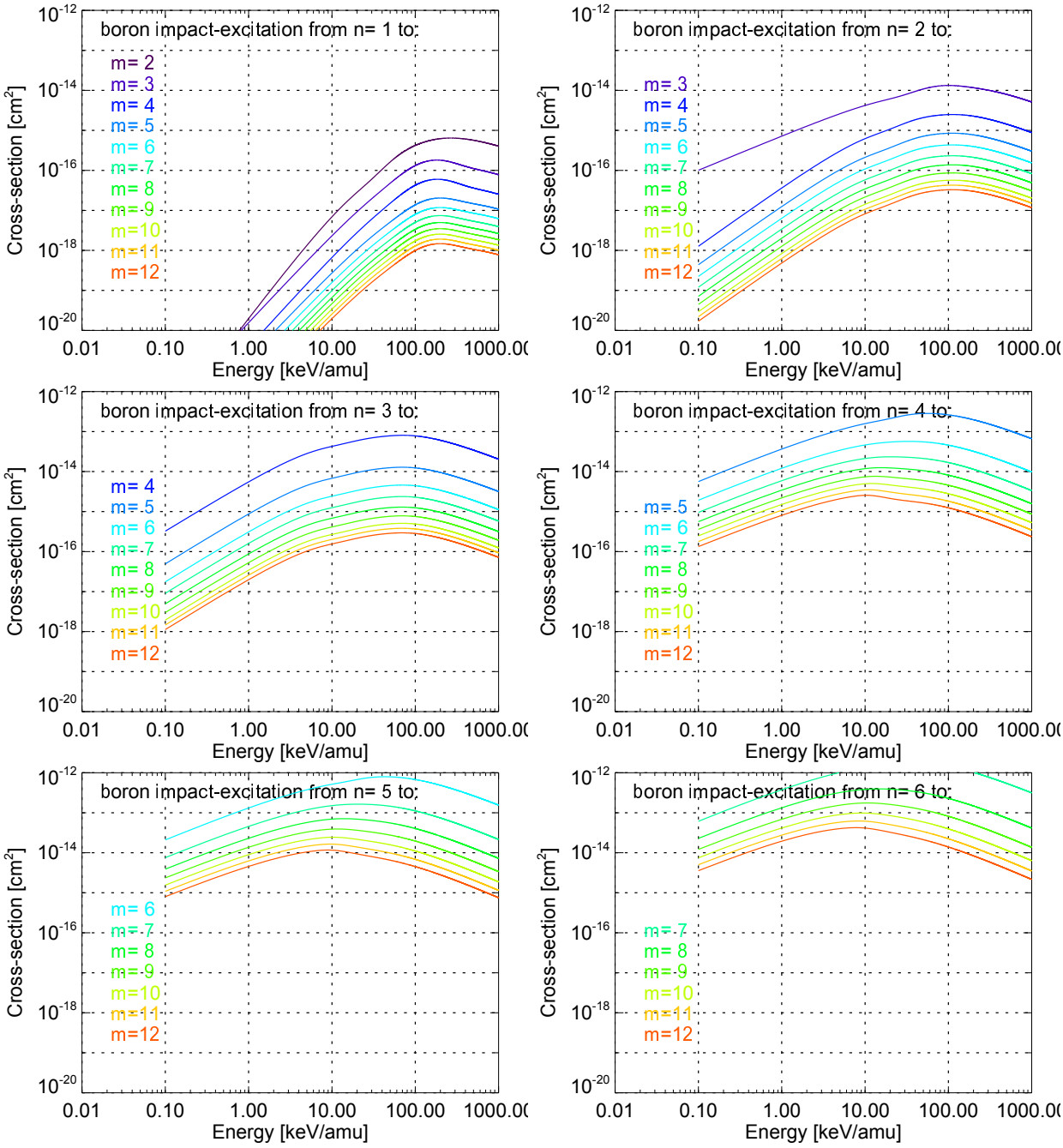

Figure B.7: Cross-sections for boron impact excitation of hydrogen atoms for initial states from n=1 to n=6 and for final states up to m=12 ($B^{5+} + H(n) \rightarrow B^{5+} + H(m)$).